



A scanning LiDAR for long range detection and tracking of UAVs

Alain Quentel

► To cite this version:

Alain Quentel. A scanning LiDAR for long range detection and tracking of UAVs. Electronics. Normandie Université, 2021. English. NNT : 2021NORMR011 . tel-03228683

HAL Id: tel-03228683

<https://theses.hal.science/tel-03228683>

Submitted on 18 May 2021

HAL is a multi-disciplinary open access archive for the deposit and dissemination of scientific research documents, whether they are published or not. The documents may come from teaching and research institutions in France or abroad, or from public or private research centers.

L'archive ouverte pluridisciplinaire **HAL**, est destinée au dépôt et à la diffusion de documents scientifiques de niveau recherche, publiés ou non, émanant des établissements d'enseignement et de recherche français ou étrangers, des laboratoires publics ou privés.



Normandie Université

THÈSE

Pour obtenir le diplôme de doctorat

**Spécialité ELECTRONIQUE, MICROELECTRONIQUE, OPTIQUE ET LASERS,
OPTOELECTRONIQUE MICROONDES**

Préparée au sein de l'Université de Rouen Normandie & d'ArianeGroup

A scanning LiDAR for long range detection and tracking of UAVs

**Présentée et soutenue par
Alain QUENTEL**

**Thèse soutenue publiquement le 13 janvier 2021
devant le jury composé de**

M. François GOUDAIL	Professeur des Universités, Institut d'Optique Graduate School (IOGS)	Rapporteur
M. Santiago ROYO	Associate professor, Universitat Politècnica de Catalunya (UPC)	Rapporteur
Mme. Angélique RISSONS	Professeure des Universités, Institut Supérieur de l'Aréonautique et de l'Espace (ISAE-SUPAERO)	Examinatrice
M. Didier BLAVETTE	Professeur des Universités, Université de Rouen Normandie	Examineur
M. Frank CHRISTNACHER	Docteur en physique, Institut Saint Louis (ISL)	Examineur
M. Yohan DUPUIS	HDR, ingénieur de recherche au sein de l'Institut de Recherche en Systèmes Electroniques Embarqués (IRSEEM)	Directeur de thèse

Thèse dirigée par Yohan Dupuis, Institut de Recherche en Systèmes Electroniques Embarqués (IRSEEM)



A scanning LiDAR for long range detection and tracking of UAVs

Abstract: Misuse of civil drones, or UAVs (unmanned aerial vehicles) has been a rising concern in the past few years. As a response, multiple systems including optics, electronics and even acoustics technologies have been developed for detection and tracking. Unfortunately, UAVs represent a challenging target to detect and track due to their small, decimetric size and large variability of shapes and behaviors. In this PhD, we developed and optimized a LiDAR (light detection and ranging) system to tackle this issue to distances up to a kilometer.

In our system, range is acquired using the time of flight principle, and imagery done by sequentially scanning the scene with a dual-axis galvanometer. We took advantage of the scanning versatility to develop several operating modes. A standard detection mode captures the image of the scene using a raster-scan of large field of view. Tracking mode is based on a local pattern surrounding the target, which is updated at a very high rate to keep the target within its boundaries.

Efforts were put into a theoretical and numerical optimization study of the numerous parameters involved in our scanning LiDAR, so as to reach sufficient performances in term of maximal range, localization resolution and rate. Pattern optimization for both detection and tracking mode was a primary focus, using the target probability of detection as the function to maximize. Target size, speed and reflectivity was also introduced in the probability of detection, giving a complete overview of the system performance. On our LiDAR platform, developed from the ground up, each component was characterized to enrich and validate our models. This prototype was tested for UAVs detection and tracking during several weeks of trials. Following this success, a pre-industrial integration process was launched and supervised by the candidate.

Keywords: LiDAR scanner, LiDAR tracker, ToF system, UAV tracking

Développement d'un LiDAR à balayage pour la détection et la poursuite longue portée de drones

Résumé: L'utilisation abusive de drones civils est une préoccupation croissante depuis ces dernières années. En réponse, de multiples systèmes basés sur des technologies optiques, électroniques et même acoustiques ont été développés pour la détection et la poursuite de ces drones. Cela représente néanmoins un challenge en raison de leur faible taille et de leur grande diversité de formes et de trajectoire. Afin de répondre à ce besoin pour des distances allant jusqu'au kilomètre, nous avons recherché, développé et optimisé un système LiDAR (light detection and ranging) à balayage.

Dans notre système, la mesure de distance est réalisée via le principe du temps de vol, et l'imagerie est effectuée en scannant séquentiellement la scène en utilisant un système de miroir galvanométrique à deux axes. Nous avons profité de la polyvalence du système de balayage pour développer plusieurs modes de fonctionnement. Un mode de détection classique réalise l'image de la scène à l'aide d'un balayage ligne par ligne de type grand champ. Le mode de suivi est basé sur un motif local entourant la cible, qui est mis à jour à une très haute cadence afin de maintenir la cible dans les limites de ce motif.

Nous avons réalisé une étude d'optimisation, théorique et numérique, des nombreux paramètres impliqués dans le balayage LiDAR afin d'atteindre des performances satisfaisantes en termes de portée maximale, de résolution et de fréquence de localisation. L'optimisation des modèles pour les modes de détection et de poursuite a été le principal focus, en utilisant la probabilité de détection cible comme fonction à maximiser. La taille, la vitesse et la réflectivité de la cible ont également été incluses dans la probabilité de détection, donnant un aperçu complet des performances du système. Sur la plateforme LiDAR, chaque composant a été caractérisé afin d'enrichir et de valider nos modèles. Cette plateforme a été testée durant plusieurs semaines d'essais, au cours desquelles nous avons réalisé la détection et la poursuite de divers types de drones. S'en est suivi un processus d'intégration pré-industrielle des chaînes optiques, électroniques et algorithmiques.

Mots clés : LiDAR à balayage, LiDAR de poursuite, temps de vol, poursuite de drone

Acknowledgements

Completing a PhD thesis is not an individual experience. Rather, it is the fruit of team work and the support of various persons that I wish to thank sincerely.

Firstly, I would like to express my deep gratitude to Olivier Maurice, my advisor at ArianeGroup, for his indefective support, his immense wisdom and his sense of humor! This PhD would not have been made without him. I would also like to thank Xavier Savatier, my first PhD advisor, and then Yohan Dupuis who took over. Both were always available to discuss one matter or the other. My sincere thanks also goes to François Nguyen, my manager at ArianeGroup, for his advices and his dynamic management. A very special thanks to Guy-Maël Jacobe de Naurois, who first started the internship and then secured the PhD funding. Our discussions have left a lasting print on me!

Besides my advisors, I would like to thank my colleagues at ArianeGroup. Baptiste Dailly, Angélique Woelffle and François Assemaat for the rich discussions on optics topics. Christophe Castanie, Manuel Ramos, Florent Todeschini and Philippe Meton for their advice on electronics and electromagnetism. And of course the rest of the team for the more lightheaded discussions around a coffee, a meal, or even at the turn of a corridor.

I also wish to thank the people involved in the LiDAR industrial project. First and foremost, Bruno Esmiller for his accessibility and the liberty he gave me on building the system. Gilles Fournier for his deep knowledge in optics and his always pertinent comments and advice. Aurélien Giraud for helping me on the last year and a half on the project, always full of energy and ready to tackle a new task. Damien Lefevre and Julien Brousse for their reactivity and knowledge in mechanical design. Côme Bernard and Stephane Laurent for their patience and dedication in understanding what I wanted to do with the wiring and electronics. Finally, a special thanks to Nicolas Brocard for his dedication to program the LiDAR.

Last but not the least, I would like to thank my family and friends for supporting me throughout these years, providing me a breath of fresh air when needed the most.

Acronyms

ADC analog to digital converter	6
AMCW amplitude modulated continuous wave	6
APD avalanche photodiode	11
BRDF bi-directional reflectivity distribution function	38
BS beamsplitter	25
CAD computed aided design	96
CAV constant angular velocity	76
CCD charge-coupled device	9
CLV constant linear velocity	72
CMOS complementary metal-oxide-semiconductor	9
DFB distributed feedback laser	80
DOA delay of arrival	
FAR false alarm rate	41
FIFO first in, first out	95
FMCW frequency modulated continuous wave	4
FoV field of view	1
FPGA field programmable gated array	
FWHM full width at half maximum	91
HWHM half width at half maximum	
InGaAs indium gallium arsenide	11
InP indium phosphide	18
LiDAR light detection and ranging	1
LWIR long-wavelength infrared, 8000 - 15000 nm	
MEMS microelectromechanical system	12
MPE maximal permitted exposure	28
MWIR mid-wavelength infrared, 3000 - 8000 nm	18

NEP noise equivalent power	43
NIR near infrared, 750 - 1400 nm	12
NHZ nominal hazard zone	101
OPA optical phase array	
PM parabolic mirror	26
PPE personal protective equipment	102
PRF pulse repetition frequency	25
RCS radar cross section	
RF radio frequency	1
ROIC readout integrated circuit	11
RMS root mean square	
Si silicon	12
SNR signal to noise ratio	6
SPAD single photo avalanche diode	11
SWIR short-wavelength infrared, 1400 - 3000 nm	11
TDC time-to-digital converter	36
TDOA time delay of arrival	
TIA transimpedance amplifier	41
ToF time of flight	9
UAV unmanned aerial vehicle	1
UV ultraviolet, 10 nm - 400 nm	
VIS visible wavelength, 400 - 750 nm	

Symbols

a_c	target acceleration	m s^{-1}
a_{fc}	constant for the frequency limit of the scanner	
A_c	target angular diameter	rad
A_m	angular amplitude of the pattern m harmonics	rad
A_p	pattern angular diameter	rad
A_s	amplitude of the cone in intrusion mode	rad
A_θ	azimuth amplitude of the raster-scan	rad
A_φ	elevation amplitude of the raster-scan	rad
b_{fc}	constant for the frequency limit of the scanner	
B_{fm}	amplitude of frequency modulation	Hz
B	bandwidth of the detection chain	Hz
\mathcal{B}	beam surface profile	
c	speed of light in vaccum	m s^{-1}
D_{APD}	APD die diameter	m
D_c	object estimated diameter	m
D_h	parabolic mirror hole diameter	m
D_i	intruder estimated diameter	m
\mathcal{D}_n	APD output distribution without laser signal	
D_r	receiving aperture diameter	m
\mathcal{D}_s	APD output distribution with laser signal	
D_θ	elliptic target dimension in the azimuth direction	m
D_φ	elliptic target dimension in the elevation direction	m
E	light complex amplitude	
f_{BRDF}	local BRDF function	sr
f_c	cutoff frequency	Hz
f_{clock}	timestamping clock frequency	Hz
f_{count}	sampling frequency of the counter wired to the APD output	Hz
f_c^{rt}	scanning frequency limitation due to the laser round trip	Hz
f_c^{liss}	scanning frequency limitation of a Lissajou pattern	Hz
f_c^{tri}	scanning frequency limitation of a triangle pattern	Hz
f_c^{spi}	scanning frequency limitation of a spiral pattern	Hz
f_d	Doppler frequency shift	Hz
f_i	frequency of rotation of the cone in intrusion mode	Hz
f_{IF}	intermediary frequency of a coherent detection	Hz
f_l	pulse repetition rate	Hz
f_{loc}	localization frequency in tracking mode	Hz
f_{loc}^{sim}	simulated localization frequency in tracking mode	Hz
f_o	focal length	m
f_p	pattern frequency	Hz
f_+	intermediary frequency increased by Doppler shift	Hz
f_-	intermediary frequency reduced by Doppler shift	Hz

f_θ	frequency of the triangular function of the raster-scan	Hz
F	APD excess noise factor	
F_{BRDF}	macroscopic BRDF function	sr
FoV_i	photodetector instantaneous field of view	rad
G	avalanche photodetector gain	
\mathcal{G}	surface overlap coefficient between the beam and the object	
G_i	radio-frequency antenna directional gain	
I	intensity of the light wave	W m^{-2}
I_{pd}	APD bulk primary dark current	A
k	threshold relative to the standard deviation	
k_{mV}	threshold applied to the voltage output of the APD	V
l	curvilinear abscissa	rad
L_F	light background radiance	$\text{W m}^{-1} \text{sr}^{-2} \text{m}^{-1}$
m	harmonic number of the pattern considered	
M	module of the wave	V m^{-1}
M^2	beam quality factor	
M_{ba}	module of the backscattered wave	V m^{-1}
M_{lo}	module of the local oscillator wave	V m^{-1}
M_m	module of the incoherent modulation	
n	pattern shape parameter	
n_f	f-number of an optical system	
n_*	effective coating stack refractive index	
N	number of pulses considered in the pattern	
N_p	number of echoes per period in tracking mode	
N_p^{sim}	simulated number of echoes per period in tracking mode	
P_{bg}	average power produced by the background light seen by the APD	W
\mathcal{P}_d	Probability of detection	
P_e	average emitted peak power	W
P_{mean}	emitted mean power	W
P_n	photon equivalent output of the APD without laser signal	W
P_r	average peak power received by the photodetector	W
P_s	photon equivalent output of the APD with laser signal	W
P_{ts}	average peak power at the target plane	W
q	electron charge	A s
r	planar distance beam-target in local coordinate system	m
r_s	spiral angular radius across time	rad
R	distance, or range	m
\mathcal{R}_{D_r}	surface reflectivity in function into an aperture of size D_r	
\mathcal{R}_0	APD unitary gain responsivity	A W
\mathcal{R}_π	hemispherical reflectivity	
s	coefficient of separation intruder-target in securisation mode	
t	time	s
T	period of the frequency modulation	s
\mathcal{T}	object surface profile	
T_a	one way atmospheric transmission coefficient	

T_p	pattern period	s
T_{scan}	period of raster-scan, scanning time	s
u	local coordinate abscissa	m
u_b	beam center abscissa in the local coordinate system	m
u_c	target center abscissa in the local coordinate system	m
U	amplitude of intensity modulation after mixing	
U_{filt}	low-pass filtered amplitude of intensity modulation after mixing	
v	local coordinate ordinate	m
v_b	beam center ordinate in the local coordinate system	m
v_c	target center ordinate in the local coordinate system	m
V	amplitude of intensity modulation after quadratic mixing	
V_c	target speed	m s^{-1}
V_c^θ	target speed in the azimuthal direction	m s^{-1}
V_c^φ	target speed in the elevation direction	m s^{-1}
V_{filt}	filtered amplitude of intensity modulation after mixing	
V_i	intruder speed	m s^{-1}
V_θ	scanner angular target speed	rad s^{-1}
W	beam diameter waist	m
W_0	beam diameter waist at emission	m
x	coordinate axis in the propagation direction	m
y	coordinate axis, axis of rotation for the elevation	m
z	coordinate axis, axis of rotation for the azimuth	m
Z	raster-scan mesh element	
Z_{vc}	raster-scan mesh element taking object speed into account	
α	spiral amplitude tuning parameter	
β	spiral frequency tuning parameter	
γ	raster-scan tuning parameter	
Γ	local coordinate system complementary direction to l and t	rad
δ_i^r	securisation cone mesh element in the radial direction	rad
δ_i^o	securisation cone resolution in the orthogonal direction	rad
δl	hole quantity in the l direction	rad
δ_R	range resolution	m
δt	hole quantity in the t direction	s
$\delta \Gamma$	hole quantity in the <i>Gamma</i> direction	rad
δ_θ	raster-scan resolution in the azimuth direction	rad
δ_φ	raster-scan resolution in the elevation direction	rad
Δ	Average pattern hole	rad
Δ_λ	optical band-pass filter width	m
$\Delta\theta^i$	beam-object depointing in the azimuth direction	rad
$\Delta\varphi^i$	beam-object depointing in the elevation direction	rad
ε	minimal planar distance beam-target to produce an echo	rad
$\zeta_{l,N}$	combination of the probability of echoes from l pulses among N	
η^{BP}	bandpass filter transmission coefficient in emission	
η_e	transmission coefficient in emission	
η_e^{BS}	beamsplitter transmission coefficient in emission	

η_e^{PM}	holed parabolic mirror transmission coefficient in emission	
η_g	transmission coefficient of a silver coated mirror	
η_r	transmission coefficient in reception	
η_r^{BS}	beamsplitter transmission coefficient in reception	
η_r^{PM}	holed parabolic mirror transmission coefficient in reception	
θ	azimuth coordinate	rad
θ_b	azimuth coordinate of the beam	rad
θ_c	azimuth coordinate of the object	rad
$\tilde{\theta}_c$	estimator of the object azimuth coordinate	rad
θ_p	azimuth coordinate of the center of the pattern	rad
Θ_b	full angle beam divergence	rad
κ	atmospheric extinction coefficient	m ⁻¹
λ	wavelength	m
λ_i	filter center wavelength, depending on the incident angle i	m
λ_0	filter center wavelength at normal incidence	m
μ_Δ	average of the Δ criteria	rad
ν	angle in the local polar coordinate system	rad
ρ_0	constant lambertian BRDF	sr
σ_{bg}	photon equivalent standard deviation off the background light	W
σ_n	photon equivalent standard deviation without laser signal	W
σ_{pd}	photon equivalent standard deviation produced of the dark noise	W
σ_s	photon equivalent standard deviation with laser signal	W
σ_{th}	photon equivalent standard deviation of the TIA output	W
σ_R	standard deviation of range distribution	m
σ_Δ	standard deviation of the Δ criteria	rad
τ_p	pulse width	s
ϕ	phase of the wave	rad
φ	elevation coordinate	rad
φ_b	elevation coordinate of the beam	rad
φ_c	elevation coordinate of the object	rad
$\tilde{\varphi}_c$	estimator of the object elevation coordinate	rad
φ_p	elevation coordinate of the center of the pattern	rad
ψ	angular offset between the center of the pattern and the target	rad
ψ_s	spiral angle across time	rad
ω	angular frequency of the wave	rad s ⁻¹
ω_m	intensity modulation angular frequency	rad s ⁻¹
ω_0	angular frequency of the referent wave	rad s ⁻¹
Ω	curvilinear abscissa direction	
Ω_{AM}	angle of intensity modulation	rad

Contents

Acronyms	v
Symbols	vii
1 Introduction	1
2 LiDAR main concepts and designs	3
2.1 Accessing range	3
2.1.1 Frequency Modulation	4
2.1.2 Intensity Modulation	6
2.2 Making a line of sight 3D image	9
2.2.1 2D detector array	9
2.2.2 1D or quasi 1D linear detector array	11
2.2.3 Single element photodetector	12
2.3 Conclusion	13
3 Related systems for drone detection	15
3.1 Not laser-based	15
3.1.1 Passive radio-frequency and active RADAR	15
3.1.2 Acoustic sensor	16
3.1.3 Passive imagery	17
3.2 Active LiDAR	17
3.2.1 Flash, gated imager	18
3.2.2 Scanning LiDAR	18
3.3 Conclusion	19
4 Architecture and principle of operation of our LiDAR	21
4.1 Specifications and proposed solution	21
4.2 Coordinate system	23
4.3 Designing an optical architecture	24
4.3.1 Configurations available	24
4.3.2 Iterations and final architecture	25
4.3.3 Wavelength selection	27
4.4 Modes	29
4.4.1 Detection mode	29
4.4.2 Tracking mode	30
4.4.3 Intrusion mode	31
4.5 Conclusion	32

5	Static Model	35
5.1	3D Accuracy, precision and resolution	35
5.1.1	Beam width and lateral resolution	35
5.1.2	Pulse width and range precision	36
5.2	Extended link budget	37
5.2.1	Generic expression	37
5.2.2	Particular case of a lambertian target	40
5.3	Detection chain	41
5.3.1	Detector structure and binary hypothesis	41
5.3.2	Noise sources	42
5.3.3	False alarm rate	45
5.3.4	Probability of detection	48
5.4	Conclusion	50
6	Dynamic Models	53
6.1	Scanning optimization for detection mode	53
6.1.1	Probability of multiple echoes	53
6.1.2	Model simplification using the probability to detect a single echo	58
6.1.3	Impact of the target speed	62
6.2	Circle optimization for intrusion mode	64
6.3	Pattern optimization for tracking mode	66
6.3.1	Pattern equations	66
6.3.2	Patterns ranked as a function of the probability of intersection	68
6.4	Scanning frequency limitations	73
6.4.1	Light round-trip travel	73
6.4.2	Scanner bandwidth	74
6.5	Conclusion	77
7	Experimental platforms	79
7.1	Platform components	79
7.1.1	Laser source	79
7.1.2	Beam steerer	82
7.1.3	Photodetector	83
7.1.4	Beam separator & collimation optics	87
7.1.5	Bandpass filter & transmission coefficients	90
7.2	System overview and control electronics	94
7.3	Platform integration	96
7.4	Conclusion	99
8	Experimental results	101
8.1	Laser safety for field trials	101
8.2	Frequency limitations	102
8.2.1	Raster-scan for detection mode	103
8.2.2	Circle-spiral for detection mode	103
8.2.3	Lissajous for tracking mode	104

8.2.4	CLV spiral for tracking mode	104
8.3	Trials and results	105
8.3.1	03/2019 with the platform "beamsplitter"	108
8.3.2	02/2020 with the platform "parabolic mirror"	108
8.4	Imagery mode	117
8.4.1	3D point clouds	117
8.4.2	4D point clouds with signal intensity	117
8.5	Conclusion	119
9	Model predictions and experimental confrontation	121
9.1	Fitting tracking data	121
9.2	Extrapolation to detection mode	125
9.3	Extrapolation to intrusion mode	129
9.4	Conclusion	130
10	Conclusion	131
	Bibliography	133

Introduction

Misuse of civil drones, or unmanned aerial vehicle (UAV), has been a rising concern in the past few years. Their availability, low cost, high speed and usable payload makes them a serious threat for some restricted areas. They raise security concerns in airports because of potential of collision with aircraft [Gettinger & Michel 2015] and threaten government buildings and officials [Sturdivant & Chong 2017]. As a response, multiple systems specifically developed to detect, track and even neutralize drones have come to light [Birch *et al.* 2015]. Unfortunately, drones are a very challenging target, with a small, decimetric size and a large variability of shapes and behaviors. Moreover, they can be operated in an urban or a more open environment, meaning that perception algorithms must work with very diverse backgrounds. Reaching good performance can be done with a single, or more likely plural technologies, ranging from radio frequency (RF) to optics and even acoustics [Guvenc *et al.* 2018, Shi *et al.* 2018, Christnacher *et al.* 2016].

Complementary to these technical solutions, laser-based detection and imaging systems (light detection and ranging (LiDAR)) are currently getting more development and usage. This increasing popularity is directly linked to the recent need for more accurate, more resolved, cheaper and smaller 3D imagers for autonomous vehicles. The automotive mass market perspective has indeed been drawing component maturation and system development for the past few years [Hecht 2018]. The versatility, compact size, and potential kilometeric range of LiDAR systems make them a potentially viable solution to detect and track small and agile targets such as UAVs. The use of laser light allows for very precise and resolved three-dimensional localization, especially compared to other technological solutions.

LiDAR systems in themselves are rich in phenomenology. Shortly after the invention of the laser, large scale experiments were already conducted to get distance measurement for atmospheric studies [Fiocco & Smullin 1963]. The field expanded to aerosol and wind sensing [Vaughan *et al.* 1996], 3D topography [Shan & Toth 2018], and structural vibrometry [Lutzmann *et al.* 2011]. For this manuscript, we will focus on hard target imagery, which is the application of choice for current generations of LiDARs.

Flash LiDAR technologies use a 2D matrix detector (camera), which is electronically gated to detect the synchronized laser pulse only during the specified time gate. One interesting aspect of gated imaging is the ability to suppress background and foreground, making image processing algorithms more robust compared to full 2D images [Laurenzis *et al.* 2019]. But a major drawback is the very small field of view (FoV) accessible at the needed resolution to detect and recognize targets such as UAV at long range [Christnacher *et al.* 2016, Woods *et al.* 2019, Breiter *et al.* 2018]. To address a considerably wider FoV, there is always the possibility to multiply the sensors. Nevertheless, independent multi-sensor calibrations and fusion presents its own difficulties and is a current area of research [Kim *et al.* 2008], especially regarding autonomous vehicles.

Another option is to build the sensor on a dynamic pointing device such as a turret, but at

the expense of high cost and bulkiness for high reliability. Lastly, one can use a scanning **LiDAR**. Scanning **LiDAR** can be built on a variety of beam steering setups to sequentially scan a laser beam within a scene, producing a fully three dimensional image. Compared to flash **LiDAR**, the resolution between points and the **FoV** can be dynamically tuned, at the expense of a larger acquisition time.

During this thesis, we developed a scanning **LiDAR** aimed toward kilometric range detection and tracking of **UAV** at really high refresh rate. We aimed to keep the laser source as low power as possible to keep the platform light in cost, volume and security. We took advantage of the scanning device versatility to develop specific modes for both detection and tracking. A mode for detection of intrusion, based on a previous patent, was also implemented. The main interrogations, which served as the guideline of this thesis, is as follow:

- how to design a scanning **LiDAR** to detect such a small target at such a long range and high refresh rate?
- Which parameters are the most crucial to optimize its performance, and how are they linked together?

To answer this questions, we had to take a deeply multi-parametric approach. We studied each component, and merged the equations together to obtain global performance indicators, mainly in the form of the probability to get one or several echoes on the target. As such, each chapter is either a development to characterize individual sub-systems, or a progression toward the end goal of a global model applied to each mode. We also had the chance to develop a physical platform, which served as a reference point and allowed us to compare our models with experimental data. As a result, this document is divided into multiple chapters which address each step of our **LiDAR** system modeling and prototyping.

The manuscript is organised as follow:

- Chapter 2 covers the main concept of **LiDAR** systems.
- Chapter 3 details technical solutions regarding **UAV** detection and tracking, including **LiDAR**.
- Chapter 4 describes the principle of operation of our system, and each of its operating mode.
- In chapter 5 we study the static model of the system, including the link budget, the false alarm rate and the probability of detection.
- Chapter 6 exposes the dynamic models of our **LiDAR** scanner, in the form of pattern parameters of each mode, including the interaction with the **UAV** (size and speed).
- Chapter 7 is the description of the experimental platform, with a detailed analysis on each component, their performance and limitation.
- Chapter 8 presents the data gathered by our platform during two sets of trials regarding **UAV** detection and tracking.
- Finally, in chapter 9 simulations are run to compare our models with the experimental data.

LiDAR main concepts and designs

Contents

2.1	Accessing range	3
2.1.1	Frequency Modulation	4
2.1.2	Intensity Modulation	6
2.2	Making a line of sight 3D image	9
2.2.1	2D detector array	9
2.2.2	1D or quasi 1D linear detector array	11
2.2.3	Single element photodetector	12
2.3	Conclusion	13

Throughout LiDAR developments, researchers and engineers have sought to apply methods and processes that were already used in radio wave applications (radar), as both techniques use an electromagnetic wave emitter and receptor. Independently of its detailed structure, a LiDAR is composed of a single or plural laser emitter, a single or plural photodetectors and an optical emitting and receiving aperture. Once emitted, the laser light travels through the medium, usually the atmosphere, before reaching the scene to image. The light then scatters on the objects, and a portion travels back to the receiving aperture. It is this portion of light that must be processed to extract the range information.

This chapter is meant to give a description of the principles and technologies used in LiDAR system. More details can be found in various books [Richmond & Cain 2010a, McManamon 2019a] and articles [Horaud *et al.* 2016, Royo & Ballesta-Garcia 2019, Behroozpour *et al.* 2017, McManamon 2019b].

2.1 Accessing range

Light is a wave that, when emitted, propagates through a medium. Because the wave travels at the speed of light c (we consider a low density medium, like the atmosphere, such as the index can be approximated to 1), the wave instantaneous module and phase acquire an offset. The light complex amplitude E can be written in the form

$$E[t] = M \left[t - \frac{x}{c} \right] \exp \left(i \left(\omega_0 \left(t - \frac{x}{c} \right) + \phi \left[t - \frac{x}{c} \right] \right) \right), \quad (2.1)$$

with t representing time, ω_0 the angular frequency and x the traveled distance. The module M and the phase ϕ are written here as functions of time, as they can potentially be modulated. Range information is also contained in the frequency term, but because the light wavelength is in the order of the micro-meter, the 2π ambiguity makes it unusable for most applications.

Therefore it is dropped in the following equations of this manuscript. The light intensity I is proportional to the square of the amplitude $T \propto |E|^2$. With the wave equation detailed, we can review the different ways to access the range information.

2.1.1 Frequency Modulation

This method, which is the most complex, relies on light coherence. Most LiDAR systems employing this method for hard target detection use frequency modulated continuous wave (FMCW). The main principle is to chirp the laser optical frequency across time, using for instance a triangular frequency modulation. When the wave propagates in the medium, it acquires a phase delay proportional to the traveled distance. The laser angular frequency ω is modulated, rather than the phase ϕ . If we wish to use Eq. (2.1), we therefore have to write that $\phi[t] = \omega[t]t$.

Because of the very high frequency of visible or infrared light (terahertz band), working with the full waveform in the electronic domain like what is done with radar is impossible. Therefore, one needs to use the coherence property of laser light to create an optical interference pattern on the detector by superposing the reference wave, called the local oscillator, lo , with the backscattered one, ba . This process acts as a frequency subtraction between the waves, lowering the center frequency. Let ω be the modulated angular frequency, added to the referent angular frequency ω_0 . The coherent light amplitude subtraction produces on the photodetector a light intensity I of expression

$$I[t] \propto \left| M_{lo} \exp(i(\omega_0 + \omega[t])t) + M_{ba} \exp\left(i\left(\omega_0 + \omega\left[t - \frac{x}{c}\right]\right)t\right) \right|^2, \quad (2.2)$$

$$\propto M_{lo}^2 + M_{ba}^2 + 2M_{lo}M_{ba} \cos\left(\left(\omega\left[t - \frac{x}{c}\right] - \omega[t]\right)t\right). \quad (2.3)$$

If the frequency modulation used is a triangle wave of period T and peak-to-peak amplitude B_{fm} , then on the up-ramp, we have

$$\omega[t] = 2\pi \frac{2B_{fm}}{T} t. \quad (2.4)$$

If the system points at a single static target at a distance $R = x/2$, then the obtained electrical signal after optical interference contains a single intermediate frequency, f_{IF} of value $f_{IF} = 4RB_{fm}/(cT)$. If the target is moving, the frequency content of the backscattered wave is shifted due to the Doppler effect. This shift can be uncoupled from the distance in the intermediate frequency by analyzing the behavior in the up-ramp compared to the down-ramp [Pierrottet *et al.* 2008]. The range is then given by

$$R = \left(\frac{f_+ + f_-}{2} \right) \frac{cT}{4B_{fm}}, \quad (2.5)$$

with $f_+ = f_{IF} + f_d$ and $f_- = f_{IF} - f_d$, f_d being the Doppler shift. The object radial speed V_c is

$$V_c = \left(\frac{f_+ - f_-}{2} \right) \frac{\lambda}{2}, \quad (2.6)$$

with λ the laser wavelength. Therefore, a well designed FMCW LiDAR provides both range and speed information, at least in the illumination direction. These considerations are illustrated in Fig. 2.1.

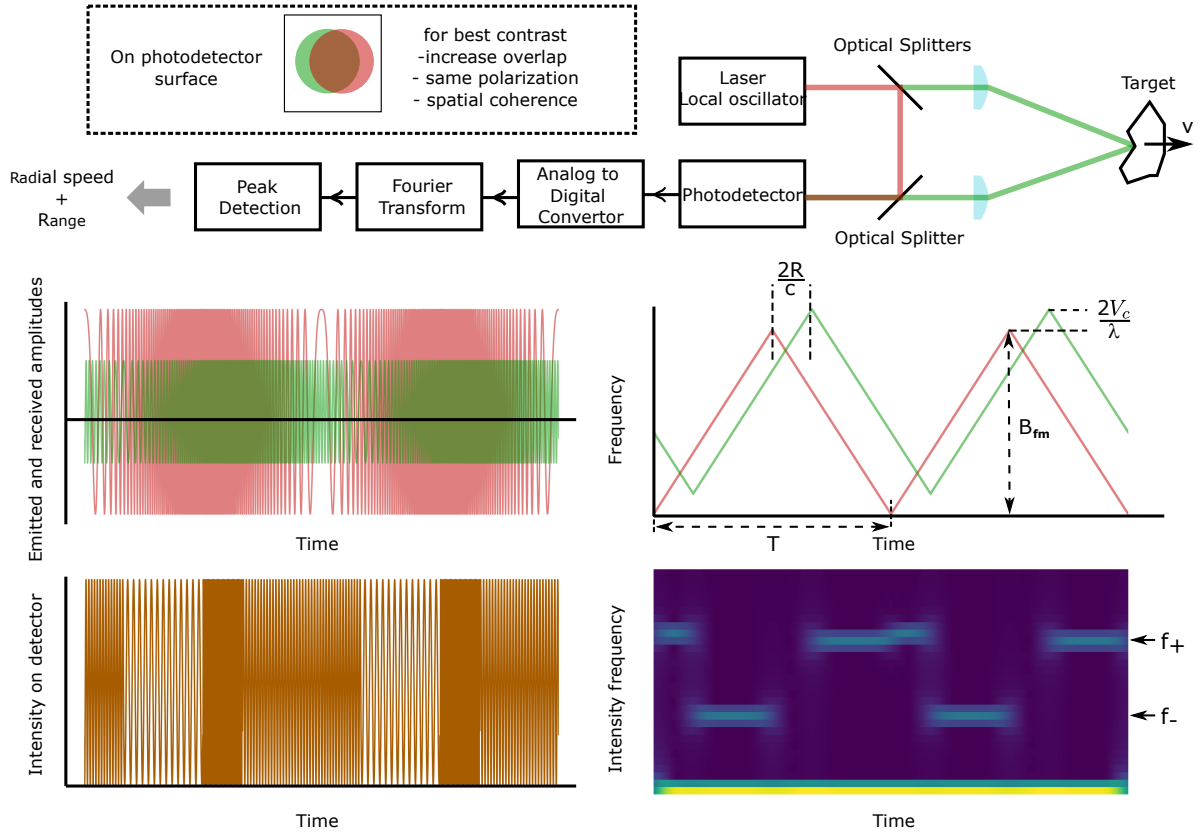


Figure 2.1: (Up) schematic of a FMCW LiDAR . (Down, up left) emitted (red) and received (green) light amplitude as a function of time for a distant moving target. (Down, up right) frequency content as a function of time for both amplitudes. (Down, down left) light intensity of the photodetector as a function of time, showing interference pattern. (Down, down right) Spectrogram of the intensity on the detector. Light color corresponds to strong signal strength.

Because of the speed information, **FMCW LiDAR** is a very interesting option. Moreover, it is based on light coherence, thus rejecting all other light sources that does not comes from the laser itself, including solar background. Yet to maximize the signal that can be exploited, the two beams must overlap, with as little wavefront and polarization distortion as possible. The alignment is thus very critical. Moreover, the modulated waveform linearity is a key factor for good signal to noise ratio (SNR) [Karlsson & Olsson 1999]. Because it is an indirect measurement, an important amount of processing must be performed to gather distance and speed. This can be done in the analog or digital domain, using for the latter appropriate analog to digital converter (ADC) and fast Fourier transform algorithms.

The laser line-width (the frequency spread of the optical wave frequency content) limits the maximum accessible range. After this distance, the return frequency gets too broaden and sink into noise. A kilometer range would for instance require a 100 kHz linewidth, which may be difficult to get across with compact laser diodes. Advanced signal processing can be used to improve detection at long range [Kim *et al.* 2018c], but the fundamental limits remains. The source stability is also impacted by other factors such as temperature and usage wear. Due to those strong requirements in linearity and line-width, limitations in average power for commercial products can inherently limits the maximum range. Because of these constraints and the overall complexity, **FMCW** was not the retained solution for the system developed during this thesis.

Finally, for wind sensing, pulsed - rather than continuous - coherent sources are used, with relatively long (a few hundreds of nanoseconds) pulse length. Coherent lasers are defined by a very narrow bandwidth, which is required to be able to extract information from the interference pattern between the emitted and received pulse. This notion of coherence is akin to the comparison of a two clocks, synchronized at a time t_0 , and then compared at a time t_1 . If clock frequency stability is poor (large bandwidth in case of a laser), then drift may cause both clocks to be out of sync, losing coherence. In the case of wind sensing, the laser wavelength is not chirped, but simply offseted by using for instance an acousto-optical modulator [Kameyama *et al.* 2007]. Therefore, range measurements can only be performed via pulse envelop detection, which yield poor range resolution due to large pulse width. Yet it allows for better decoupling between velocity and range compared to **FMCW**. The higher peak power also allows to reach much higher range while keeping a lower, more "eye-safe" average power.

2.1.2 Intensity Modulation

The other option is to modulate the module of the light wave. For this method, incoherent detection - or energy detection, is used. As explained before, the frequency of light is too high to be directly acquired by any electronics, and therefore photodetectors can only access the intensity envelope. To use a radio-wave analogy, the lightwave acts as a carrier frequency for intensity modulation distance measurement.

Amplitude modulated continuous wave In amplitude modulated continuous wave (**AMCW**) **LiDAR**, the intensity is modulated using a periodic signal. We wish to present here a way to extract range using direct signal multiplication and filtering, such as shown in [Melexis 2018]. Yet some commercial systems employ signal digitization to perform correlation between the reference and the back-scattered light intensity, using either cross-correlation or Fourier transform multiplication [Godbaz *et al.* 2012]. We present here a "lock-in" type of de-

tection, in which the reference and the back-scattered light intensity must be mixed, resulting in

$$U[t] \propto |M[t - \frac{x}{c}] \exp(i(\omega_0 t + \phi))|^2 |M[t] \exp(i(\omega_0 t + \phi))|^2 , \quad (2.7)$$

$$\propto M[t - \frac{x}{c}]^2 M[t]^2 , \quad (2.8)$$

$$\propto I[t - \frac{x}{c}] I[t] . \quad (2.9)$$

If the modulation is sinusoidal, then

$$I[t] = M_m \cos(\omega_m t) , \quad (2.10)$$

with ω_m the modulated angular frequency and M_m its amplitude. The direct and quadratic product U and V can then be written as

$$U[t] = \frac{M_m^2}{2} (\cos(2(\omega_m(t - \frac{x}{c}))) + \cos(\omega_m \frac{x}{c})) , \quad (2.11)$$

$$V[t] = \frac{M_m^2}{2} (\sin(2(\omega_m(t - \frac{x}{c}))) + \sin(\omega_m \frac{x}{c})) . \quad (2.12)$$

By using low-pass filtering or time integration to remove the time dependence, we obtain U_{filt} and V_{filt} :

$$U_{filt} = \frac{M_m^2}{2} \cos(\omega_m \frac{x}{c}) , \quad (2.13)$$

$$V_{filt} = \frac{M_m^2}{2} \sin(\omega_m \frac{x}{c}) . \quad (2.14)$$

In the end, we can extract the distance $R = x/2$ by computing the angle Ω_{AM} :

$$\Omega_{AM} = \arctan(V_{filt}/U_{filt}) = \omega_n \frac{2R}{c} , \quad (2.15)$$

$$\iff R = \frac{c\Omega}{2\omega_n} . \quad (2.16)$$

In most systems, to get a more accurate range, the algorithm (lock-in type or cross-correlation) is usually performed at 4 four different phase shifts. Increasing the angular frequency ω_m directly increases range resolution, but at the same time shortens the unambiguous range, i.e. the range at which a 2π period of the modulation is reached. For instance a 10 MHz modulation correspond to a maximum distance of a few tens of meters. Moreover, because of the filtering process, getting range with enough accuracy requires multiple waveform periods, which directly increases the time needed for each point. Eye-safety legislation also restricts the value of the laser light average power that can be emitted. In this direct detection setup, sensitivity is directly proportional to the power amplitude of the laser source, and inversely proportional to the noise floor of the detection chain. A example of architecture of a [AMCW LiDAR](#) is shown in Fig. 2.2.

Because of these aforementioned arguments, most commercial applications are limited to very short distances, usually ten meters, or the size of a room. Silicium-based detector arrays are usually used, coupled with near-infrared LED rather than lasers [[Royo & Ballesta-Garcia 2019](#)].

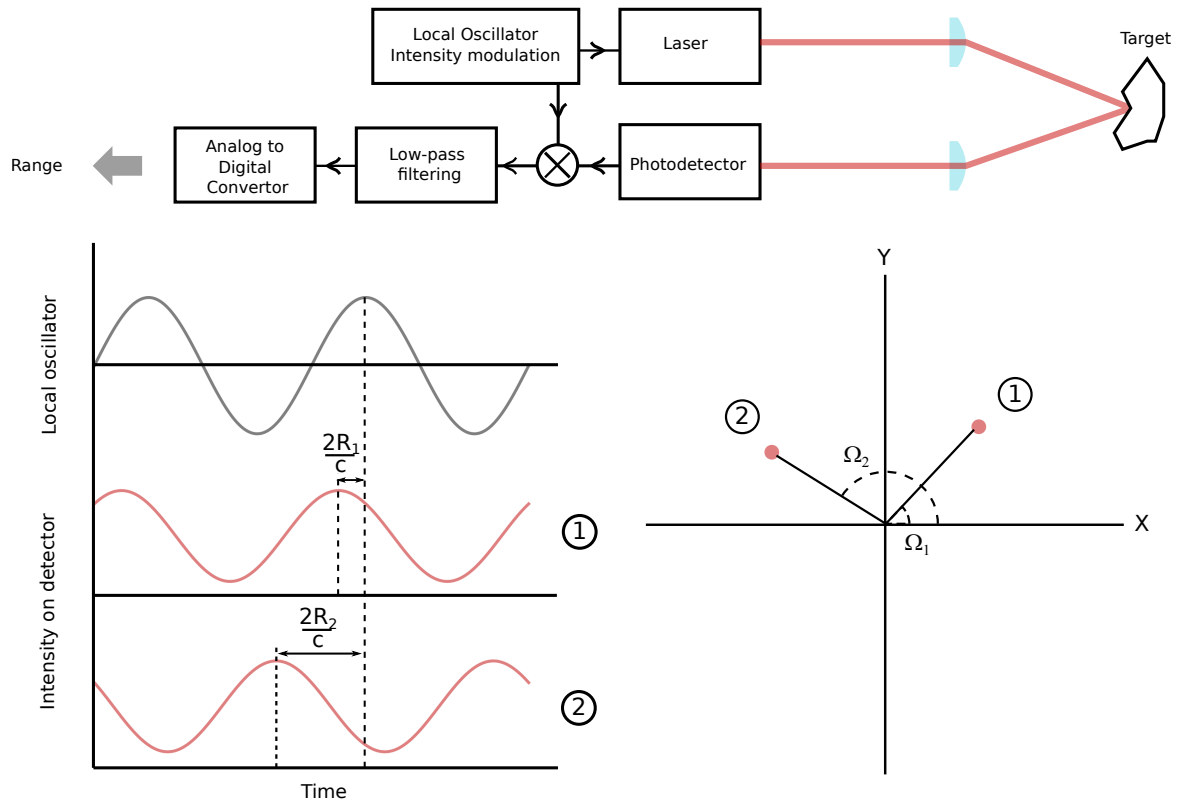


Figure 2.2: (Up) schematic of an [AMCW LiDAR](#). (Down, left) local oscillator (black) and received (red) light intensity as a function of time, for two different ranges R_1 and R_2 . (Down, right) XY plane representation of the filtered product. R_1 and R_2 can be deduced from the respective value of Ω_1 and Ω_2 .

Pulsed time of flight The second, most common form of intensity modulation is very certainly the pulsed time of flight (ToF) LiDAR. In this method, the laser emits a very short laser pulse. By acquiring the time difference between the emitted and received pulse, it is possible to perform a direct distance measurement with $R = c\text{ToF}/2$. Usually, to get as much peak power as possible while keeping a reasonable photodetector bandwidth, pulse duration is in the nanosecond range [Behroozpour *et al.* 2017]. Compared to AMCW, the narrow pulses allows for high peak power while keeping a low average power, therefore keeping up with the eye-safety limit.

Pulse time-stamping can be done by processing the digitized return waveform, yet this approach requires a very high sampling rate digitizer and heavy data computation for real time application. Most systems uses fast analog triggering electronics [Chevrier & Campanella 2016]. Compared to the FMCW, the technique is sensitive to other light sources, most importantly the solar background. The use of a narrow bandpass optical filter can help mitigate its impact. Moreover, range accuracy is not a function of the modulation bandwidth like with FMCW or AMCW, but is limited by rising edge or pulse centroid detection precision, adding to jitters within the electronics. Changes in amplitude, or pulse broadening can therefore create pulse walk [Williams 2017], which needs to be compensated. For those reasons, the overall ranging performance is usually in the centimeter range at best. Schematic of a pulsed LiDAR is presented in Fig. 2.3.

2.2 Making a line of sight 3D image

Once we viewed the main options to retrieve distance, we can address the way LiDAR systems create a 3D image. There are three main types of LiDAR : staring, scanning, and hybrids. Each design possess its own advantages and drawbacks, but the core constraint is often the choice of detector, which limits either the FoV or the resolution. Therefore, we choose here a presentation based on the detector type.

2.2.1 2D detector array

The detector can be comprised of a 2D array of pixels, working just like a camera, except it can perform range measurements. For FMCW and AMCW, the illumination is continuous. For pulse ToF, the illumination is pulsed, and the resulting system is called a flash LiDAR. In flash systems, the whole scene can be theoretically acquired in a single nanosecond flash, providing high refresh rates and a "frozen" image of the scene. Independently of the range method used, the laser has to illuminates the full FoV seen by the 2D array. Because of the loss in energy density, which squares with the FoV to cover, the maximum available range shortens very quickly. Moreover, the threshold for eye-safety also limits the laser power. An illustration of a flash LiDAR design is shown in Fig. 2.4.

The array pixel density and size brings its own limits regarding the compromise between FoV and resolution. In the NIR wavelength, around 900 nm, charge-coupled device (CCD) or complementary metal-oxide-semiconductor (CMOS) silicium based arrays are widely available at a low cost. They are mainly used for AMCW LiDAR, with specialized electronics to allow for light demodulation, such as the 320 x 240 pixels of [Melexis 2018]. The same type of detector could potentially be used for FMCW LiDAR, but processing the MHz intermediate beat frequency requires specialized electronics and signal processing functions that is very complex to implement

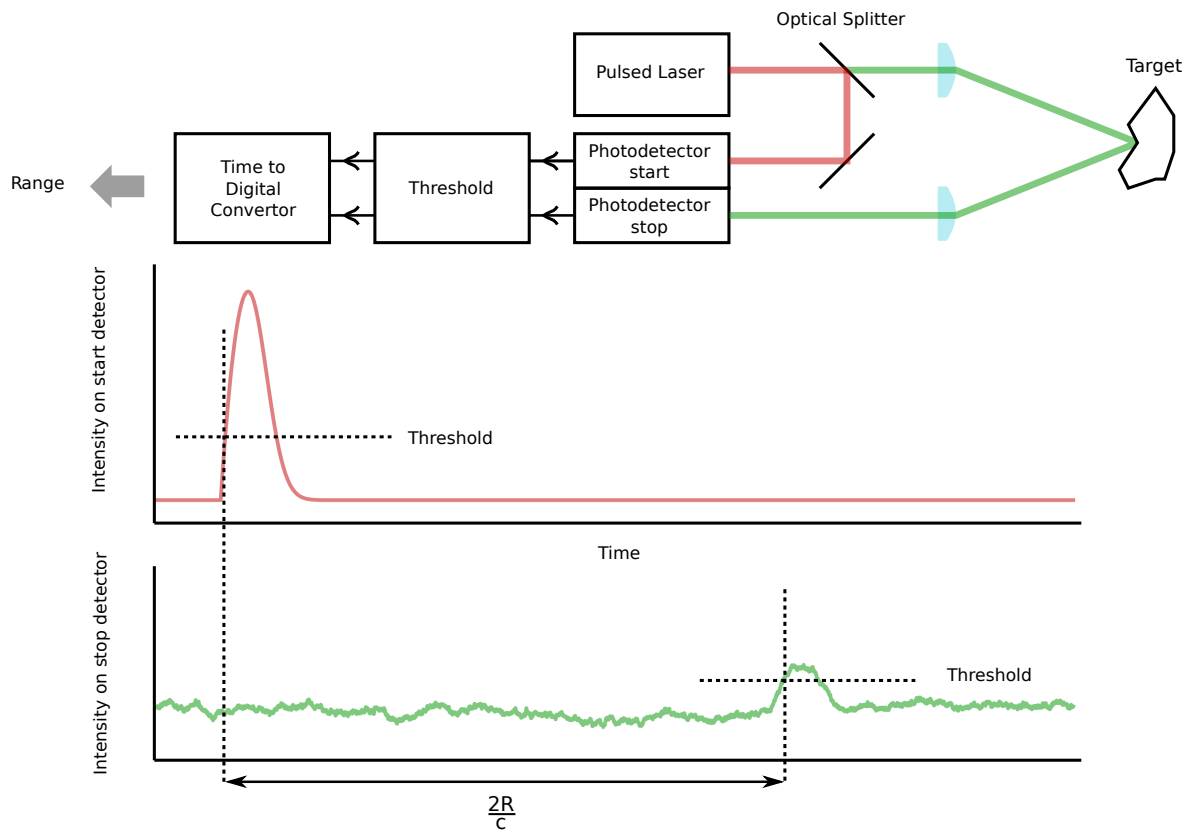


Figure 2.3: (Up) schematic of a pulsed LiDAR. (Down) emitted (red) and received noisy (green) light intensity as a function of time. Thresholding and time-flagging directly give access to target range.

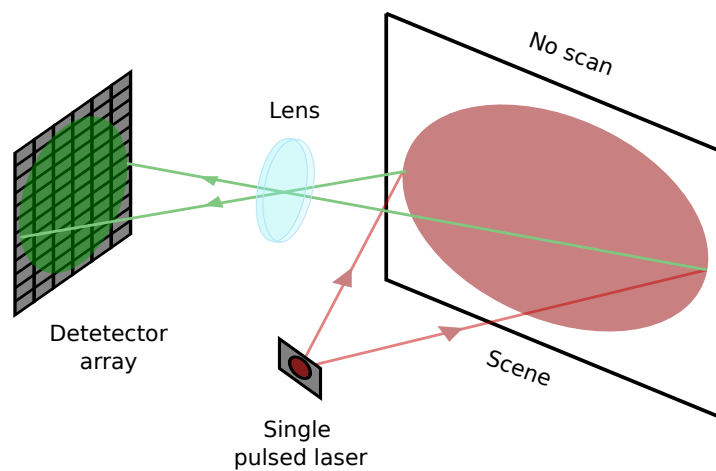


Figure 2.4: Illustration of a flash LiDAR with a single pulsed emitter and a 2D detector array.

on such a huge number of pixels. To the best knowledge of the author, a full 2D array for **FMCW LiDAR** has not yet been realized with more than a few pixels. A workaround must be found to increase pixel resolution, like using an **AMCW** camera [Mitchell *et al.* 2019].

For pulsed flash **LiDAR**, the constraint is even higher, as a true ToF system with centimetric accuracy requires a high bandwidth photodetector and amplifier including a very high speed readout integrated circuit (**ROIC**). Another option is to directly link the output of the photodetector to a digital electronics, bypassing the **ROIC**, but lowering either the dynamic range or the sensitivity of the device [Horaud *et al.* 2016]. To increase the SNR, extremely sensitive arrays of detectors are usually used in this direct detection setup. In the NIR wavelength, which is the most widely used for current automotive **LiDAR**, silicon avalanche photodiode (**APD**) is the component of choice. An emerging trend sees the use of arrays of silicon photomultipliers (**SiPM**) [Agishev *et al.* 2013], which are constituted of **APD** biased beyond their breakdown voltage, and are able to detect a single photon event. They are also called single photo avalanche diode (**SPAD**) or Geiger-mode **APD**. With any single photo detector, there is a short time period (at the very minimum 100 ns) after each detection where the detector is blinded, called dead time. Moreover, a phenomenon called after-pulses increases the false alarm rate right after this dead time, for a short period. Therefore, operation in a photon-rich environment such as daytime can be very challenging.

To alleviate eye-safety constraints for longer range system, it is possible to operate in the short-wavelength infrared, 1400 - 3000 nm (**SWIR**) band. At this wavelength, light does not penetrate cornea and therefore damage appears at higher power density. In this waveband, commercially available arrays can be based on HgCdTe, which must be cooled, or on the more used indium gallium arsenide (**InGaAs**) crystal. **APD** arrays on these materials are commercially available, reaching resolutions of 512x640 pixels [Rutz *et al.* 2018]. Unfortunately, properly implementing **ROIC** able to time the nanosecond returning pulse seems, at current time, too complex to be done on such an important amount of pixels. To alleviate that constraint, these arrays are used for **ToF** application by applying an electronic shutter on the **ROIC**, so as to only accept light flux coming from a specific distance slice on the scene. Gate width is often in the tens of nanosecond order, which means a distance resolution of few tens of meters. Because these cameras usually run at a few tens of hertz, varying the gate center image after image can be done to improve the range resolution of the image [Wu *et al.* 2011], while keeping refresh rate relatively high. Increasing range resolution has also been demonstrated using diverse compress sensing algorithms [Laurenzis & Woiselle 2014].

2.2.2 1D or quasi 1D linear detector array

With a 1D detector matrix, the laser light must illuminate a horizontal or vertical band of the scene, which is then swept across the orthogonal direction to produce the 2D image. Therefore, a beam steering component must be used. This setup is most often used for direct pulse detection, as the lower number of elements allows for implementation of high-bandwidth **ROIC** for real, direct pulse **ToF** measurements [Yang *et al.* 2019]. Such a setup also allows to increase laser power density on the scene, as the instantaneous FoV will be smaller than for a 2D array. The loss in **FoV** must be compensated by the beam steerer, but scanning a single dimension may be acceptable and causes less wear than scanning in 2D [Imaki *et al.* 2015]. Like previously mentioned, the technology is more mature, widespread and provides better performances in the

near infrared, 750 - 1400 nm (NIR) with silicon (Si) components than in the SWIR with InGaAs components.

Another solution commonly seen, most notably in systems developed by the company Velodyne, is the use of one or more linear array of both laser emitters and receivers. Each laser is coupled to its single element photodetector in a vertical arrangement. The resulting system illuminates a vertical band, and is rotated in the horizontal direction to generate a 360° point cloud. The resolution on the other direction is given by the number of elements within the line FoV [Hall 2011]. Ouster LiDAR systems also employ this design, except that they are using microelectromechanical system (MEMS) mirrors instead, increasing compactness and lowering power consumption [Pacala & Fritchl 2019]. Another solution is to electronically scan a 2D detector array, the rows being addressed sequentially. Therefore a way lower number of ROIC and timing electronics is needed for accurate pulse detection, as they can be sequentially routed to the active pixels. Such a method can be called quasi 1D. An illustration using a MEMS is shown in Fig. 2.5.

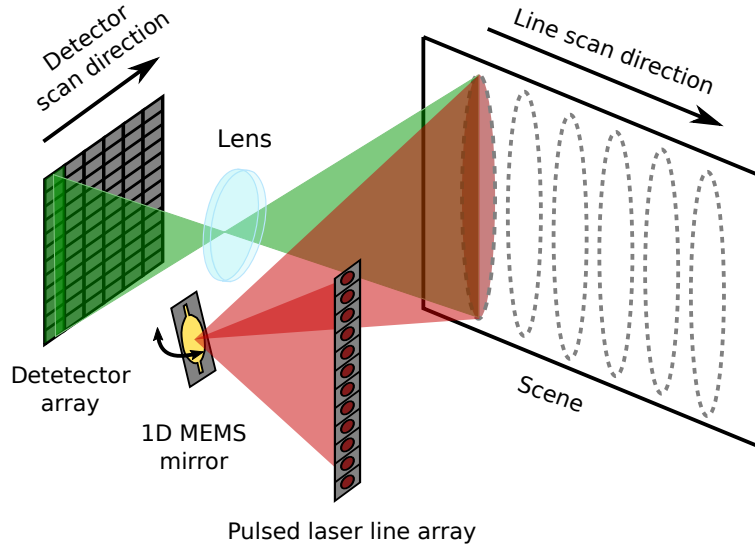


Figure 2.5: Illustration of a mixed-approach with a pulsed laser line array, a 1D MEMS mirror scanner and a synchronized electrically scanned 2D detector array.

2.2.3 Single element photodetector

LiDAR comprising of single element photodetector are referred as purely scanning LiDAR. In this architecture, a narrow laser beam is continuously swept across the FoV. Each position of the beam scanner is stored to sequentially reconstruct the image. This method can provide both a long range, a wide FoV, and a high resolution depending on the scanner performances. 2D beam steering can be realized with a number of solutions such as mechanical galvanometers [Nguyen *et al.* 2017b] or non-mechanical MEMS mirrors [Yoo *et al.* 2018], rotating polygons [Sato *et al.* 2010] or prisms [Zhu 2017], and even solid-state photonics phase array [Eldada 2018]. Each one of these beam steerers can be clustered into different applications depending on their size, cost, mechanical bandwidth, laser power handling, access to position feedback and aperture.

We can make a comparison of main available technologies that can be used for 2D beam steering. We exclude rotating polygons due to the fixed scanning pattern that they produce, as we want to have more scanning freedom (see operating modes of chapter 4). The comparison is displayed in Table 2.1.

	MEMS mirrors [Wang <i>et al.</i> 2020]	OPA [Poulton <i>et al.</i> 2017]	Galvanometer mirrors [Aylward 2003]
FoV	Medium to high ($\geq 10^\circ \times 10^\circ$)	Medium to high ($\geq 10^\circ \times 10^\circ$)	High ($40^\circ \times 40^\circ$)
Aperture	Small (few millimeters)	Small (few millimeters)	Large (up to several centimeters)
Bandwidth	High (≥ 1 kHz)	Very high (≥ 10 kHz)	Medium (up to the kHz depending on size)
Size - Weight	Low	Low	High (bulky)
Control type	Open loop	Open loop	Closed loop
Maturity level	Medium at mm size (micro-mechanics)	Low (photonics)	High (actuator)

Table 2.1: Comparison of the three main beam steering technologies for a mono-static design.

We can see here that each technology possess its strength in terms of aperture, bandwidth, size or consumption.

Coming back to the scanning principle, another advantage of scanning LiDAR is the photodetector. Single element photodetectors are cheaper, usually more sensitive and more widely spread than arrays. Nevertheless, when considering a single source and single detector, flash LiDAR sensor will always have a far greater refresh rate at the equivalent FoV and resolution. Moreover, very intensive data processing may be required to analyze hundreds of thousands of 3D point clouds in real time, requiring advanced hardware and software. At last, designing a scanning LiDAR to meet given requirements in angular resolution, refresh rate, range and FoV is a complex problem, as most parameters critically depends on each other [Quentel *et al.* 2019]. A monostatic scanning LiDAR implementation is shown in Fig. 2.6.

2.3 Conclusion

Range can be retrieved in two main ways. Firstly, one can rely on optical frequency modulation and interferometry, using continuous laser source (FMCW). The main drawbacks for long range are source power, coherence length and linearity, as well as a complex optical architecture and alignment. Decoherence effect produced by atmospheric turbulence, target surface roughness and other aberration can also significantly impact long range performance [Cao *et al.* 2020]. Coherent pulsed laser sources are unfit for proper LiDAR imagery because range can only be obtained using the ToF of the 100 ns or more pulse envelop.

The second technique is to use intensity modulation. Using modulated continuous waves (AMCW) for long range requires a very high average power and very good linearity, which is

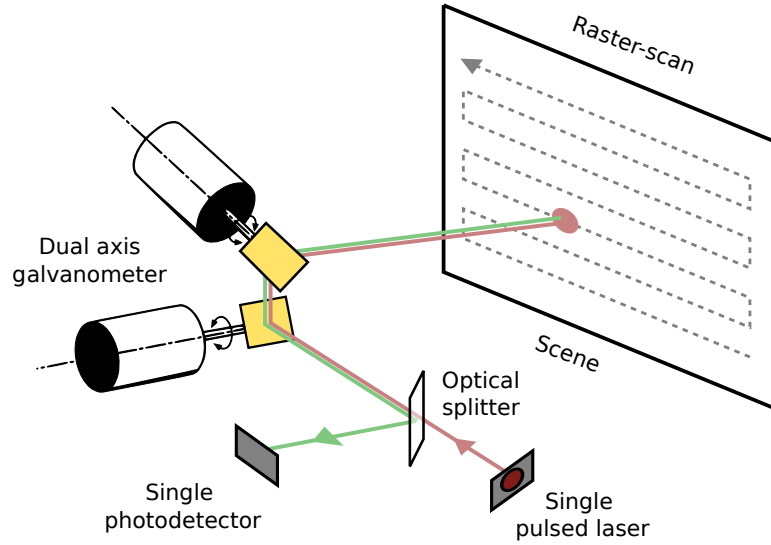


Figure 2.6: Illustration of a 2D scanning LiDAR using two galvanometer mirrors. The configuration is monostatic with a single laser emitter and a single photodetector.

difficult to come across. On the contrary, high peak power laser sources with nanosecond pulse widths are readily available for a ToF architecture. Because of its simplicity of implementation and long ranges performance, the pulse ToF LiDAR was the retained solution for our system.

Concerning the imagery method, commercially available arrays of ToF sensors with materials other than silicon lack the maturity to provide a large pixel count, therefore providing a poor ratio between FoV and resolution. For ease of implementation and performance, we chose to rely on a single photodetector and a dual-axis beam steering component, realizing a scanning LiDAR. More details on the architecture are given in chapter 4.

Related systems for drone detection

Contents

3.1 Not laser-based	15
3.1.1 Passive radio-frequency and active RADAR	15
3.1.2 Acoustic sensor	16
3.1.3 Passive imagery	17
3.2 Active LiDAR	17
3.2.1 Flash, gated imager	18
3.2.2 Scanning LiDAR	18
3.3 Conclusion	19

Multiples options has been consistently used for remote, automated detection and tracking of drones or UAV. They indeed represent a challenging target in terms of size, speed and variability of behavior. Moreover, they can be operated in an urban or a more open environment, meaning that perception algorithms must work with very diverse backgrounds. Multiple acousto-electro-optical solutions have been developed to provide a solution to this problem, including LiDAR systems.

3.1 Not laser-based

This section describes the state of the art of UAV, drones, and more generally small, agile targets detection and tracking using systems other than laser-based. A selection of examples and systems is provided here, but more details can be found on the following articles [Guvenc *et al.* 2018, Shi *et al.* 2018, Kim *et al.* 2019, Birch *et al.* 2015].

3.1.1 Passive radio-frequency and active RADAR

The RF domain extents from 3 kHz to 300 GHz. Amateur commercially available UAV are operated using a remote controller operating in the RF domain. By spying this link, it is possible to detect and track the UAV using a completely passive system. In the same waveband, an active radar emits and receives its own RF waves to detect and image the target. Inherently, a radar or a passive RF system has much less resolution than a LiDAR. Exactly like with a laser, the wave emitted or received by an antenna retains coherence properties. Diffraction theory shows that the full angle beam divergence Θ_b can be given in order of magnitudes by:

$$\Theta_b \propto \frac{\lambda}{D_r} \text{ [rad]} , \quad (3.1)$$

with λ the wavelength, and D_r the aperture. In the NIR, at a $1 \mu m$ wavelength, a laser of 1 cm of diameter at the exit of the system produces a beamwidth of 0.006° . This represents 10 cm at 1 km. With RF systems, the aperture is complex to accurately compute. The beam divergence can instead be derived from the value of its directional gain G_i relative to an isotropic antenna by the approximate formula

$$\Theta_b = \sqrt{29000/G_i} [^\circ] . \quad (3.2)$$

To give an order of magnitude, a 20 dBi antenna, such as the one used for RF drone detection in [Nguyen *et al.* 2017a], produces a beamwidth of around 20° . This is the raw lateral resolution of the system, considerably lower than in the optical domain.

The advantage of the passive RF option is the relatively inexpensive components compared to the other solutions. Yet, non trivial line of sight and multipath propagation must be carefully studied to acquire the distance with a single receiver. Detection was experimentally demonstrated on distances of several hundred of meters [Nguyen *et al.* 2017a]. The main difficulty resides in isolating the correct frequency band and channel and keeping tracks of potential hopping sequences on the carrier frequency [Shin *et al.* 2015]. Moreover, there are many types of hardware and software implementations across manufacturers and models. The control on older model can be analog, using a ten of MHz carrier frequency, or digital in newer model using classical Wifi band of 2.4 or 5.8 GHz, or even dual-band [Haluza & Čechák 2016]. Adding the likely presence of other communications channels (from GSM, Wifi, radio, etc...) sinking the signal into noise, it is easy to see how challenging of an approach it is. Nevertheless, recognizing the drone model is possible if a data bank was previously built. The team from [Farlik *et al.* 2019] showed diverse drone identification from up to 1400 m. Jamming the communication link once detected is also available with a correctly tuned emitter.

To improve accuracy and detection range, radar systems must be employed. Radar have very good penetration in bad weather (rain, fog, etc...), and can be operated during the night. By exploiting doppler effect like with the FMCW LiDAR, radar gets access to the instantaneous target speed. The main challenge that must be faced is the low radar cross-section of drones, and their low speed compared to usual radar targets. Drone discrimination against noise and clutter was shown to be improved by using micro-Doppler signatures in a multistatic configuration [Hoffmann *et al.* 2016]. In [Caris *et al.* 2015], a 94 GHz radar (mm wave) was shown to produce a 15 cm range resolution, and was able to track target from 10 m up to several hundreds of meters. Finally, we can cite here experiments with DJI Phantom 2 and a radar prototype showing a maximum detection range of about 3 km [Farlik *et al.* 2016].

Nevertheless, it should be stated that strong radar signals may not be suitable for a continuous urban use. Day long operation could potentially disrupt electro-sensitive equipment. Moreover, radar systems used in civil area should comply to exposure limits within the norm of the country [ICN 1998], which could limit its accessible power and thus maximal range. These constraints are obviously shared with active LiDAR systems.

3.1.2 Acoustic sensor

When flying, drones produce a very recognizable buzzing sound due to its electric propellers. Therefore, and as demonstrated up to 800 meters in [Benyamin & Goldman 2014], it is possible to use acoustic sensors to detect and track these types of UAV. In this paper, a single tetrahedric

array of 4 sensors was used. By using this array instead of a single detector, coherent beamforming techniques were used to increase the aperture (see Eq. (3.1)) and to considerably improve resolution, even with the kHz wave frequency. It was comparable to a GPS tracker within a 10° accuracy. Authors of [Busset *et al.* 2015] proposes a more complex set-up using an "acoustic camera" comprised of a sphere of 120 sensors. The given angular resolution is 0.5°, and maximum range in a urban environment is given at around 300 m for the DJI Phantom 2. Reliability of the detection can be improved by using a data bank of known signatures.

The main drawback of the system, as discussed in both articles, is the surrounding noise. Whereas it comes from busy roads or helicopters, it can sink signal into noise, even with the use of dedicated bandpass filters [Benyamin & Goldman 2014]. Nevertheless, it is a purely passive solution, using relatively cheap components, and which can be operated at night. Using the coherence properties of sound wave, a multistatic acoustic receiver could potentially increase both range and angular precision, and could be an option for site surveillance.

3.1.3 Passive imagery

Camera and image processing are a natural solution for UAV detection and tracking, as they are used in most generic surveillance systems. Algorithms can use either, or both, features characteristics and motion [Zhang *et al.* 2016]. Apart from stereoscopic, multistatic systems using multiple cameras, the data produced is only 2D, and therefore there is no access to range. As mentioned with flash LiDAR, the compromise between scene resolution and FoV coverage is set by the matrix size, number of elements and the optics focal length. To improve the system, multiple cameras with multiple FoV can be employed. The first, wider FoV camera can be for instance dedicated to rough detection of potential objects, which can be refined with the smaller FoV, higher resolution camera. Of course, such a set-up would require mobile elements such as point-tilt systems, which can heavily increase the total price.

Camera are very widespread, and therefore relatively cheap. Image processing algorithms for detection, recognition and tracking are also been developed for decades, therefore the field is mature. Another advantage is the high precision of camera compared to RF-based system, as it relies on light wave with a lower diffraction limit. The main drawback of passive imagery is poor performances in lower visibility scenario such as foggy, rainy, clouding weather and during the night. Using infrared camera help with penetration through obscurants [Kim *et al.* 2018b], but resolution is limited and price is usually high. Non line-of-sight imaging is also a challenge in most urban environment.

3.2 Active LiDAR

As seen previously, no stand-alone solution seems ideal to detect and track UAV. Each have its own advantages and drawbacks. To improve global performances, LiDAR was therefore tested as a complementary sensor. Compared to passive imagery, the system can work in degraded weather or during the night, and produces range information. Because it is an active system, signal to noise ratio is expected to be better than for passive systems such as RF and acoustic sensors, while being more resolved due to optical wavelength. Resolution will be better compared to radar, but non-line of sight imaging is not possible, and bad weather scene penetration is lower.

Moreover, laser based systems must be limited in power due to eye-safety regulation, therefore a long range system may not be suitable in populated areas.

We describe here two types of **LiDAR** applied to this specific application. One use gated imagery, and the other a scanning mechanism.

3.2.1 Flash, gated imager

Flash, gated imagers usually operate in the IR region. For eye-safety consideration, the wavelength of predilection is often in the **SWIR**, close to 1500 nm to maximize usable peak power. Flash imagers are made with a 2D matrix detector (camera), which is electronically gated to detect light only during the specified time gate. Used with a flash laser, it is possible to acquire a range slice of a few tens of meters wide. Apart for signal to noise ratio and night operation, another interesting aspect of gated imaging is the ability to suppress background and foreground, making image processing algorithms more robust compared to complete 2D images [Laurenzis *et al.* 2019].

As an example, we can cite here a cryocooled, 640x512 pixels, 15 μm pitch gated HgCdTe APD camera to identify diverse targets [Breiter *et al.* 2018]. The camera FoV is $0.9^\circ \times 0.7^\circ$ and is able to resolve a 2.5 cm object at 1 km. The flash system is mounted on a motorized tripod and is the zoom relay option of a wider FoV ($6^\circ \times 5^\circ$), passive camera in the mid-wavelength infrared, 3000 - 8000 nm (**MWIR**) region. With this type of resolution, long range drone recognition is possible. Nevertheless, tracking quality will heavily depends on the mechanical response of the tripod, as the camera FoV is very narrow and must be constantly tilted to follow the drone trajectory. A similar demonstrator can be cited here, specifically dedicated to drone detection and tracking [Christnacher *et al.* 2016]. The authors used an EBCMOS **InGaAs**/indium phosphide (**InP**) camera of 640x480 pixels, with a FoV of $0.9^\circ \times 1.2^\circ$, mounted on a pan and tilt device. An EBCMOS camera is comprised of at least two major layers: one photocathode, and one CMOS thinned layer. Here a **InGaAs**/InP photocathode is used to convert incidents photons of the **SWIR** band into electrons, which are accelerated by several kV of static electric field into the backside CMOS layer, acting as the final array of pixels. The sensitivity of this sensor is close to the single photon. The measurements show tracking improvements over conventional camera while the drone was flying in front of a forest, because the background disappear with gated imaging. Kilometer range was also disclosed with this system.

At last, the authors of [Woods *et al.* 2019] used a 32x32, Si based **SPAD** array in a **LiDAR** system, light sensitive from a wavelength of 0.3 to 0.9 μm . On the same optical axis, the **SPAD** array was coupled to a passive thermal camera sensitive from 8 to 12 μm . The thermal camera is used for detection of object of interest in a relatively large FoV, then transitioning to **LiDAR** for a higher resolution depth map. The optronics head is mounted on a gimbal turret. Depth resolution was disclosed to be 50 cm, with a small **LiDAR** FoV of 0.1° and a 100 Hz refresh rate. Detection of a fixed-wing **UAV** was performed at 1.5 km. Other images were acquired with a **LiDAR** operating in the **SWIR** for eye-safety considerations.

3.2.2 Scanning LiDAR

Conversely, scanning **LiDAR** systems are less employed for drone and **UAV** detection. The main advantage of scanning **LiDAR** is the considerably wider addressable FoV compared to flash imager, at the expense of acquisition time if image resolution is kept equal. Therefore at first

glance, the system does not seem to be adapted to the detection of agile and small targets. But prototypes and commercial systems are developed to challenge this idea. All systems described here are pulsed ToF based.

The OPAL product from Neptec was tested and shown to be able to detect a drone up to 600 m [Church *et al.* 2018]. The design is based on rotating prisms, and was able to achieve detection while scanning 30° of FoV at a refresh rate lower than 1 Hz. The pattern drawn is a rose with an uneven laser point density across the scene. Detection was performed when at least two echoes were found originating from the same localization, as a mean to filter false alarms. Another demonstrator developed by Hanwah systems aims to reach the 2 km range. They propose a scanning LiDAR system able to cover a FoV of 350°x120° while able to focus on a FoV of 0.5° to increase resolution [Kim *et al.* 2019]. The system is based on 1 kHz bandwidth galvanometer mirrors, and mounted on a gimbal to reach this wide FoV. Resolution is very high, reaching 0.003°x0.025°. Data processing is more intensive than with the Neptec demonstration and is based on neighbor clustering to segment the scene and track the target among the noise [Kim *et al.* 2018a].

At last, another approach is to use commercial scanning systems targeted toward automotive industry. One team used Velodyne 360° rotating scanning LiDAR with both 64 and 16 lines mounted on a vehicle to detect and track an UAV [Hammer *et al.* 2018]. Detection range is very limited with this set-up, only up to 50 m. Vertical resolution is 0.4°, while horizontal resolution is 0.17° for the 64 lines, and 2° for the 16 lines. Due to the low resolution, even at this close range, the system has to rely on less than 10 points for clustering. Identification of the UAV was therefore challenging and false alarms were complex to sort due to the amount of other objects on the scene.

3.3 Conclusion

We propose on Table 3.1 a summary about existing technologies able to detect and track drones. Unfortunately, precise range, FoV and overall performance are difficult to come by, even in the literature. Moreover, the scale of some systems compared to more modest setups can induce a comparative bias (for instance comparing a 100 m range scanning LiDAR for automobile compared to a military oriented 2 km range flash LiDAR). To this effect, the candidate tried to use sources describing systems specifically oriented toward drone detection, and based on a single technology, as the one described previously. This summary is also inspired by multiples reviews [Guvenc *et al.* 2018, Birch *et al.* 2015, Taha & Shoufan 2019, Shi *et al.* 2018].

Commercial drone detection systems are often based on a plurality of technical solutions, especially passive imagery and radar. The use of LiDAR for this application is more marginal, which can be explained by the cost of high performing systems and the potential eye-safety issues. Nevertheless, as discussed in chapter 4, we propose to take full advantage of the high resolution and dynamic performances of a scanning LiDAR to answer specific requirements.

	Localization method	Drone signature	Advantages	Limitations
Acoustic	TDOA with a microphone array	Propellers sound frequency with drone database	Low cost	High ambient noise, heavy processing for accurate localization/recognition, low range
Radio frequency	DOA , signal intensity	Communication channel with drone database	Low cost, recognition by drone communication signature	RF link drone dependant, heavy processing for accurate localization (multi-path propagation), drone in autonomous operation not detectable
Radar	Delay based localization, doppler for instantaneous speed	Micro-doppler, Radar cross-section	Non line of sight imaging, can be operated in adverse (fog, rain, night, ...) conditions, high range	High cost, low drone RCS and altitude, low resolution implying difficult identification
Passive visible imagery (VIS, NIR)	2D Pixel coordinates on array, stereoscopy for 3D	Features detection	Low cost, recognition with image processing mature, high 2D resolution with adequate optics	Fixed ratio FoV /resolution, line-of-sight only, performances reduced in adverse conditions, low range precision via stereoscopy
Infrared passive imagery (SWIR, MWIR, LWIR)	2D Pixel coordinates on array	Features detection	High 2D resolution with adequate optics, good penetration in obscurants and night operation	High cost, fixed ratio FoV /resolution, line-of-sight only, low resolution sensor, weak drone thermal signal
Flash LiDAR	2D Pixel coordinates on array, delay based localization with ToF or gating	Features detection, laser cross-section	High 2D resolution with adequate optics, excellent penetration through obscurants and night operation, high range	High cost, fixed ratio FoV /resolution, line-of-sight only, low resolution sensor
Scanning LiDAR	Beam steerer positioning, delay based localization	Features detection, laser cross-section	Very high range resolution, penetration through obscurants depending on wavelength and night operation, high range	High cost, scanning time to cover wide FoV , resolution limited by beam footprint, line-of-sight only, eye-safety concerns

Table 3.1: Comparison table between technologies for drone detection and tracking.

Architecture and principle of operation of our LiDAR

Contents

4.1	Specifications and proposed solution	21
4.2	Coordinate system	23
4.3	Designing an optical architecture	24
4.3.1	Configurations available	24
4.3.2	Iterations and final architecture	25
4.3.3	Wavelength selection	27
4.4	Modes	29
4.4.1	Detection mode	29
4.4.2	Tracking mode	30
4.4.3	Intrusion mode	31
4.5	Conclusion	32

4.1 Specifications and proposed solution

The purpose of our **LiDAR** system is to detect and track small, agile targets such as drones at a long, kilometer range as well as close range. The system must have precise positioning, lower than the target dimensions, and should be able to refresh the target position at a high rate during tracking. High dynamic ranges are required, in terms of target range, acceleration, speed and trajectories. We wish to respect the specifications shown in Table 4.1, in order of importance.

The angular accuracy is partly constraining, but good quality beam steering systems can have a much better resolution than what we want to achieve. The real constraint for a scanning **LiDAR** is the refresh rate. Conventional imagery of a large **FoV** with enough resolution to detect drones at several hundred of meters may take up to a few seconds [Church *et al.* 2018]. Therefore, for high localization rates, the system must use a local scan of a reduced **FoV**, which itself should be centered on the target at all time.

Because of the risk of lowering tracking quality with heavy data processing algorithms, we choose to rely on a easier, more robust method based on a binary assumption: if an echo is produced during a local scan, then the target is present. This is particularly relevant for drones against non-signing backgrounds such as the sky. This was demonstrated for space docking rendez-vous [Blais *et al.* 2000], and more recently applied to **UAV** tracking [Kasturi *et al.* 2016].

We were inspired by these two articles and proposed the following improved solution:

Parameter	Value
Detection FoV	$\leq 10^\circ \times 10^\circ$
Scanning duration	≤ 10 s for $10^\circ \times 10^\circ$
Range	From 50 m to 1000 m
Tracking localization rate	> 100 Hz
Angular accuracy	$< 300 \mu\text{rad}$ at 1 km (size of the drone)
Range accuracy	< 1 m
Max tracked angular speed	$5^\circ/\text{s}$ (more than 40 m/s at 500 meters range)
Laser hazard	As low as possible
Dimensions & weight	Low enough to be included in another system
Modes	Detection, tracking and intrusion detection in a given angular zone

Table 4.1: Specifications of our LiDAR.

1. The first phase is target detection among a given, large FoV which is void of any targets other than the drone. The LiDAR scans this large zone, which may take a few seconds.
2. If a target is detected, then the systems switch to tracking mode with a local scanning pattern. The target is kept within the local pattern boundaries. The method relies on minimizing the error between the center of the local scanning pattern and the average of the echoes received during a period. It is akin to an ecartometry principle. Because of the narrow FoV, localization rate can be very high.
3. Concerning the intrusion detection, we chose to draw a laser cone which encloses an angular zone. If an object penetrates the zone, it crosses this laser boundary and should be detected, triggering an alarm and effectively securing the zone.

The three modes and their succession are presented in Fig. 4.1

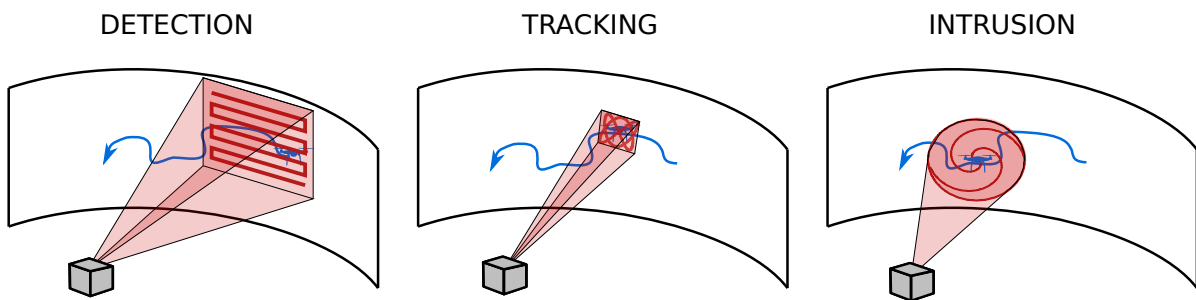


Figure 4.1: Representation of the three different modes of the system for a drone target (blue) moving at a distance from the LiDAR (grey box). To illustrate, a raster-scan is used for detection, a Lissajous is used for tracking, and a circle-spiral used for intrusion detection.

Finally, A graph showing the correspondence between target angular speed and metric speed as a function of range is shown in Fig. 4.2. On this figure we can see how widely different angular speed traduces to metric speed depending on range.

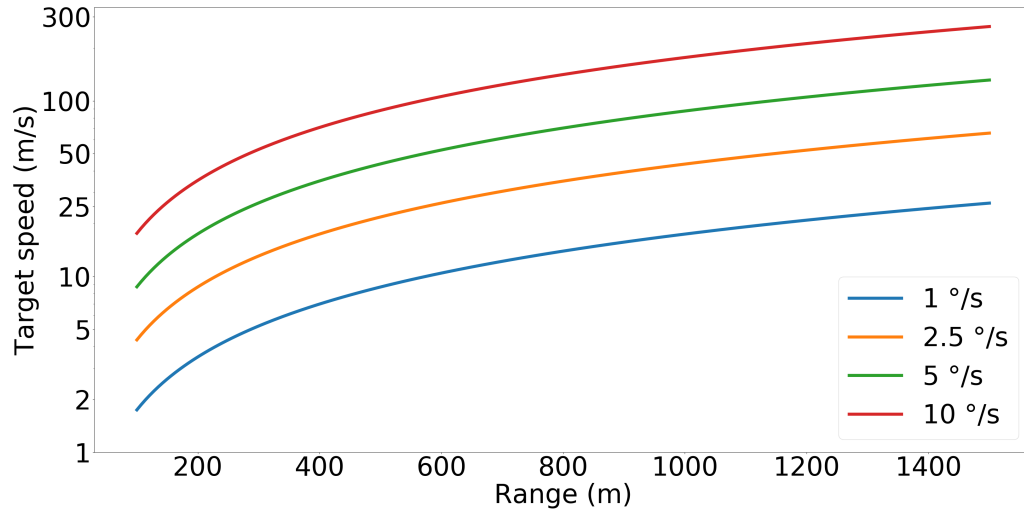


Figure 4.2: Conversion between angular and metric speed for target range from 100 meters to 1500 meters.

4.2 Coordinate system

We chose to use the horizontal coordinate system, with the two angles being azimuth θ and elevation φ . This is particularly adapted for a LiDAR aimed at flying targets because it is referenced to ground. Using Fig. 4.3, we can deduce the following transformation from our horizontal coordinate system $(\theta, \theta, \varphi)$ to the Cartesian one (x, y, z) :

$$\begin{cases} x = R \cos(\theta) \cos(\varphi) \\ y = R \sin(\theta) \cos(\varphi) \\ z = R \sin(\varphi) \end{cases} . \quad (4.1)$$

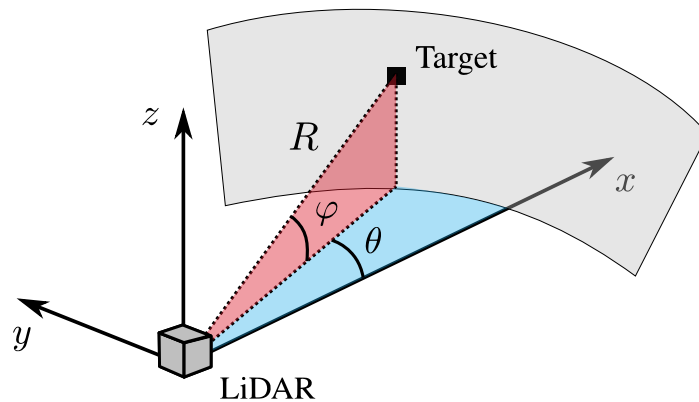


Figure 4.3: Presentation of the LiDAR horizontal coordinate system. The grey area represents a spherical portion at constant range R .

4.3 Designing an optical architecture

Scanning LiDAR is our preferred solution to answer the requirements presented. In terms of range, resolution and component availability, flash LiDAR is another good proposition, but the very narrow FoV needed (around $1^\circ \times 1^\circ$ for the range we wish to obtain [Breiter *et al.* 2018, Christnacher *et al.* 2016, Woods *et al.* 2019]) makes it incompatible with some of our requirements. One workaround would be to scan this narrow flash LiDAR FoV across the scene, but it would require mounting the system on a pan and tilt unit, which breaks the compactness requirement. On the other hand, a carefully designed scanning LiDAR can produce the necessary range, resolution, FoV and flexibility within the initial specifications.

More details on the specific components used can be found on chapter 7.

4.3.1 Configurations available

We built our LiDAR around the scanning ToF principle with a threshold pulse detection. When the emitted laser pulse intersects with an object on the scene, part of the energy is back-scattered to the system. Depending on a number of parameters such as reflectivity, energy density, atmospheric transmission and more, the back-scattered pulse may be intense enough to trigger an echo. By time-stamping the echo and reading the beam steering pointing coordinates, one has access to the azimuth θ_c , elevation φ_c and range R of the object.

Because of the required kilometer range, high peak power lasers must be used. This component is expensive and may be bulky, therefore we are limited to a single source. Multiple channels LiDAR, such as the one currently used in systems developed by the company Velodyne is thus not within our possibilities. Laser pulse width should be in the nanosecond range, combining high peak power with a relatively low pulse energy. For performance issues and ease of integration, we are also using a single element photodetector. The photodetector bandwidth and very low noise needed means an APD should be used, with an active cell as small as possible.

In terms of design, there are two main architectures. One is bi-static, where emission and reception channels are separated. The other is mono-static, where the emission and reception channels are shared. We are going to review these two.

4.3.1.1 Bi-static (scanning emission, staring reception)

In this setup, the emitted laser beam is scanned on the scene using a beam steerer. The detector stares at the whole FoV. This may be the most intuitive design, but it has two main drawbacks. At first, because of the wide FoV, noise coming from background illumination (the sun) is very high, even if it could be mitigated by using a narrow optical bandpass filter.

Another critical aspect is the aperture. Let D_r be the collection diameter (aperture), and f_o the focal of the system. If we consider an input beam of collimated light, then the f-number $n_f = f_o / D_r$ conditions the maximal value of the cone angle that can be focalised by the optical system. On the other hand, the relationship between FoV_i , D_{APD} and the lens focal f_o is given by geometric optics:

$$\text{FoV}_i = \frac{D_{\text{APD}}}{f_o} . \quad (4.2)$$

Therefore, we can express the collection diameter as

$$D_r = D_{\text{APD}} \frac{1}{n_f \text{FoV}_i} . \quad (4.3)$$

Very high aperture lens have f-number close to one ($n_f \sim 1.4$). Current technical limitations make it difficult and expensive to get f-number smaller than 1. Therefore, for a $75 \mu\text{m}$ APD and a $\text{FoV}_i=10^\circ$, the corresponding aperture is smaller than 1 mm. This is far too small for the wanted kilometer range. Therefore, this option is not realistic.

Some systems have successfully employed bi-static approach for a scanning LiDAR. They rely for instance on a single scanner for emission and reception in an autosynchronous design, but this requires a massively sized second axis [Laurin *et al.* 1999], incompatible with our speed constraints. Another solution is to use two scanning devices [ROYO *et al.* 2018], but alignments and synchronization can become very tedious for the precision we need at a kilometer range.

4.3.1.2 Mono-static (single scanner for emission and reception)

The other option is to scan a much smaller detector instantaneous FoV across the scene in synchronization with the laser. One way to readily synchronize emission and reception is to share the same scanner for both. The drawback is that collection diameter is directly limited by the scanner aperture. A bigger collection would imply a bigger scanner, and therefore less dynamic capabilities.

The complexity of mono-static systems resides in the separation between the emission and the reception. This separation can be physical, by using a holed mirror for instance, or optical, using polarization with a beamsplitter (BS). A high degree of optical isolation is critical between each channel so as not to blind or damage the detector with the emitted pulse, whose peak power can be very high. Unfortunately, each optical component introduce a new interface, which can potentially create unwanted backscattering.

A schematic of mono-static and bi-static architectures is presented in Fig. 4.4.

4.3.2 Iterations and final architecture

Our final design is comprised of a mono-static configuration with a single laser source, beam steering element and photodetector (cf Fig. 4.5). A dual axis galvanometer, which has position feedback implemented, is used as the steering element and allows for a wide range of scanning patterns. A bandpass spectral filter is added in front of the photodetector to reduce shot noise coming from background light. The beam rays should have a low enough angle of incidence to preserve the optical bandpass filter characteristics (high f-number needed).

The pulsed laser source is defined by its mean power P_{mean} , its peak power P_e , its pulse repetition frequency (PRF) f_l and its pulse width τ_p . In linear regime, we got the equation

$$P_e = \frac{P_{\text{mean}}}{\tau_p f_l} . \quad (4.4)$$

This pulsed operation means that every pattern drawn by the system is not continuous, but rather sampled at the laser PRF f_l .

In the first iteration, separation between emission was done with a BS. The source was unpolarized, and so was the BS. As a result, both the transmission coefficients in emission and reception, η_e^{BS} and η_r^{BS} , are roughly to 0.5. The total losses in the path amount to 75% of

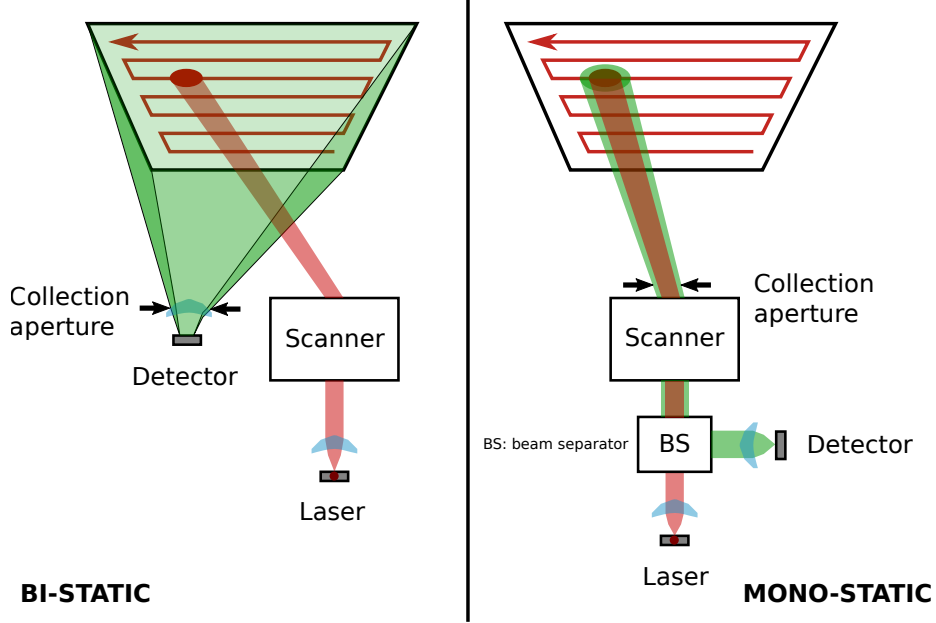


Figure 4.4: Schematic of two main types of architectures for a single emitter LiDAR scanner. (Left) Bi-static configuration with a scanning emission and a staring single photodetector. (Right) Mono-static configuration using the same scanner for both emission and reception. The critical component is the beam separator.

the total energy, which is very high. Using a polarized source and BS was considered to reduce losses. Many LiDAR architectures use polarization to this effect, with some optimization to reduce cross-talk [Wang *et al.* 2016, Qu *et al.* 2018]. Nevertheless, it can be challenging because of the depolarization effects previously mentioned in chapter 2.

In the second iteration, separation between the emitted and received pulse is done with a holed off-axis parabolic mirror (PM). The emitted laser beam goes through a hole in the mirror and is then oriented in the scene by the galvanometer. The back-scattered wave retraces the same trajectory, except it is reflected by the PM and focused onto the detector. As a result, the received aperture is annular. This induces some losses in the reception path, but creates a good optical isolation between the paths while minimizing the number of optical surfaces.

The transmission coefficients in emission and reception, η_e^{PM} and η_r^{PM} , can be expressed in this case as

$$\begin{cases} \eta_e^{PM} = 1 - \exp\left(-\frac{2D_h^2}{W_0^2}\right) \\ \eta_r^{PM} = 1 - \frac{D_h^2}{D_r^2} \end{cases}, \quad (4.5)$$

with W_0 the laser beam waist diameter assuming a Gaussian beam and D_h the mirror hole diameter.

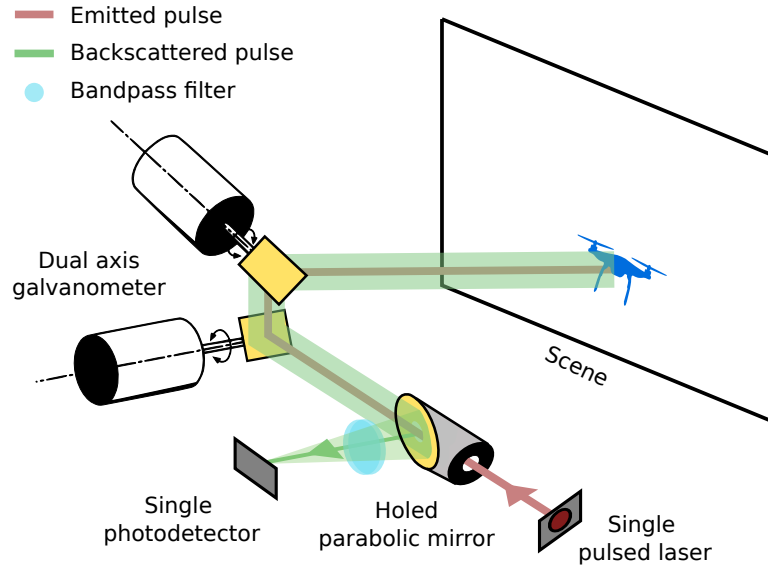


Figure 4.5: Presentation of the LiDAR final optical architecture.

4.3.3 Wavelength selection

Now that the LiDAR architecture has been described, we have to select the operating wavelength of our LiDAR. This issue in itself is quite complex, because there are a lot of parameters involved depending the application. We show on Table 4.2 the main contributing ones as well as the wavelengths we can choose from.

Parameters	Wavelengths
<ul style="list-style-type: none"> - source at the desired peak power and PRF - photo-detector performance - optics and coating availability - component prices - atmospheric transmission - background illumination (solar or terrestrial) - eye-safety limits 	<ul style="list-style-type: none"> - ultraviolet, 10 nm - 400 nm (UV) - visible wavelength, 400 - 750 nm (VIS) - near infrared, 750 - 1400 nm (NIR) - short-wavelength infrared, 1400 - 3000 nm (SWIR) - mid-wavelength infrared, 3000 - 8000 nm (MWIR) - long-wavelength infrared, 8000 - 15000 nm (LWIR)

Table 4.2: Main contributing parameters for wavelength selection.

The UV, MWIR and LWIR are fairly "exotic" and require specific, costly material, with often less performance than more widespread components. The VIS wavelength is also not suited for a scanning LiDAR application because of its visibility to the human eye (glare, temporary blindness, etc...). Therefore, we are only left with either the NIR or the short SWIR (up to 1800 nm). As mentioned on chapter 2, the APD can be based on either Si or InGaAs crystal. Their fabrication process, properties and prices are different with an advantage given to the silicon,

but not too significant. In our case, reflectivity is not a deciding factor because drones can be constituted of a wide range of materials, some with a higher signature in the NIR, others in the SWIR.

The selection can be made by looking at the laser safety issue. International laser safety standard EN 60825-1:2014 defines a maximal permitted exposure (MPE) of the eye in $[J/m^2]$ or $[W/m^2]$ for each wavelength and observation time. We plotted in Fig. 4.6 the MPE of the eye from 750 to 1800 nm, for pulses ranging from 1 ns to 1 μs and for average emission (> 10 s) and for laser divergence lower than 1.5 mrad (narrow beams). The continuous emission can be applied to pulsed sources, by considering pulse accumulation for more than 10 s.

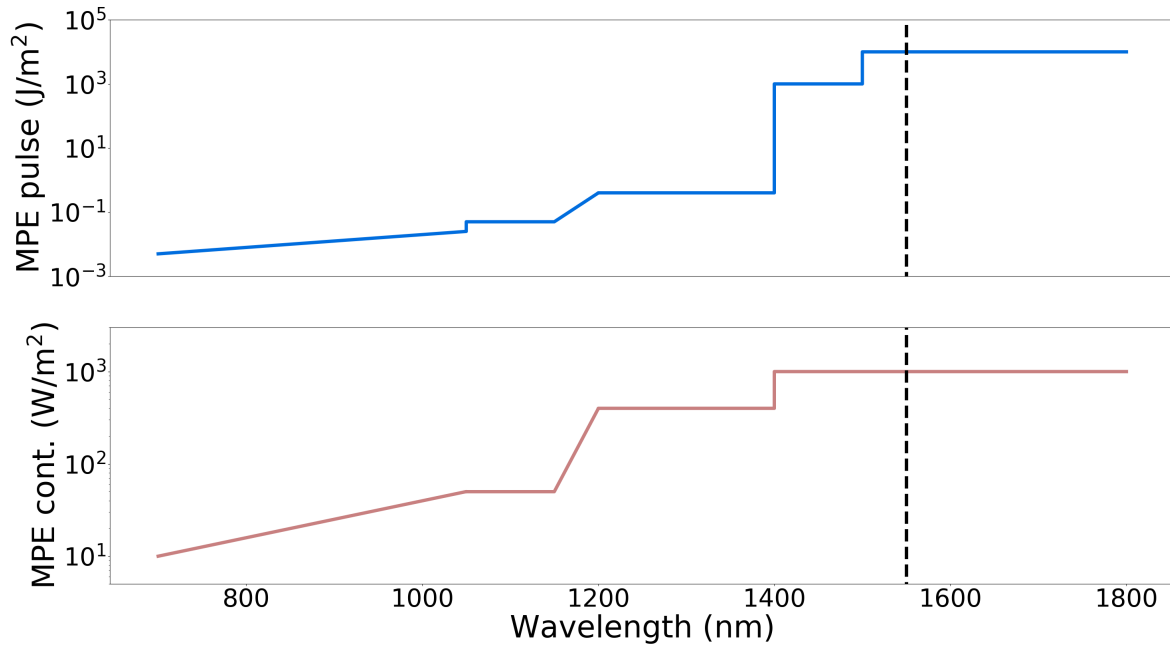


Figure 4.6: MPE of the eye for single pulse (1 ns - 1 μs) and continuous emission (> 10 s). Both ordinate scales are very different as one deals with average power, and the other with energy per pulse. The selected wavelength is 1550 nm (black dotted line), in the most permissive region.

We can see on this figure that the most permissive region for laser exposure is between 1500 and 1800 nm. In this region, radiations do not reach the retina and are stopped by the cornea and other parts. This implies that the same MPE is used for the skin at this wavelength. Due to the high repetition rate of most scanning LiDAR, the most restricting MPE is often the continuous one. Values higher than the MPE can cause thermal damage such as burns. In our application, we selected 1550 nm because of the availability of Erbium laser sources, developed for fiber communication.

4.4 Modes

4.4.1 Detection mode

In detection mode, the LiDAR scan a relatively wide FoV (for instance $10^\circ \times 10^\circ$). The most common scanning operation is a raster-scan. It is a non-overlapping directional sequential scan in two dimensions. The pattern can be achieved by driving the azimuth axis, θ , with a triangular waveform and the elevation axis, φ , with a stair waveform. By this description, θ must be driven at a much higher frequency than φ , which incidentally is adapted to dual-axis galvanometer scanner which possesses a fast and a slow axis.

To study this pattern and its performance, we need to take a closer look at its structure. Even though the raster-scan is continuously drawn, each laser pulse is separated on the θ and φ axis. The separation on θ depends on the laser PRF and the triangular waveform frequency. The separation on φ depends on the stair step size. These separations are the corresponding resolution δ_θ and δ_φ . With a Gaussian beam of given full angle divergence Θ_b , there may be significant overlap between each pulse.

The arrangement between each azimuth sweep must also be defined. For maximal density, it is possible to arrange the successive laser beams in an uniform hexagonal lattice, which is known to present the highest density when stacking disks [Fukshansky 2009]. To use this pattern and arrangement in practice, timing and synchronization between the beam scanner and the laser must be handled with care to keep drift to a minimum. This level of control is very difficult to achieve in practice. Therefore, we choose to base further studies on the worst case, which is when the pulses are kept on top of each other. The pattern then forms a rectangular (or square) lattice, which possesses the lowest compactness of any type of stack.

In this raster-scan, the critical parameters are the scanning time, T_{scan} , and the angle resolution, δ_θ and δ_φ . A perfect scanner would have both a high resolution and a short scanning time. With Fig. 4.7, we can show these quantities by introducing the triangular waveform frequency f_θ . Using the desired FoV (A_θ, A_φ), both resolutions can then be expressed as

$$\begin{cases} \delta_\theta = \frac{2f_\theta}{f_l} A_\theta \\ \delta_\varphi = \frac{1}{2T_{\text{scan}}f_\theta} A_\varphi \end{cases} . \quad (4.6)$$

These equations can be used to verify that the desired performance of the raster-scan is within the dynamic capabilities of the scanner, particularly for the azimuth axis (fast axis) frequency f_θ . We can reformulate Eq. (4.6) to express the scanning time directly as the function of the resolution, the FoV and the laser PRF as

$$T_{\text{scan}} = \frac{A_\theta A_\varphi}{\delta_\theta \delta_\varphi} \frac{1}{f_l} . \quad (4.7)$$

This equation will be used in chapter 6 as a link between the laser characteristics (f_l), the operational constraint ($T_{\text{scan}}, A_\theta, A_\varphi$), and the needed system resolution ($\delta_\theta, \delta_\varphi$).

This mode end when a detection occurs. The detection mode is binary and therefore not robust to other elements on the scene. It can be improved by range gating so as to exclude background or foreground.

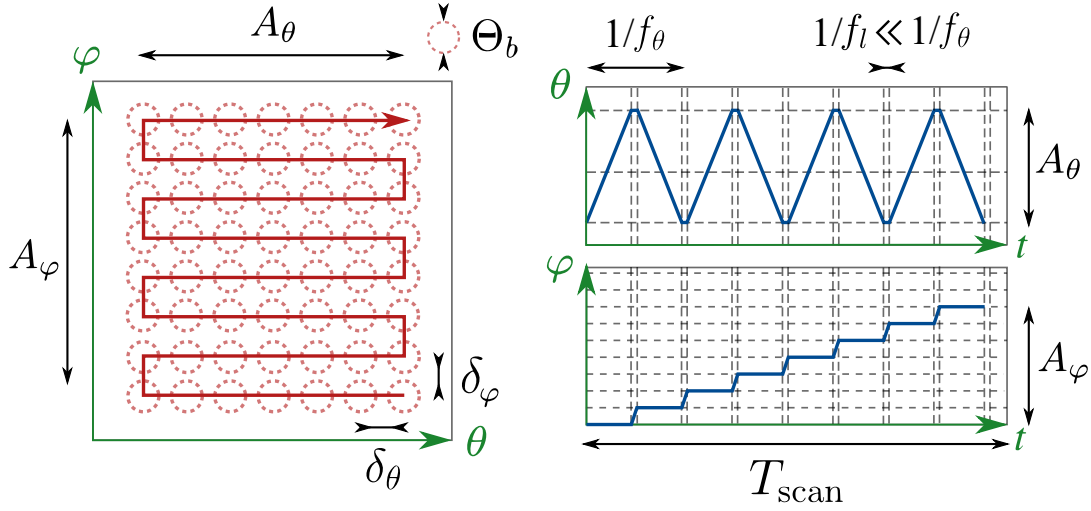


Figure 4.7: Representation of the scanning pattern (left) and each corresponding one-dimensional waveform (right). On the left the laser pulse beam distribution is highlighted in red dashed circles, Θ_b being the beam diameter projected on the scene. The laser beams distribution follows a square (or rectangular) pattern, which is a worst case with the lowest compacity.

4.4.2 Tracking mode

In a general manner, tracking consists in gaining access to the target coordinates in real-time, or more precisely at a given refresh rate. As described previously, because we wish to have a very high refresh-rate, we adapted a method found on [Blais *et al.* 2000] and [Kasturi *et al.* 2016]. The core principle is to periodically re-center a laser pattern on the target position found at the end of the current iteration, so as to minimize the error between the previous pattern center and the newly detected target position. To keep refresh rate as high as possible while complying with the bandwidth of the scanners, we have to use relatively simple and angularly small patterns. In fact, the pattern may be only a few times as big as the target. Therefore, a relatively precise primo-detection is needed to initialize tracking by localizing the target within a scene which may be tens of degrees wide. This primo-detection can be provided by other systems, or by the same LiDAR such as previously described.

The pattern shape was selected according to the target estimated diameter, D_c , to improve tracking quality. D_c can be a prior if the target dimensions are known, or can be found and refined during tracking, as described in [Blais *et al.* 2000]. The tracking algorithm is as follow:

1. at the iteration i , the laser system draws a local pattern surrounding the target, centered on coordinates $(\theta_p^i, \varphi_p^i)$. During the pattern period T_p , the beam may overlap with the target multiple times, potentially producing echos. These three dimensional echo coordinates are stored.
2. At the end of the period, the average $(\tilde{\theta}_c, \tilde{\varphi}_c, R)$ of the echoes coordinates is computed. This produces an estimation of the target coordinates.
3. The pattern center is updated using $(\theta_p^{i+1} = \tilde{\theta}_c, \varphi_p^{i+1} = \tilde{\varphi}_c)$. Then, go back to 1.

With this algorithm, if there are echoes at each period, the localization frequency f_{loc} is the inverse of the pattern period, $f_{loc}=1/T_p$. If no detection is made during a set number of periods, then tracking is considered lost (timeout). A visual description is made in Fig. 4.8. Thank to the recursivity of the algorithm, a dynamic range gating can be implemented to remove any potential foreground or background echoes.

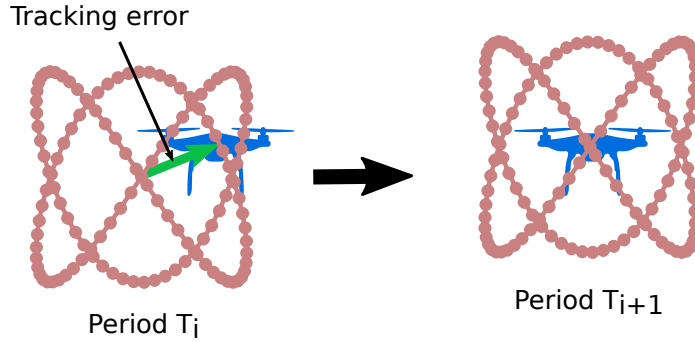


Figure 4.8: Core tracking strategy relying on minizing the tracking error between each pattern period. Pattern shape adaptation is not displayed here.

The main drawback of our strategy is that the LiDAR is entirely focused on the target and therefore blind toward the rest of the environment. Multi-target tracking can be enabled by temporally switching between targets, with a degradation of performance.

For single target tracking, performance is fundamentally linked to some parameters such as the number and homogeneity of laser beams within the pattern, the diameter of the pattern, and its period. A small target may slip within the "holes" of the grid-like pattern, and a fast target may escape the pattern boundaries before it has time to complete its revolution. Adequate pattern configuration is then critical to meet the required performance. Therefore, we propose in chapter 6 an approach to rank patterns regarding their performances in terms of probability of intersecting the target.

4.4.3 Intrusion mode

One interesting aspect of our LiDAR is its detection capabilities. In our specifications, a large angular zone around the target must be secured. Based on a previous patent [Haag *et al.* 2019], the LiDAR system is used to secure a zone by drawing an angular cone around the target. In this mode, there is another object, called the intruder, which wishes to penetrate the angular zone close to the target. The securisation cone is there to detect it when it crosses the barrier. As detailed previously, the pulsed nature of the source creates "holes" in the angular cone. To guarantee a detection, one need to play on the frequency of rotation f_i and the laser PRF. These design considerations are at the heart of this mode performances.

In parallel to the intrusion detection, the target still needs to be tracked. This is done by another system, but this one need a telemetry on the target at a given rate. To answer this requirement, a spiral is spliced within the cone at a low frequency (1 Hz). Separation between target detection and intruder detection is done by splitting the pattern into two angular zones using a coefficient s , which can take values between 0 and 1. If A_s is the circle or cone angular

diameter, then

$$\begin{cases} \text{If detection at coordinates } (\theta, \varphi) \text{ such as } \sqrt{\theta^2 + \varphi^2} \geq sA_s/2, \text{ then it is an intruder,} \\ \text{else detection is assigned to the target.} \end{cases} \quad (4.8)$$

This description is only valid if the center position of the cone is regularly updated by the other system realizing tracking. A description of the waveform used is shown in Fig. 4.9.

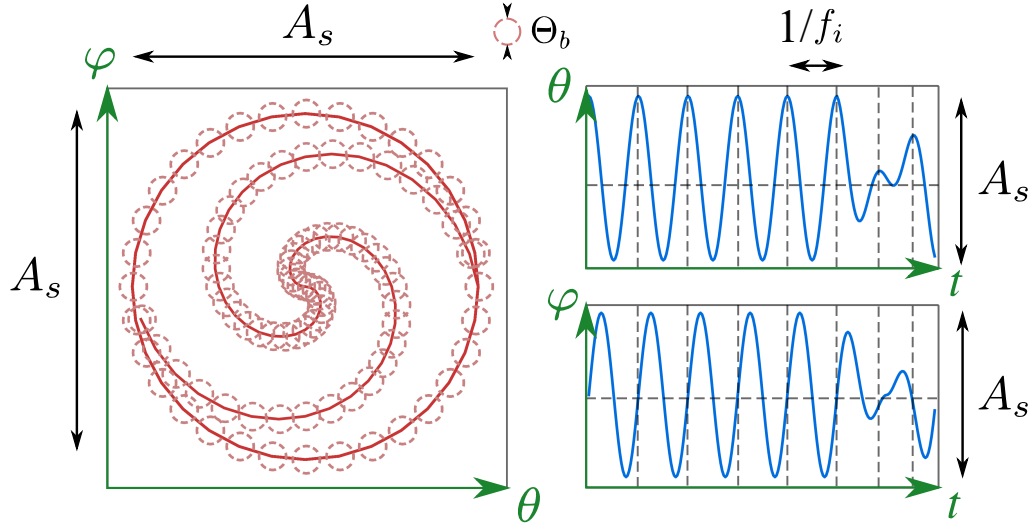


Figure 4.9: Representation of the pattern (left) and each corresponding one-dimensional waveform (right). On the left the laser pulse beam distribution is highlighted in red dashed circles, Θ_b being the beam diameter projected on the scene. The beam distribution is an angular cone with a spiral spliced at a given number of cone iterations (5 here).

4.5 Conclusion

The three modes implemented in our LiDAR are summarized in Fig. 4.1. Beside implementation, our work consisted in modeling and optimizing each individual modes regarding the needed specifications. To summarize, the theoretical work presented in the following chapters covers:

1. for detection mode, an optimization of the probability of detection of a given target at a given distance while minimizing operational constraints such as the scanning duration,
2. for tracking mode, a model for best pattern selection regarding echo density and overall performance,
3. for intrusion mode, a model to find the adequate cone frequency to always detect target of given speed and size at a given distance. This is critical for an intrusion-proof setup.

Experimental confirmation was also performed, essentially for tracking in which we gathered the most data. In any case, these models provide a global comprehensive study and a performance

analysis to indicate trends and working points. All these models take root in our extended link budget, which is described in the following chapter.

Static Model

Contents

5.1	3D Accuracy, precision and resolution	35
5.1.1	Beam width and lateral resolution	35
5.1.2	Pulse width and range precision	36
5.2	Extended link budget	37
5.2.1	Generic expression	37
5.2.2	Particular case of a lambertian target	40
5.3	Detection chain	41
5.3.1	Detector structure and binary hypothesis	41
5.3.2	Noise sources	42
5.3.3	False alarm rate	45
5.3.4	Probability of detection	48
5.4	Conclusion	50

5.1 3D Accuracy, precision and resolution

This section covers the generic optical concepts regarding static accuracy performance of a scanning LiDAR using pulsed ToF.

5.1.1 Beam width and lateral resolution

Any type of pulsed light can be used to achieve ranging. In practice, except for close range **AMCW LiDAR** (a few meters), laser sources rather than LED are employed. Spatial coherence of lasers allows to keep a high energy density across range, which is not possible for incoherent sources such as LED. Beamforming is a possibility to project a specific laser shape on the scene, especially in flash **LiDAR** where the illuminated **FoV** should be rectangular and uniform. Nevertheless, the fundamental Gaussian mode happens to be the solution of the paraxial wave equation that minimizes far-field divergence, as well as minimize spot size when focused [Paschotta 2006]. Because energy density is such a concern for long range **LiDAR**, using a laser with a diffraction limited Gaussian profile is therefore the best option. The power density I of the beam in the direction of propagation x , normalized to the emitted peak laser power P_e , is given in the **LiDAR** coordinate system (cf Fig. 4.3) by:

$$I(y, z, x) = P_e \frac{8}{\pi W(x)^2} \exp\left(-\frac{8(y^2 + z^2)}{W(x)^2}\right), \quad (5.1)$$

with W the waist diameter, which is a function of range x . W is defined as twice the distance from the center of the beam where the intensity drops to $1/e^2$. The waist diameter is linked to the laser wavelength, λ , and the initial waist (at emission), W_0 , by the formula [Paschotta 2011]

$$W = W_0 \sqrt{1 + \left(\frac{4\lambda x}{\pi W_0^2} \right)^2}. \quad (5.2)$$

It is important to note that the larger the beam at emission, the smaller its divergence is. This effect is directly linked to the physics of diffraction in wave propagation, which is similar to a Fourier transform. In our architecture, the Gaussian beam passes through a hole in a parabolic mirror. This may truncate the beam, which in turns will increase the divergence. This issue was studied in [Drège *et al.* 2000], resulting in an approximated formula of the full beam divergence, Θ_b , as a function of the hole diameter, D_h , and λ as

$$\Theta_b = 0.9712 \frac{\lambda}{W_0} \left(\frac{e}{1 - \exp \left[- \left(\frac{D_h}{1.0271 W_0} \right)^2 \right]} - 1 \right)^{1/2}. \quad (5.3)$$

Laser are often provided with a parameter, noted M^2 (M-square), which is the beam quality factor. It measures the beam shape deviation from a perfect Gaussian ($M^2=1$). Their final divergence can be approximated by Eq. (5.3) multiplied by $\sqrt{M^2}$ [Nelson & Crist 2012].

The full beam divergence directly relates to the footprint of the beam on the scene. By adapting the Rayleigh criterion to laser imaging, two object can be discriminated if they are angularly separated by at least Θ_b . This is analog to saying that the produced point cloud in dimension (θ, φ) can be approximated by the convolution between the scene and a Gaussian blur of size Θ_b . The angular separation between points is given by the chosen resolution $(\delta_\theta, \delta_\varphi)$, which is defined in chapter 4 with a raster-scan example.

A beam steerer having a better resolution than Θ_b can still be usable to reduce the error between the actual target position and the one seen by the system, particularly in tracking mode as demonstrated on chapter 7. Moreover, more resolution can be profitable in laser imagery if two-dimensional deconvolution algorithms are applied to the point cloud, similarly to what is done in image processing [Luo *et al.* 2019].

5.1.2 Pulse width and range precision

Range precision in direct ToF LiDAR is a relatively complex problem. As shown on Fig. 2.3, range is found by measuring the time between pulse emission and pulse reception (which is the ToF), producing $R = c\text{ToF}/2$. Because the pulse has a given width, some processing must be applied to reduce it to a single time value. The most common time-stamping methods are based on either peak detection, matched filter detection (or correlation detection) or leading-edge pulse detection. Matched filtering or peak detection requires very high-speed digitizer (≥ 1 GSa/s) for digital signal processing, which is costly and complex to integrate for real-time applications. Leading-edge pulse detection has a simpler electric architecture with an amplifier directly feeded into a comparator for threshold detection.

The output of the comparator is a digital pulse, which is sent to a time-to-digital converter (TDC) for time-stamping. Range resolution δ_R is given by its clock rate f_{clock}

$$\delta_R = \frac{c}{2f_{\text{clock}}} . \quad (5.4)$$

Ranging measurements are subject to systematic errors, which can be corrected by calibration, and random errors, which cannot. Systematic errors lead to loss of range accuracy and random errors lead to loss of range precision.

Systemic errors with leading-edge pulse detection stems from variations in the strength of the signal, which has an impact on the instant at which the edge crosses the threshold (range-walk errors). This error can be important in detection systems with large dynamic range, resulting in massive signal strength variation on the detector. Because pulse amplitude scales with pulse width (found by leading-edge and falling-edge time-stamping), look-up tables with polynomial fitting can be implemented to mitigate this effect [Williams 2018].

Random errors are caused by pulse-to-pulse variations in the returned pulse, therefore impacting the leading edge time-stamping. Atmospheric turbulence, noise sources in reception chain and optical SNR can generate jitter [Grönwall *et al.* 2007]. For a very simplified case of a flat diffuse target, the impact of a Gaussian noise of the detection chain produces a jitter σ_R of expression [Steinvall & Chevalier 2005]

$$\sigma_R \approx 0.1 \frac{c}{B \text{ SNR}} , \quad (5.5)$$

with B the reception chain bandwidth, which in case of a matched detector can be exchanged for the inverse of the pulse width $1/\tau_p$. As a general guide, a smaller pulse width is directly correlated with more range precision.

5.2 Extended link budget

To model the static performance of our system, we need to compute the link budget, which is the average expected number of photon received as a function of the average number of photon sent. The analytic expression is a description of the photon losses from the emission out of the laser to the atmospheric propagation toward the target and back at the detector. The key element is the beam-target interaction, which for best accuracy must take into account geometrical overlap between the two as well as the reflective properties of the target.

In our model, we suppose a target at a fixed range R to our LiDAR. We are writing our link budget in terms of peak power instead of photons (energy) so that it can be directly compared to the sensitivity of the photo-detector, often expressed in power unit.

5.2.1 Generic expression

We can separate the expression into two components. First, the emission from the output of the laser up to the target surface. The peak power P_{ts} at the target plane is given by

$$P_{ts} = P_e \eta_e T_a , \quad (5.6)$$

with P_e the emitted peak power at the laser output, η_e the emission transmission efficiency of the LiDAR and T_a the atmospheric transmission. Then, the interaction between the beam and the target is the most challenging part. The way a material scatters light is modeled using the

bi-directional reflectivity distribution function (BRDF), in steradian, noted f_{BRDF} . Strictly, this function is defined for a single point source uniformly illuminating a infinitesimal surface area with a single point source collecting a infinitesimal solid angle. Here, we are illuminating a macroscopic target, which area is given by the surface mask \mathcal{T} , with a beam of a given beam profile \mathcal{B} ($\iint \mathcal{B}(u,v) du dv = 1$). We can write the produced integral in the local (u,v) plane, which is a projection of the (y,z) LiDAR plane at target distance $x=R$. We define the beam center coordinates in this plane from its angular coordinates (θ_b, φ_b) as

$$\begin{cases} u_b = R \tan \theta_b \\ v_b = R \tan \varphi_b \end{cases}, \quad (5.7)$$

and similarly the target center coordinates in this plane from its angular coordinates (θ_c, φ_c) as

$$\begin{cases} u_c = R \tan \theta_c \\ v_c = R \tan \varphi_c \end{cases}. \quad (5.8)$$

A representation of these parameter in case of a Gaussian beam is done on Fig. 5.1.

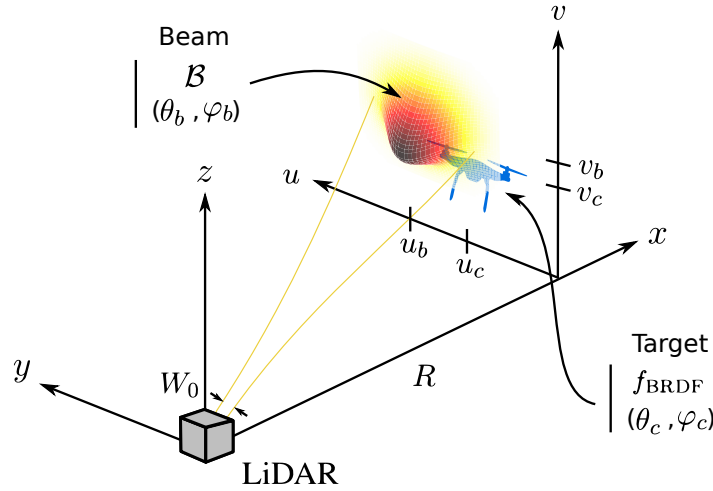


Figure 5.1: Representation of a Gaussian beam emitted by the LiDAR at coordinates (θ_b, φ_b) with a target present at coordinates (θ_c, φ_c) . We show here the local coordinate system in the target plane (u,v) as well as the interaction between the beam profile \mathcal{B} and the target profile \mathcal{T} .

f_{BRDF} is the local BRDF of the target, and can take different values across the surface, which is a function of (u, v) . Its value is also dependent on both the incident angle (θ_b, φ_b) and the photodetector angular direction (θ, φ) . We wish to have a macroscopic target BRDF function F_{BRDF} which takes into account the illumination on the target and all the local BRDF f_{BRDF} composing the target. We can thus define this function by using a surface integral of expression

$$F_{\text{BRDF}}(\theta_b, \varphi_b, \theta_c, \varphi_c, \theta, \varphi) = \iint_{-\infty}^{+\infty} \mathcal{B}(u - R \tan \theta_b, v - R \tan \varphi_b) f_{\text{BRDF}}(u - R \tan \theta_c, v - R \tan \varphi_c; \theta_b, \varphi_b, \theta, \varphi) du dv. \quad (5.9)$$

The target mask and orientation \mathcal{T} is included within f_{BRDF} . It should be noted that if the beam is a 2D Dirac function centered on (θ_b, φ_b) , then the macroscopic BRDF is equal to the microscopic BRDF of this position.

With this development, we now have an expression of the proportion of light scattered back at a infinitesimal solid angle in the direction (θ, φ) . The infinitesimal solid angle is defined by $d^2O = \sin(\theta)d\theta d\varphi$. We have to perform a final integration to get the target reflectivity into the LiDAR aperture of diameter D_r , noted \mathcal{R}_{D_r} . This integral also have to take into account the incident projection angle of the irradiance, which is traduced by a $\cos(\theta)$:

$$\mathcal{R}_{D_r}(\theta_b, \varphi_b, \theta_c, \varphi_c) = \iint F_{\text{BRDF}}(\theta_b, \varphi_b, \theta_c, \varphi_c, \theta, \varphi) \cos(\theta) d^2O . \quad (5.10)$$

The solid angle of this aperture is defined by a cone of aperture $\arctan(D_r/(2R))$ as seen by the target. Therefore, we have the following integral:

$$\mathcal{R}_{D_r}(\theta_b, \varphi_b, \theta_c, \varphi_c) = \int_0^{2\pi \arctan(\frac{D_r}{2R})} \int_0^{\arctan(\frac{D_r}{2R})} F_{\text{BRDF}}(\theta_b, \varphi_b, \theta_c, \varphi_c, \theta, \varphi) \cos(\theta) \sin(\theta) d\theta d\varphi . \quad (5.11)$$

This expression is only strictly true if the reflected direction is oriented on the normal of the target surface, which is what we suppose here. The final expression for the reflectivity depends on both the beam and target angular coordinates. This dependence can be found in the geometrical surface overlap between the two, as well as in the angle of incidence and reflection in the BRDF. Much more parameters are hidden into this function, like range or beam divergence. This description of the reflectivity can be found in a different formalism in [Jenn 2005].

If we come back to our link budget, we can write that the received power P_r on the detector is then

$$P_r = P_{ts} \mathcal{R}_{D_r} T_a \eta_r . \quad (5.12)$$

The reflectivity \mathcal{R}_{D_r} is akin to a gain factor, depending on the target incline to back-scatter energy into the solid angle defined by the collection aperture D_r . Using Eq. (5.6), the global link budget can then be written as

$$P_r = P_e \eta_e \eta_r \mathcal{R}_{D_r} T_a^2 . \quad (5.13)$$

A representation of the back-scattered energy is done on Fig. 5.2.

Atmospheric transmission is lowered by both light absorption and diffusion. Both components can be expressed using Beer-Lambert law under the expression:

$$T_a = \exp \left(- \int_0^R \kappa(l) dl \right) , \quad (5.14)$$

with κ the extinction coefficient in km^{-1} . In case of an uniform medium during propagation, we simply have $T_a = \exp(-\kappa R)$. The value of the coefficient can be found in data tables for different wavelengths and atmospheric conditions (visibility, humidity, etc...).

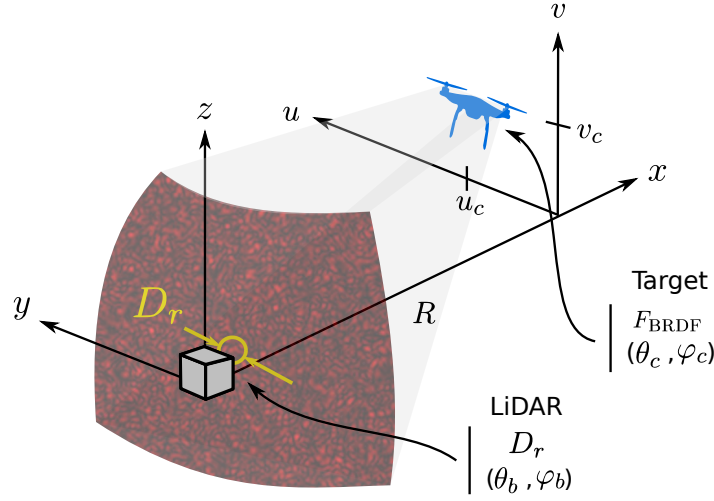


Figure 5.2: Representation of the back-scattered energy by the target surface, here shown as a speckle profile. We only show a portion of the back-scattered hemisphere. The **LiDAR** collects a fraction of light through its aperture D_r , the sensor being oriented in direction (θ_b, φ_b) (monostatic architecture).

5.2.2 Particular case of a lambertian target

We wish to simplify the expression found in Eq. (5.13) for an uniform lambertian target. Lambertian surfaces uniformly scatters back the energy into an hemisphere. They are defined by $f_{\text{BRDF}} = \rho_0 \mathcal{T}(u, v)$, with ρ_0 the constant **BRDF**, uniform in all direction. With this expression, the target surface mask on the microscopic **BRDF** formula becomes explicit. With that in mind, the macroscopic target **BRDF** function F_{BRDF} becomes:

$$\begin{aligned} F_{\text{BRDF}}(\theta_b, \varphi_b, \theta_c, \varphi_c) &= \rho_0 \int_{-\infty}^{+\infty} \int_{-\infty}^{+\infty} \mathcal{B}(u - R(\tan \theta_b - \tan \theta_c), v - R(\tan \varphi_b - \tan \varphi_c)) \mathcal{T}(u, v) \, du dv \\ &= \rho_0 \mathcal{G}(\theta_b - \theta_c, \varphi_b - \varphi_c) \end{aligned} \quad (5.15)$$

Here we have introduced \mathcal{G} , which we call the surface overlap function. This function is parametrized by the beam and target profile, and by the angular depointing between the beam and the target center position, provided that the angle difference is small:

$$\mathcal{G}(\theta_b - \theta_c, \varphi_b - \varphi_c) \sim \int_{-\infty}^{+\infty} \int_{-\infty}^{+\infty} \mathcal{B}(u - R(\theta_b - \theta_c), v - R(\varphi_b - \varphi_c)) \mathcal{T}(u, v) \, du dv . \quad (5.16)$$

We can then simplify write Eq. (5.11) as:

$$\mathcal{R}_{D_r}(\theta_b, \varphi_b, \theta_c, \varphi_c) = 2\pi\rho_0\mathcal{G}(\theta_b - \theta_c, \varphi_b - \varphi_c) \int_0^{\arctan(\frac{D_r}{2R})} \cos(\theta)\sin(\theta) \, d\theta . \quad (5.17)$$

We can recognize that $\sin(2\theta) = 2\cos(\theta)\sin(\theta)$, leading to

$$\mathcal{R}_{D_r}(\theta_b, \varphi_b, \theta_c, \varphi_c) = 2\pi\rho_0\mathcal{G}(\theta_b - \theta_c, \varphi_b - \varphi_c) \int_0^{\arctan(\frac{D_r}{2R})} \frac{\sin(2\theta)}{2} d\theta . \quad (5.18)$$

And therefore

$$\mathcal{R}_{D_r}(\theta_b, \varphi_b, \theta_c, \varphi_c) = \pi\rho_0\mathcal{G}(\theta_b - \theta_c, \varphi_b - \varphi_c) \left(\frac{1 - \cos(2 \arctan(\frac{D_r}{2R}))}{2} \right) . \quad (5.19)$$

Because the target distance is so much larger than the aperture, we have $R \gg D_r$, and $\arctan(D_r/(2R)) \sim D_r/(2R)$ (the aperture is reduced to a flat disk rather than a portion of sphere). And then, we can use the limited development of the function cosinus, $((1 - \cos(D_r/R))/2) \sim (D_r/(2R))^2$ to finally get

$$\mathcal{R}_{D_r}(\theta_b, \varphi_b, \theta_c, \varphi_c) \sim \pi\rho_0\mathcal{G}(\theta_b - \theta_c, \varphi_b - \varphi_c) \left(\frac{D_r}{2R} \right)^2 . \quad (5.20)$$

Instead of using the lambertian BRDF, it is more convenient to use the hemispheric reflectivity $\mathcal{R}_\pi = \pi \rho_0$, which can be measured with relative ease. For an uniform lambertian target, at normal incidence, we can thus expect the following returned power (using Eq. (5.13), (5.14) and (5.11)):

$$P_r = P_e \eta_e \eta_r \mathcal{G}(\theta_b - \theta_c, \varphi_b - \varphi_c) \mathcal{R}_\pi \left(\frac{D_r}{2R} \right)^2 \exp(-2\kappa R) , \quad (5.21)$$

with \mathcal{G} the surface overlap coefficient between the beam profile and the target at range R .

5.3 Detection chain

In this section we describe the model for the detection chain of our system. At first we are looking at the different noise sources which can impact the detector, and then we are interested in more operational constraints such as the false alarm rate (FAR) and the probability of pulse detection. We are doing this analysis for an APD detector in linear mode, as it provides better sensitivity compared to p-i-n photodiode. APD have the advantage of an avalanche gain G , which boost the photon signal, over p-i-n photodiodes. As we will see, this gain does not come without drawbacks, especially regarding the FAR.

5.3.1 Detector structure and binary hypothesis

The structure of the detector is important to understand how it performs and how it behaves. The detector is comprised of four main parts. An APD, which is light sensitive and converts a set of photons to electrons with a given avalanche gain. A transimpedance amplifier (TIA), which converts and amplifies the current into a given voltage. A voltage threshold comparator, which acts as a leading edge detector and output a digital "0 or 1" high level voltage. At last, a TDC time-stamp the digital voltage, provide range resolution. Detection is only acknowledged if the output of the TIA goes above a threshold. Because the output of the TIA presents random

temporal fluctuations (noise), the threshold may be crossed in the absence of signal, producing a false alarm.

For simplification purposes, we are going to use optical power in Watt instead of electrical voltage in Volt, which is only a matter of conversion factor. Let P_n be the output of the TIA (in optical Watt) without laser signal. It is a random variable of zero mean (low-pass filtered) and standard deviation σ_n , distributed along a function \mathcal{D}_n ($P_n \sim \mathcal{D}_n(\mu = 0, \sigma = \sigma_n)$, with \sim meaning "distributed along"). A false alarm occurs when P_n gets above a threshold, which we set as k times the standard deviation of the noise σ_n . We thus have the following proposition:

$$\text{in the absence of signal, a false alarm occurs IFF at an instant } t, P_n \geq k\sigma_n . \quad (5.22)$$

Now let P_s be the output of the TIA during a laser pulse return. P_s is also a random variable, whose average P_r can be calculated by the link budget shown in the previous section. It could be tempting to say that P_s is distributed along \mathcal{D}_n , meaning that the noise is purely additive and P_s deterministic. But this may not be the case, as signal carries its own fluctuations (pulse to pulse laser fluctuation, atmospheric turbulence, target speckle, shot noise, etc...). We therefore introduce the signal distribution \mathcal{D}_s , of mean P_r and standard deviation σ_s ($P_s \sim \mathcal{D}_s(\mu = P_r, \sigma = \sigma_s)$). We can then have the following proposition:

$$\text{in the presence of signal, a detection occurs IFF at an instant } t, P_s \geq k\sigma_n . \quad (5.23)$$

Finally, we can introduce the SNR as the ratio between the signal average value P_r and the standard deviation of the noise σ_n . We choose to use σ_n instead of σ_s to have a fixed noise floor.

$$\text{SNR} = \frac{P_r}{\sigma_n} . \quad (5.24)$$

Both P_r and σ_n are in optical power (Watt). To optimize the probability of detection while minimizing the FAR, we must understand the different noise sources. Measuring and modeling both \mathcal{D}_n and \mathcal{D}_s as well as their standard deviation is also essential to be able to predict performance in different scenario. The detector structure is schematized in Fig. 5.3.

5.3.2 Noise sources

In this section we are only looking at the sources of noise without signal, therefore relating to the FAR. Signal fluctuation (signal noise) will be described in the section dedicated to the probability of detection. The noise theory for APD made from Si (VIS-NIR) or InGaAs (NIR-SWIR) crystals can be found in more details in [Huntington 2016]. The sources are the following

- Thermal noise. This type of noise is present in every electronic system and comes from thermal agitation of the signal carrier in the medium. In APD, it mainly comes from the TIA which convert and amplify the low electron current into measurable voltage. Its standard deviation σ_{th} is proportional to the Boltzmann constant, the bandwidth of the receiver B , the temperature and the amplifier impedance.

- Primary dark current shot noise, or leakage current. Leakage current is due to the random generation and recombination of electrons and holes within the depletion region of the APD. There are two types of leakage, one on the bulk, which goes through the same amplification process, and one of the surface, which does not. Because the surface current is negligible in practice, the primary dark current mean value I_{pd} can be assimilated to the bulk current. The standard deviation σ_{pd} can be written as

$$\sigma_{pd} = \frac{\sqrt{2qI_{pd}G^2FB}}{\mathcal{R}_0G} \text{ [W]}, \quad (5.25)$$

with q the electron charge, G the avalanche gain, F the excess noise factor and \mathcal{R}_0 the unity-gain responsivity [A/W]. The excess noise factor F is a compensation for the tendency of APD to generate an excess of noise compared to what is expected from the dark current and amplification alone. The dark current follows a Poisson distribution, akin to shot noise. It is usually the main contributor of APD noise.

It is interesting to note that the gain G can be simplified from this equation. This is due to our definition of the SNR in Eq. (5.24), as we compare the raw returned signal against an equivalent noise power. In other words, the primary dark current and the returned power follows the same amplification, and therefore the gain do not impact the noise value in that regard.

- Background shot noise. The background comes from the exposition of the APD, during LiDAR operation, to other light sources than the laser, such as the sun. If the average value, or its slow fluctuations, can be easily filtered, there is still shot noise created. This type of noise results from the discrete time of arrival of photons, which produces a high speed fluctuation of background power, proportional to its mean value P_{bg} . The standard deviation σ_{bg} is given by

$$\sigma_{bg} = \frac{\sqrt{2q\mathcal{R}_0P_{bg}G^2FB}}{\mathcal{R}_0G} \text{ [W]}, \quad (5.26)$$

P_{bg} can be drastically reduced by using a narrow optical band-pass filter of width $\Delta\lambda$. We can write the filter width as a function of the background light noise, P_{bg} , using the equation adapted from [Richmond & Cain 2010b] as

$$P_{bg} = L_F \frac{\pi}{4} D_r^2 \text{FoV}_i^2 \Delta\lambda, \quad (5.27)$$

where L_F is the background radiance and FoV_i the photodetector instantaneous FoV. Ideally, the filter width should be chosen narrow enough so that the background noise is negligible compared to the other sources.

The detection chain and noise sources are described in Fig. 5.3. The noise of the detection chain can be reduced to the global noise standard deviation σ_n . If the background noise is negligible compared to the other sources of noise, then this value can be found under the term noise equivalent power (NEP) on most photodetector datasheets as a single, readily usable

performance metric. σ_n is the square root of the quadratic sum of every standard deviation, producing

$$\sigma_n = \frac{\sqrt{2qM^2F(I_{pd} + \mathcal{R}_0P_b)B + \sigma_{th}^2}}{\mathcal{R}_0G} \quad [\text{W}]. \quad (5.28)$$

In most cases, if the band-pass filter is narrow enough and the TIA chosen so that its noise is negligible, the primary dark current is the main contributor. The final noise standard deviation can then be reduced to

$$\sigma_n = \frac{\sqrt{2qFI_{pd}B}}{\mathcal{R}_0} \quad [\text{W}]. \quad (5.29)$$

As previously mentioned, the avalanche gain G only improves the noise figure if the amplifier noise dominates, which usually is not the case for an APD. Bandwidth selection is also critical here to minimize noise while being large enough to detect short, nanosecond pulses. Excess noise factor and primary dark current are related to the fabrication process of the APD.

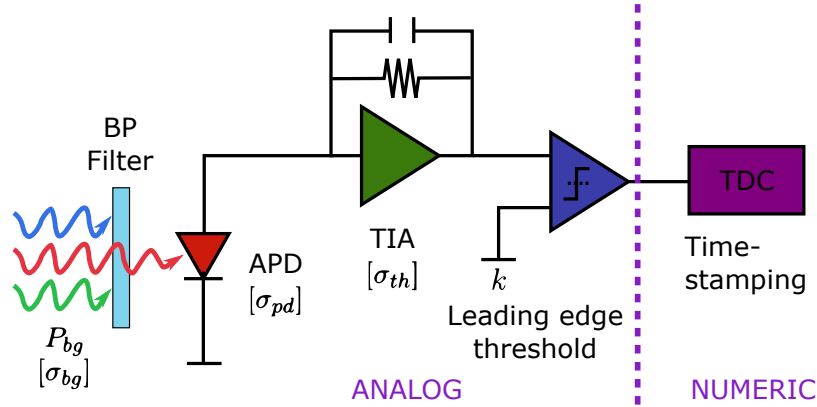


Figure 5.3: Schematic of the reception chain comprising of an optical band-pass filter (BP), an APD, a TIA, a comparator for threshold detection and the TDC for time-stamping. The noise sources, without signal, are highlighted for each component.

It is possible to measure σ_n , which is equivalent to the NEP (the detector sensitivity at a SNR=1). To achieve this, we can use a large, perfectly lambertian target of calibrated hemispherical reflectivity. The expression of σ_n as a function of range R can be found from Eq. (4.4) and (5.21):

$$\sigma_n = \frac{P_{\text{mean}}}{\text{SNR}} \frac{1}{\tau_p f_l} \frac{D_r^2}{4R^2} \mathcal{R}_\pi \eta_r. \quad (5.30)$$

Here we drop the atmospheric attenuation assuming a close range target, and $\mathcal{G} = 1$ because the target is supposed to be big enough to cover the totality of the laser beam. η_e can also be equated to 1 as the mean laser power can be directly measured outside of the system. The numerical application is disclosed on chapter 7.

5.3.3 False alarm rate

5.3.3.1 Analytic development

In this subsection, no laser signal is present. We want to model the distribution of the noise \mathcal{D}_n , of standard deviation σ_n . Contrary to the probability of false alarm, the FAR has a temporal component, which is directly proportional to the TDC clock rate f_{clock} for time-stamping. Indeed, if the probability of having a false alarm is equal to one, then a detection will occur at every clock cycle of the TDC, meaning that $\text{FAR} = f_{\text{clock}}$ in this case. We can then give a general expression of the FAR as

$$\text{FAR}(k) = f_{\text{clock}} \int_{k\sigma_n}^{+\infty} \mathcal{D}_n(x|\mu=0, \sigma=\sigma_n) dx, \quad (5.31)$$

where μ is the mean value of the noise distribution, σ its standard deviation. The FAR is a function of the threshold factor k . The noise distribution is critical to get an accurate value of the FAR at a given threshold, but is often overlooked. For instance, with a classic Gaussian assumption, we have

$$\begin{aligned} \text{FAR}_{\text{gauss}}(k) &= f_{\text{clock}} \int_{k\sigma_n}^{+\infty} \frac{1}{\sigma_n \sqrt{2\pi}} \exp\left(-\frac{x^2}{2\sigma_n^2}\right) dx \\ &= \frac{f_{\text{clock}}}{2} \left(1 - \text{erf}\left(\frac{k}{\sqrt{2}}\right)\right) \end{aligned} \quad (5.32)$$

One distinctive characteristics of APD is that the secondary carriers that are generated from the primary carriers (from dark current, background and laser photo-current) follow a MacIntyre noise distribution. For these photodetectors, the avalanche process induces an excess of noise, meaning that unwanted events of large magnitude happens more frequently. This leads to a tail in the distribution function, which means that for high gain values, important false alarm rates can be observed at thresholds where it should be negligible compared to the Gaussian assumption [Huntington *et al.* 2018]. The resulting \mathcal{D}_n is the convolution of a Poisson distribution (primary carriers are Poisson distributed) with a MacIntyre distribution (secondary carriers). Unfortunately, there is no closed-form for this distribution, and is complex to compute due to multiple infinite series.

5.3.3.2 Experimental confirmation

Rather than making further assumptions on theoretical models, we performed a direct FAR measurement of our detection chain (cf Fig. 5.3). We fed the output of the threshold comparator to a counter of sampling frequency f_{count} , and swept the value of k across a full range. In practice, we don't have direct access to k , but we rather had to sweep a gain on the amplifier before the comparator input of the integrated APD. A voltage gain and offset is done on this input, and therefore we need a way to transform k_{mV} into the actual value k .

Moreover, we observed on our APD a cross-talk effect between the analog and the digital output. Each time the comparator is triggered, it emits a 1 V digital pulse which artificially increases the value of the analog output pulse. When plotting the histogram of the maxima of

this analog output we can then observed a bimodal distribution (cf Fig. 5.4). The distribution of lower amplitude is populated by the maxima of the noise that did not triggered the comparator, and the distribution of higher amplitude is populated by the maxima of the noise that triggered the comparator and created a false alarm.

The intersection of both distributions is the best way to separate the noise that triggered a false alarm from the noise that did not trigger it. Thus, this value was accepted as the threshold. k can be deduced by dividing this value by the standard deviation of the analog noise (measured when the trigger is set very high so no cross-talk can happen). We obtained a linear fit of expression

$$k = \frac{k_{mV} - 476}{4} \quad (5.33)$$

The data we had to gather to find this expression is illustrated in Fig. 5.4.

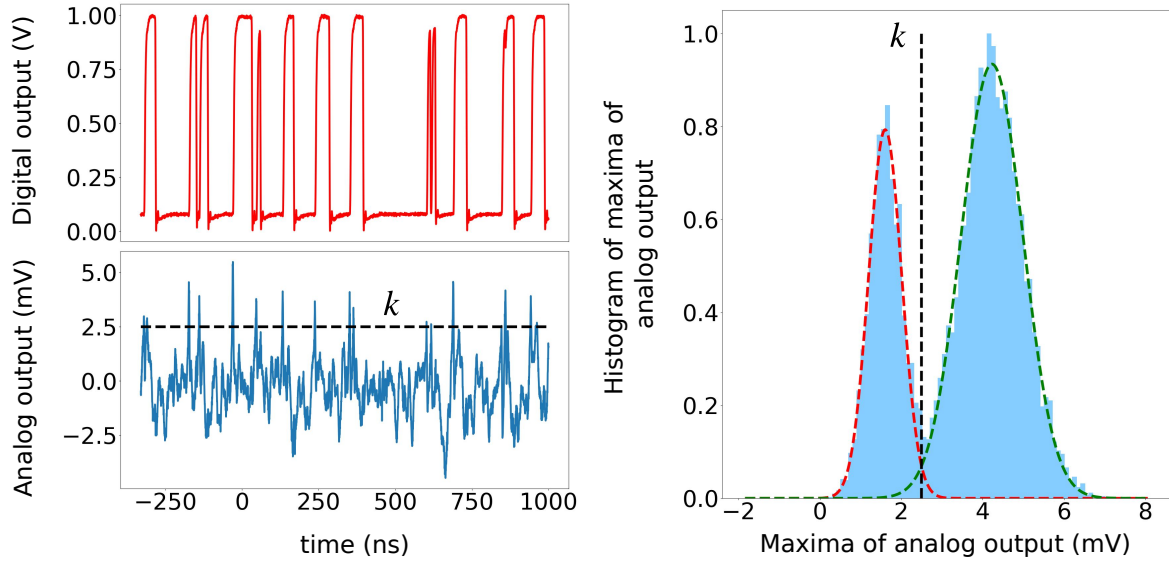


Figure 5.4: (Up left) digital output of the comparator, (down left) analog output of the comparator, (right) histogram of the maxima of the analog output, and Gaussian fit of the bimodal distribution (red and green dots). The bimodal histogram reveals a cross-talk between the analog and the digital output, effectively dividing the noise maxima between the values triggering and not triggering the comparator.

Then, we can measure the FAR as a function of k_{mV} , translated into k by using Eq. (5.33), with a counter sampling frequency of $f_{\text{count}}=200$ MHz. This measurement was made with the APD mounted on the architecture described in Fig. 4.5, pointed toward an outdoor wall during a sunny day of summer. A 12 nm width optical filter was used to keep noise contribution from the solar background minimal. This setup was purposely done so that the FAR could be more representative of real operating conditions. The APD model used is an InGaAs, with a 75 μm diameter, operated at a high gain ($G \sim 20$). The results are presented in Fig. 5.5.

The first observation we can make is that the FAR is at half value for $k=2.7$. In theory, because the analog noise average is null, it should be at half value for $k=0$. By analyzing the

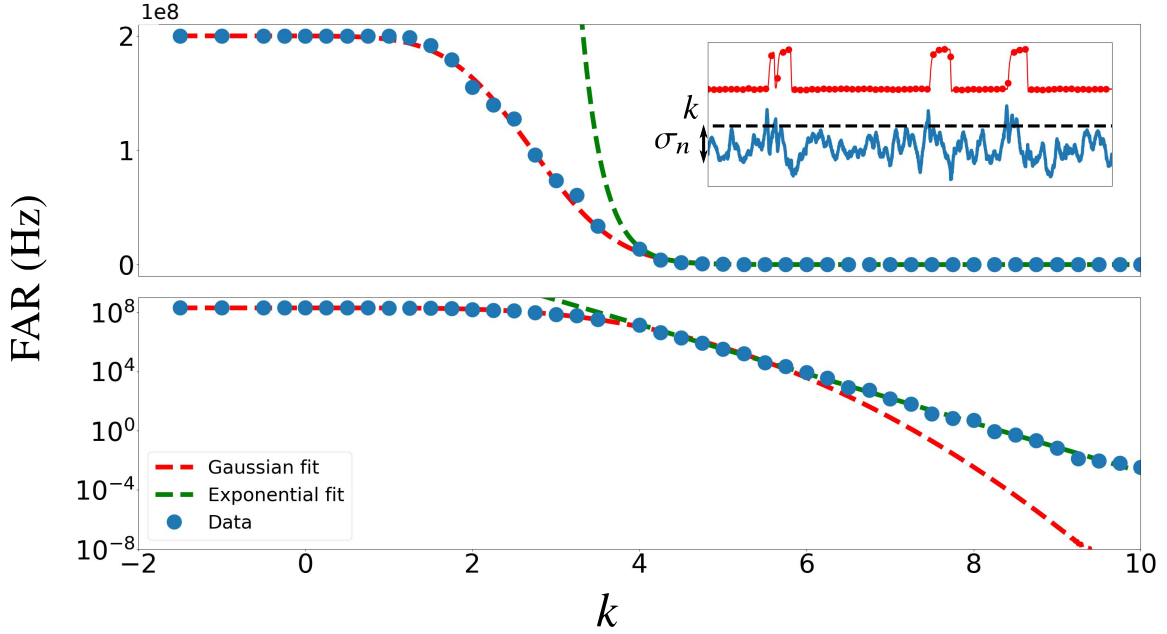


Figure 5.5: Linear and logarithmic plot of the FAR as a function of the threshold k (blue dots), with a Gaussian cumulative distribution fit (red line) and an exponential fit (green line). (Insert) Analog noise from the APD (blue) and comparator output (red). The spacing between dots represents the counter sampling frequency f_{count} .

behavior of the digital output compared to the analog output, we observed that the comparator behavior was not strictly a "sample by sample" comparison. For low values of k , there seems to be a hysteresis component, as the digital output does not immediately goes back to low level if the analog value crosses back the threshold. This effect, which can be seen in Fig. 5.4 (top left), is believed to produce a higher FAR that what could be expected for relatively high values of k compared to σ_n . The Gaussian model used to fit the FAR produced

$$\text{FAR}_{\text{gauss}}(k) = \frac{f_{\text{count}}}{2} \left(1 - \text{erf} \left(\frac{k - 2.7}{\sqrt{2} \cdot 0.8} \right) \right). \quad (5.34)$$

We can observe in Fig. 5.5 that this Gaussian assumption underestimates the number of false alarms observed for high values of k . For instance, at a threshold $k=9$, we can observe 1 false alarm every 15 seconds, whereas the Gaussian assumption prediction is completely negligible. This behavior has been extensively studied since the assembly of the first APD, and the noise is known to follow the MacIntyre distribution [Huntington *et al.* 2018]. Here, because we want to provide a simple way to fit the data, we choose to fit the tail with an exponential function of expression

$$\text{FAR}_{\text{exp}}(k) = \exp(-3.82 k + 31.83), \quad (5.35)$$

valid for $k \geq 4.6$. We can now set a threshold value k producing a negligible amount of false alarm. Here we used a threshold $k=10$, resulting in about 1 false alarm every six minutes.

5.3.4 Probability of detection

5.3.4.1 Analytic development

Now we consider that a return pulse is present. We can first define the probability of detection \mathcal{P}_d as the ratio between the number of pulse emitted and the number of pulse received. Mathematically, the probability of detection is akin to the cumulative distribution function of the signal random variable P_s . Therefore, we can write \mathcal{P}_d as

$$\mathcal{P}_d(k, P_r) = \int_{k\sigma_n}^{+\infty} \mathcal{D}_s(x|\mu = P_r, \sigma = \sigma_s) dx, \quad (5.36)$$

where μ is the mean value of the signal distribution, σ its standard deviation. \mathcal{P}_d is a function of the threshold factor k and the mean return signal P_r . For a classic Gaussian assumption, we have

$$\begin{aligned} \mathcal{P}_d(k, \text{SNR}) &= \int_{k\sigma_n}^{+\infty} \frac{1}{\sigma_s \sqrt{2\pi}} \exp\left(-\frac{(x - P_r)^2}{2\sigma_s^2}\right) dx \\ &= \frac{1}{2} \left(1 - \text{erf}\left(\frac{k - \text{SNR}}{\sqrt{2}\sigma_s/\sigma_n}\right)\right) \end{aligned} \quad (5.37)$$

In this equation we have replaced P_r by the SNR using Eq. (5.24). The signal fluctuations can come from multiple sources. The laser stability pulse to pulse was tested but rejected as a noise source (less than 1% peak power fluctuation). Atmospheric turbulence and speckle may create fluctuations, and have been extensively studied [Goodman 2007]. Nevertheless, the most prevalent source of noise is often the signal shot noise, which is linked to the discrete time of arrival of photons. Because the signal is added to the already existing detector noise, we can add the signal shot noise in quadrature to the standard deviation of the noise, producing:

$$\sigma_s = \sqrt{\sigma_n^2 + \frac{2qFP_rB}{\mathcal{R}_0}} \quad [\text{W}]. \quad (5.38)$$

We can then write that:

$$\sigma_s/\sigma_n = \sqrt{1 + \frac{2qFB}{\mathcal{R}_0\sigma_n} \text{SNR}}. \quad (5.39)$$

And finally:

$$\mathcal{P}_d(k, \text{SNR}) = \frac{1}{2} \left(1 - \text{erf}\left(\frac{k - \text{SNR}}{\sqrt{2(1 + a\text{SNR})}}\right)\right), \quad (5.40)$$

with $a = 2qFB/\mathcal{R}_0\sigma_n$, a being unit-less.

5.3.4.2 Experimental confirmation

Even though theoretical value for a is computable, we have to confront our model with experimental data. Especially to see if other noise sources could impact \mathcal{P}_d . Therefore, by pointing the system at a given target, we swept the laser peak power P_e and measured the probability

of detection $\mathcal{P}_d = [\text{number of pulses received}] / [\text{number of pulses sent}]$ as a function of the signal to noise ratio $\text{SNR} = P_r / \sigma_n$. P_r is measured using the analog output of the APD, and σ_n is as mentioned the standard deviation of the noise on this analog output without signal. In Fig. 5.6, \mathcal{P}_d was measured for three different static targets at different ranges. The threshold was set at $k=10$, which corresponds to a very low FAR of around one false alarm every six minutes. The plot of \mathcal{P}_d is presented in Fig. 5.6. The best fit was found for $a = 0.35$.

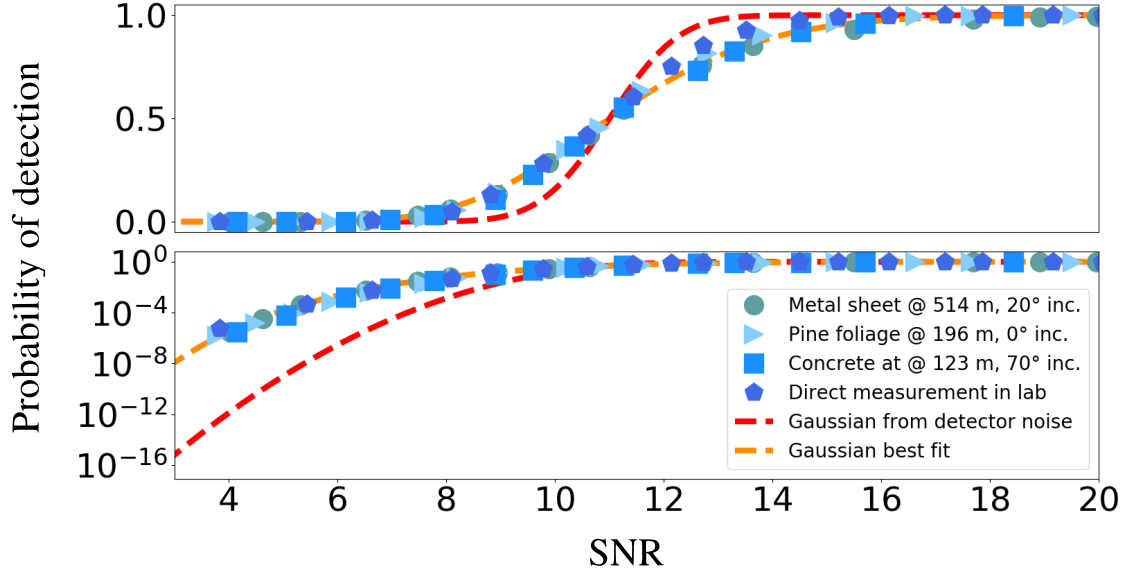


Figure 5.6: Linear and logarithmic plot of the probability of detection for three types of targets at various distances and angles of incidence, and in the laboratory with the laser directly illuminating the detector (using densities to lower the power). The orange dotted line is from Eq. (5.40), with $a = 0.35$ and the red one is from noise contribution only with $a = 0$.

Interestingly, the probability of detection seems independent on both the nature of the material and the angle of incidence. No variations were also observed if the beam divergence or the collection aperture were modified. This was confirmed by making the measurement again in a lab, using neutral densities to point the laser beam directly on the APD (pentagon dots in Fig. 5.6). This result may be surprising, as it tends to indicate that neither the atmospheric turbulence nor target speckle seem to have measurable impact on the probability of detection. Yet it must be kept in mind that these measurements are only a subset of data and may not represent the complete behavior of the system. For instance the impact of the detector gain, FAR, or laser coherence length was not tested.

Another thing that can be noted is that even if the threshold was set at $k=10$, we observe that the 50% probability of detection point is realized at $\text{SNR}=11$. This effect was consistently reproduced, and can be interpreted in the way that more power is needed to trigger an event than to trigger a false alarm. This difference could be linked to the comparator non-linearities previously highlighted, but the layout of the circuit would be needed to reach a definitive conclusion. It could also be linked to the limitation of our digital electronics. A low SNR means a smaller pulse width than a high SNR due to pulse walk effect. And a pulse width of a few

nanoseconds, with only 1 V amplitude, could indeed be challenging for many digital electronics. This effect could potentially bias the probability of detection toward larger SNR, and could also explain why it is independent of the target type.

Now in theory, we can compute a with $q=1.6 * 10^{-19}$ C, $F=5.6$, $R_0=1$ A/W, $B=17$ MHz and $\sigma_n=0.56$ nW (from the APD datasheet and measurements). We obtain as a result $a = 65$, which is two order of magnitude bigger than the experimental a . An explanation can be that the variance use comes from a Poisson distribution of the signal shot noise, rather than the MacIntyre distribution. In any case, the presence of the square root of the SNR in the denominator of Eq. (5.40), which is a good fit to the data, seems to imply a shot noise type of fluctuation.

Finally the noise and signal distributions \mathcal{D}_n and \mathcal{D}_s can be deduced from the equation of the FAR and \mathcal{P}_d respectively. We chose to put them on the same axis with a signal SNR=11. It is presented in Fig. 5.7.

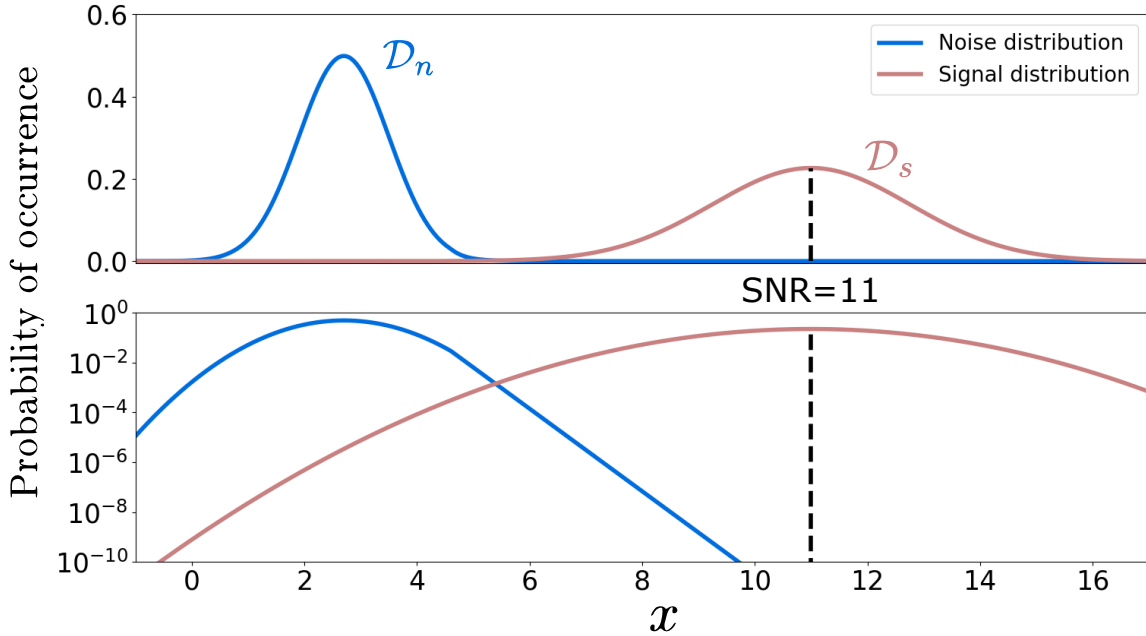


Figure 5.7: Linear and logarithmic plot of the distribution density for the noise and the signal (with SNR=11 for the signal). The transition between the Gaussian and exponential function is visible in the change of slope in the noise distribution at $x=4.6$. The distribution around the average is much wider for the signal than for the noise.

5.4 Conclusion

We now have a detailed model for the static capabilities of our system. Static inaccuracies are linked to the beam divergence and pulse width, if we except beam steerer pointing stability. Thanks to the link budget, we can have the expected average return power as function of a great number of parameters, which can be simplified or complexified depending on the application. Deep understanding and measurements on the detection chain gave us fitted models for both the FAR and the probability of detection, as well as the value of its sensitivity (NEP or σ_n).

This development was critical to accurately compute the probability to detect a given object at a given range. Transitioning to the dynamic model can be done by using the surface overlap function \mathcal{G} introduced in the link budget, which is function of the relative position of the beam compared to the target center position. This function was used in our first paper on scanning optimization [Quentel *et al.* 2019].

Dynamic Models

Contents

6.1 Scanning optimization for detection mode	53
6.1.1 Probability of multiple echoes	53
6.1.2 Model simplification using the probability to detect a single echo	58
6.1.3 Impact of the target speed	62
6.2 Circle optimization for intrusion mode	64
6.3 Pattern optimization for tracking mode	66
6.3.1 Pattern equations	66
6.3.2 Patterns ranked as a function of the probability of intersection	68
6.4 Scanning frequency limitations	73
6.4.1 Light round-trip travel	73
6.4.2 Scanner bandwidth	74
6.5 Conclusion	77

This chapter is dedicated to model the dynamic performances of the LiDAR. This development is made regarding the three LiDAR modes described on chapter 4, which are the detection, tracking and intrusion mode. To this effect, we wish to bring together the pattern parameters of each mode (angular resolution, duration, amplitude, etc...) and the probability of detection previously found. By using the probability to get one - or more - echo from the target as our main criteria, we can highlight trends and lay the foundations of a parametric study.

6.1 Scanning optimization for detection mode

6.1.1 Probability of multiple echoes

In detection mode, we are using the target coordinates (θ_c, φ_c) relative to the beam (θ_b, φ_b) to find the probability of echoes. They are linked to the probability of detection in the link budget expression (via the surface overlap function), and to the raster scan via the beam disposition on the scene. We can then introduce the angular beam-target depointing in both directions $(\Delta\theta^i, \Delta\varphi^i)$:

$$\begin{cases} \Delta\theta^i = \theta_b^i - \theta_c \\ \Delta\varphi^i = \varphi_b^i - \varphi_c \end{cases}, \quad (6.1)$$

with the subscript i being a reference for a given laser beam within the raster-scan pattern considered.

The target is supposed to be perfectly uniform, with lambertian back-scattering properties. A more accurate model can be employed, yet a low reflectivity lambertian target is usually met in literature as a generic target providing an overall performance value [Williams 2017]. This is especially useful when the target properties are not known, or if they are too diverse to be restricted to a specific reflectivity model.

For a lambertian target, the link budget can be adapter from Eq. (5.21) using the depointing as

$$P_r(\Delta\theta^i, \Delta\varphi^i) = P_e \eta_e \eta_r \mathcal{G}(\Delta\theta^i, \Delta\varphi^i) \left(\frac{D_r}{2R} \right)^2 \exp(-2\kappa R) . \quad (6.2)$$

Similarly, the SNR becomes

$$\text{SNR}(\Delta\theta^i, \Delta\varphi^i) = \frac{P_r(\Delta\theta^i, \Delta\varphi^i)}{\sigma_n} = b \mathcal{G}(\Delta\theta^i, \Delta\varphi^i) , \quad (6.3)$$

with $b = \frac{P_e}{\sigma_n} \eta_e \eta_r \left(\frac{D_r}{2R} \right)^2 \exp(-2\kappa R)$, b being unit-less. Finally, we can write the probability of pulse detection from Eq. (5.40) as

$$\mathcal{P}_d(\Delta\theta^i, \Delta\varphi^i) = \frac{1}{2} \left(1 - \text{erf} \left(\frac{k - b \mathcal{G}(\Delta\theta^i, \Delta\varphi^i)}{\sqrt{2(1 + a b \mathcal{G}(\Delta\theta^i, \Delta\varphi^i))}} \right) \right) . \quad (6.4)$$

Now as discussed previously, the pulsed laser is sequentially scanned on the scene during the raster-scan, producing a rectangular grid-like scan pattern. Each laser beam is separated in azimuth by δ_θ and in elevation by δ_φ . Because of the repetitive nature of the scan pattern, it forms a lattice. From this observation, we can reduce our study to the target positions in a single mesh element Z of size $(\delta_\theta, \delta_\varphi)$. \mathcal{P}_d is a function of the depointing $(\Delta\theta^i, \Delta\varphi^i)$ between beam and target, therefore it can be expressed for each target position (θ_c, φ_c) within Z , and for every pulses of the raster-scan grid. This implies that for a single target position within Z , there is potentially as much echoes as the number of pulses on the raster-scan (as illustrated on Fig. 6.1).

To better explicit our development, we can show an example of the probability to get a single echo from a pulse numbered i , among the total number of pulses N of the raster-scan. The pulses indexation is arbitrary, and its purpose is only for notation. For instance, we can choose to number the pulses starting from left to right, and up to down. The probability $\mathcal{P}(m = 1|i)$ to get one echo from the pulse i , among the N pulses within the raster-scan, is then

$$\mathcal{P}(m = 1|i) = \frac{\iint_{\delta_\theta, \delta_\varphi} \mathcal{P}_d(\theta_b^i - \theta_c, \varphi_b^i - \varphi_c) \prod_{j \neq i, 1}^N [1 - \mathcal{P}_d(\theta_b^j - \theta_c, \varphi_b^j - \varphi_c)] d\theta_c d\varphi_c}{\delta_\theta \delta_\varphi} . \quad (6.5)$$

This expression was put together by computing the probability to have exactly 1 echo for one given pulse, and none for the other pulses ($\mathcal{P}_d \prod (1 - \mathcal{P}_d)$), for one given target position. We then performed an integration for every target positions over the Z area, which gives a global probability to get 1 echo for a given pulse i . There is no need to integrate positions outside of Z because the raster-scan is a repeated mesh of cell Z . The global probability to get a single echo $\mathcal{P}(m = 1)$, from any of the N pulses is then simply

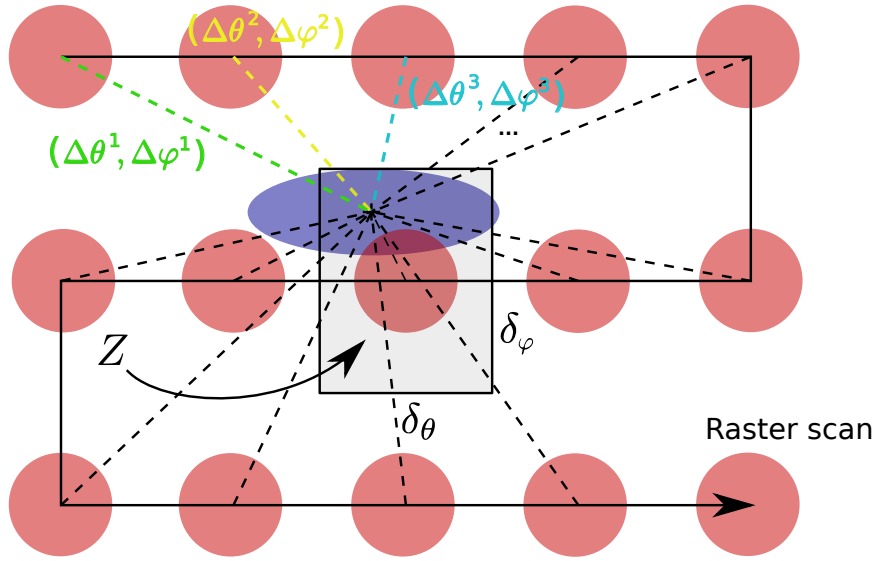


Figure 6.1: Illustration of a pulsed laser beam (red disks) raster-scan pattern with a grid parameter $(\delta_\theta, \delta_\phi)$ and an elliptic target (blue ellipse). The depointing between each laser beam and the target is given by $(\Delta\theta^i, \Delta\phi^i)$ (dotted lines).

$$\mathcal{P}(m = 1) = \sum_{i=1}^N \mathcal{P}(m = 1|i) \quad (6.6)$$

To account for 2 or more echoes, the formula has to evolve drastically. Indeed, we have to find all the combinations for the pulses i or j among the N possible pulses. The total number of combinations to take into account is classically given by $\binom{l}{N}$. To this effect, we introduce $\zeta_{l,N}$, which is the ordered combination of the probability of echoes from l pulses among N . This expression cannot be written formally, but we can give an example for 2 echoes among 4 pulses. To simplify notations, we will use $\mathcal{P}_d(j) = \mathcal{P}_d(\theta_b^j - \theta_c, \varphi_b^j - \varphi_c)$ in our example:

$$\begin{aligned} \zeta_{2,4}(1) &= \mathcal{P}_d(1)\mathcal{P}_d(2)(1 - \mathcal{P}_d(3))(1 - \mathcal{P}_d(4)) , \\ \zeta_{2,4}(2) &= \mathcal{P}_d(1)\mathcal{P}_d(3)(1 - \mathcal{P}_d(2))(1 - \mathcal{P}_d(4)) , \\ \zeta_{2,4}(3) &= \mathcal{P}_d(1)\mathcal{P}_d(4)(1 - \mathcal{P}_d(2))(1 - \mathcal{P}_d(3)) , \\ \zeta_{2,4}(4) &= \mathcal{P}_d(2)\mathcal{P}_d(3)(1 - \mathcal{P}_d(1))(1 - \mathcal{P}_d(4)) , \\ \zeta_{2,4}(5) &= \mathcal{P}_d(2)\mathcal{P}_d(4)(1 - \mathcal{P}_d(1))(1 - \mathcal{P}_d(3)) , \\ \zeta_{2,4}(6) &= \mathcal{P}_d(3)\mathcal{P}_d(4)(1 - \mathcal{P}_d(1))(1 - \mathcal{P}_d(2)) , \end{aligned} \quad (6.7)$$

There are $\binom{2}{4} = 6$ required expression of $\zeta_{2,4}$ to account for all cases. The variable i of $\zeta_{2,4}$ is randomly ordered, and is simply use to index this function. We can then generalize Eq. (6.6) and write that the probability to have l echoes among N pulses $\mathcal{P}(m = l)$ is

$$\mathcal{P}(m = l) = \frac{1}{\delta_\theta \delta_\varphi} \sum_{i=1}^{\binom{l}{N}} \iint_{\delta_\theta, \delta_\varphi} \zeta_{l,N}(i, \theta_c, \varphi_c) d\theta_c d\varphi_c . \quad (6.8)$$

The probability of having at least l echoes among N pulses $\mathcal{P}(m \geq l)$ is the sum $\mathcal{P}(m \geq l) = \sum_{j=l}^N \mathcal{P}(m = j)$. The full expression is then given by

$$\mathcal{P}(m \geq l) = \frac{1}{\delta_\theta \delta_\varphi} \sum_{j=l}^N \sum_{i=1}^{\binom{j}{N}} \iint_{\delta_\theta, \delta_\varphi} \zeta_{l,N}(i, \theta_c, \varphi_c) d\theta_c d\varphi_c . \quad (6.9)$$

It is important to highlight that this expression is not a mathematical closed-form. Each expression of $\zeta_{l,N}$ must be calculated by an iterative algorithm. The number of elements to sum and the complexity of the algorithm is, from the formula, at best $2^N - 1$. Therefore, increasing the number of echoes will increase computation time in an exponential manner.

Beside the sum of combinations, the key to the algorithm is the computation of the surface overlap function \mathcal{G} . This function is defined by Eq. (5.16) with a given beam and target profiles, \mathcal{B} and \mathcal{T} . The expression can be either formally integrated into a closed form for specific target and beam shape, or numerically integrated using 2D matrix and convolution. This is what we chose to do, by computing both the laser beam and the target in the form of a 2D matrix at a given range. The overlap function \mathcal{G} (and therefore \mathcal{P}_d) can then be numerically computed for every position of the target (θ, φ) within \mathcal{Z} , and for every of the N pulses. We choose to reduce the target to two parameters, one along the azimuth, D_θ , and one along the elevation D_φ . Its shape is in this case elliptical. The laser beam intensity is supposed to be Gaussian. An illustration is presented in Fig. 6.3.

For each range R , the algorithm is the following:

1. create a resolved enough 2D matrix for both the beam and the target (cf Fig. 6.3 and 6.2). This mesh has to be re-computed for each range because the laser beam diameter increases with range (due to its divergence),
2. for each pulse on the raster-scan, compute the overlap surface coefficient \mathcal{G} (with a numerical convolution) using each pulse position relative to the target. Repeat this operation for each target position within \mathcal{Z} (illustration in Fig. 6.1). We obtain N 2 dimensional matrix representing the value of \mathcal{G} for each target position within \mathcal{Z} ,
3. using Eq. (6.4), for each pulse, compute b , then \mathcal{P}_d from the \mathcal{G} matrix. We obtain N 2 dimensional matrix representing \mathcal{P}_d ,
4. using Eq. (6.9), compute $\mathcal{P}(m \geq l)$ from the \mathcal{P}_d matrix, by summing over the 2 dimensional matrix elements.
5. go back to 1) for another value of the range R .

Because of the number of iterations needed to explore the probability of echoes as a function of R , this method is computation heavy. Let K be the number of ranges R considered. Then, the number of operations to perform is $K2^N$. It is exponentially increasing with the number of

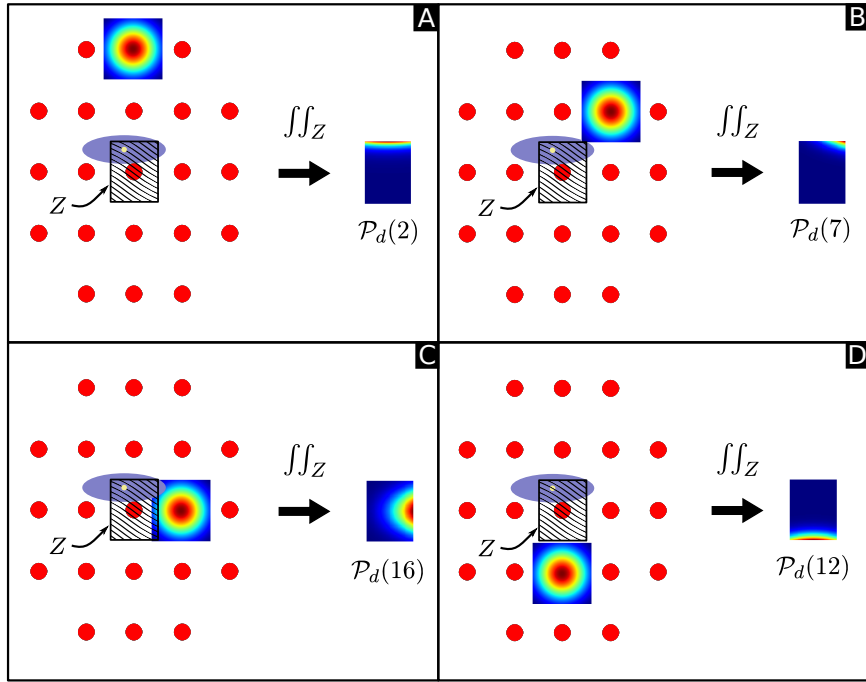


Figure 6.2: Illustration of the resulting probability of detection for 4 pulses (number 2, 7, 12 and 16) among 21, for each target position (θ, φ) within Z (wave pattern at the center). The red dots represents the centers of the beams, the blue ellipse the target, and the Gaussian image the beam. In this example, the target is too small compared to the beam waist for the outer ring of the raster-scan to produce echoes. Nevertheless, it will produce echoes at closer distance, where the target is much larger.

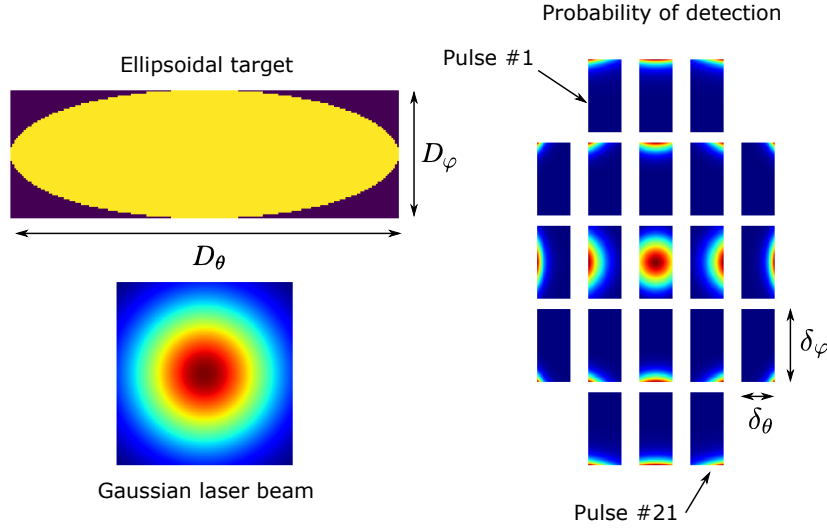


Figure 6.3: Probability of detection $\mathcal{P}_d(\Delta\theta^i, \Delta\varphi^i)$ for each target position (θ, φ) within Z , and for every one of the 21 laser pulses considered. Each element is shown at their respective pulse position, but separated by a white space for convenience (in reality they are continuous). The target is elliptical with dimensions $D_\varphi=3D_\theta$. The raster scan has a dimension $\delta_\varphi=2\delta_\theta$. Dimensions and colors are not to scale between inserts.

laser beams considered. The accuracy of the model will also increase with the number of echoes considered.

Now, we developed a forward model giving the probability to detect a given target from a given number of parameters. This means that finding an optimal parameter (laser peak power, angular resolution, divergence, etc...) requires an extensive iterative process. It is even worse when multiple parameters must be optimized from each other, without mentioning computation time. Nevertheless, it is still a very complete approach which can be used as a tool to complete other approaches.

6.1.2 Model simplification using the probability to detect a single echo

In this subsection, we wish to develop a faster model to be able to dynamically optimize some parameters of our LiDAR. To achieve this, we have to make certain simplification steps. We can list them here:

- we are only considering the probability to have a single echo. Moreover, we are only looking at a single beam i , which is the closest from the target. This assumption considerably simplifies our problem because there is no need to use combinations,
- the beam is Gaussian during its whole propagation path, meaning that atmospheric turbulence are neglected,
- the target is a disk of diameter D_c , of uniform lambertian reflectivity.

Using a disk target is important to achieve a symmetry of revolution in the overlap function \mathcal{G} . In that case, the depointing between a beam and the target is only depending on the distance r between the center of the target and the center of the beam in the target plane (in the local coordinate system (u, v)). This heavily reduce computation time.

In this subsection, we are trying to keep using the angular parameters (θ, φ) , rather than the local coordinate system at range R , ($u = R \tan \theta$, $v = R \tan \varphi$). As we are only considering a single echo, we can simplify our notations. We consider that the beam is centered in our reference frame, ($u_b = 0$, $v_b = 0$) and ($\theta_b = 0$, $\varphi_b = 0$). The target coordinates can thus be simplified ($u_c = u$, $v_c = v$) and ($\theta_c = \theta$, $\varphi_c = \varphi$). The overlap function can then be simplified:

$$\mathcal{G}(\theta_b - \theta_c, \varphi_b - \varphi_c) = \mathcal{G}(\theta, \varphi) \quad (6.10)$$

Because of this symmetry of revolution, we can restraint our study to depointing on the single axis u . The expression for the target profile \mathcal{T} becomes

$$\begin{cases} \mathcal{T}(u, v) = 1 & \text{iff } (u - r)^2 + v^2 \leq \frac{D_c^2}{4} \\ \mathcal{T}(u, v) = 0 & \text{otherwise} \end{cases} \quad (6.11)$$

with $r = \sqrt{u^2 + v^2} = R\sqrt{(\tan \theta^2 + \tan \varphi^2)} \sim R\sqrt{\theta^2 + \varphi^2}$ for small angles. The planar distance between the beam and the target center position. The beam profile is considered Gaussian. It was presented in Eq. (5.1), and we can write here in our coordinate system as:

$$\mathcal{B}(u, v) = P_e \frac{8}{\pi W^2} \exp\left(-\frac{8(u^2 + v^2)}{W^2}\right), \quad (6.12)$$

with W the waist diameter. The overlap function \mathcal{G} , introduced in Eq. (5.16), can then be expressed as

$$\mathcal{G}(\theta, \varphi) = \iint_{\left(u - R\sqrt{\theta^2 + \varphi^2}\right)^2 + v^2 \leq \frac{D_c^2}{4}} \frac{8}{\pi W^2} \exp\left(-\frac{8(u^2 + v^2)}{W^2}\right) du dv. \quad (6.13)$$

We can simplify the previous equation by using the local polar coordinate system (r, ν) for integration ($r = \sqrt{u^2 + v^2}$, $u = r \cos \nu$, $v = r \sin \nu$). The expression becomes

$$\mathcal{G}(\theta, \varphi) = \frac{8}{\pi W^2} \int_0^{2\pi} \int_0^{D_c/2} r \exp\left(-\frac{8(r^2 + R^2(\theta^2 + \varphi^2) + 2rR\sqrt{\theta^2 + \varphi^2}\cos(\nu))}{W^2}\right) dr d\nu. \quad (6.14)$$

The overlap surface coefficient is presented in Fig. 6.4.

Unfortunately the expression does not have a closed form, so it has to be numerically computed. The probability of detection as a function of the angular depointing can be written using Eq. (6.4) as

$$\mathcal{P}_d(\theta, \varphi) = \frac{1}{2} \left(1 - \operatorname{erf} \left(\frac{k - b \mathcal{G}(\theta, \varphi)}{\sqrt{2(1 + a b \mathcal{G}(\theta, \varphi))}} \right) \right). \quad (6.15)$$

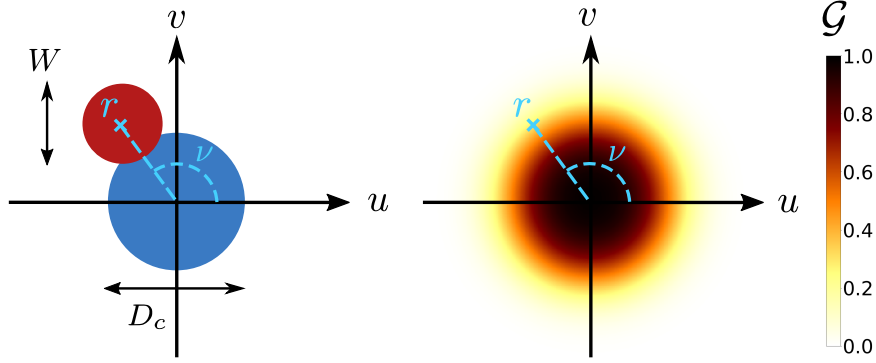


Figure 6.4: (Right) representation of the surface overlap coefficient between a Gaussian laser beam of waist diameter W and a disk target of diameter D_c . On the left is represented one position of the beam (red disk) ($u \sim R\theta$, $v \sim R\varphi$) relative to the target (blue disk), producing a single point in the 2D grid. The only variable is the planar distance $r \sim R\sqrt{\theta^2 + \varphi^2}$.

When applied to the rectangular grid-like pattern of the raster-scan, we can clearly see the layout of the lattice with the mesh element Z of size $(\delta_\theta, \delta_\varphi)$. Similarly to the previous subsection, we can reduce our study to the mesh element Z (see Fig. 6.5). The simplified probability to get 1 echo from the closest beam to the target is then the integral of \mathcal{P}_d over the area Z :

$$P(m=1) = \frac{1}{\delta_\theta \delta_\varphi} \int_{-\delta_\varphi/2}^{\delta_\varphi/2} \int_{-\delta_\theta/2}^{\delta_\theta/2} \mathcal{P}_d(\theta, \varphi) d\theta d\varphi. \quad (6.16)$$

Compared to Eq. (6.5), we have made a number of simplifications. As stated previously, we have only taken into account the beam closest to the target, which avoids heavy combinatory computations. In practice, some deviation can be observed when comparing single echo to multi-echo computations. Nevertheless, the gain in computing duration (more than 100 times faster) makes the single echo the best alternative. Comparisons between the two algorithms are shown on subsection 9.2.

With the model that we developed, we can possibly find the values of a set of chosen parameters among all (peak power, collection, scanning time, etc...) which will guarantee a probability p to get an echo. The simplifications done in this subsection should allow for relatively fast iterative implementation to quickly optimize chosen parameters using the following equation:

$$P(m=1) = \frac{1}{2\delta_\theta \delta_\varphi} \int_{-\delta_\varphi/2}^{\delta_\varphi/2} \int_{-\delta_\theta/2}^{\delta_\theta/2} \left(1 - \operatorname{erf} \left(\frac{k - b \mathcal{G}(\theta, \varphi)}{\sqrt{2(1 + a b \mathcal{G}(\theta, \varphi))}} \right) \right) d\theta d\varphi. \quad (6.17)$$

The dependency of most the variables are hidden in b , including the range R . The scanning time T_{scan} can also be a variable as it is a function of the azimuth and elevation resolution.

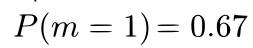


Figure 6.5: Representation of the probability of detection as a function of the beam-target depointing $r \sim \sqrt{\theta^2 + \varphi^2}$ for a raster scan. A_c is the target angular diameter. In this example the probability to get an echo is 0.67.

6.1.3 Impact of the target speed

In all the previous models, the target was supposed to be static within the scene. Under a number of assumption, we obtained the probability of detection for the mesh element Z , which was equated to the whole scene. We can use this model as our base to include the target speed, which should degrade the probability of detection.

Here, we are only considering speed in the target plane, ie orthogonal to the LiDAR line of sight, and at range R . This correspond to a "worst case" scenario, contrary to a target coming toward or going away from the LiDAR, which will appear static. In the target plane, the target speed has two components: one in azimuth, noted V_c^θ , and one in elevation, noted V_c^φ . We suppose that speed is constant in both norm and direction. Moreover, the target is supposed to move in the opposite direction of the scan to fit into this worst case.

The target position follows an uniform random distribution, which means that it can start from anywhere on the scene. To find the impact of the target speed, we have to look at the closest target position relative to a pulse, and then to the next one on either azimuth or elevation (depending on the speed orientation). Because the target has moved between these two pulses, there are occasions where the target is never contained within the rectangle $(\delta_\theta, \delta_\varphi)$ of either pulses. The time between pulses on the azimuth axis is $1/f_l$ and $1/(2f_\theta)$ on the elevation axis.

We illustrate this effect in Fig. 6.6 for a target speed $V_c = V_c^\varphi$ oriented in elevation. We can clearly see here that because of the target movement, it is never within Z for pulse 0, neither for pulse 1. The target initial position here is selected so that compared to pulse 0, the distance in elevation is $\delta_\varphi + \frac{V_c^\varphi}{4f_\theta}$ at time t_0 . At time t_1 , the target is at the same distance in elevation to pulse 1. This is the only case for which the target is at equal distance to both pulses. In other cases, the target is gonna be closer to either pulse 0 or pulse 1, which would improve the probability of detection. To account for all these target positions, we have to perform an integration over the new mesh element Z_{v_c} of dimensions

$$\begin{cases} \text{On the azimuth axis, } \delta_\theta + \frac{V_c^\theta}{f_l} \sim \delta_\theta \\ \text{On the elevation axis, } \delta_\varphi + \frac{V_c^\varphi}{2f_\theta} \end{cases} . \quad (6.18)$$

The speed oriented toward the azimuth θ can be discarded here because the laser PRF $f_l \gg f_\theta$. Then, the probability of getting an echo can be readily adapted from Eq. (6.17):

$$P(m=1) = \frac{1}{2\delta_\theta(\delta_\varphi + V_c^\varphi/(2f_\theta))} \int_{-\delta_\varphi/2 - V_c^\varphi/(4f_\theta)}^{\delta_\varphi/2 + V_c^\varphi/(4f_\theta)} \int_{-\delta_\theta/2}^{\delta_\theta/2} \left(1 - \operatorname{erf} \left(\frac{k - b \mathcal{G}(\theta, \varphi)}{\sqrt{2(1 + a b \mathcal{G}(\theta, \varphi))}} \right) \right) d\theta d\varphi . \quad (6.19)$$

This formula should be computed in the same way than on the previous subsection, ie using numerical methods.

We can give a speed limit for this expression. Let's suppose that the scanning starts in the upper corner. Because the target position is uniformly distributed on the scene, all target positions lower than $A_\varphi/2$ account for half of all positions, and all target positions upper than $A_\varphi/2$ account for the other half. This starting position can be therefore seen as an average starting position, at the right balance between the edges and the scanner initial position. Moreover, we

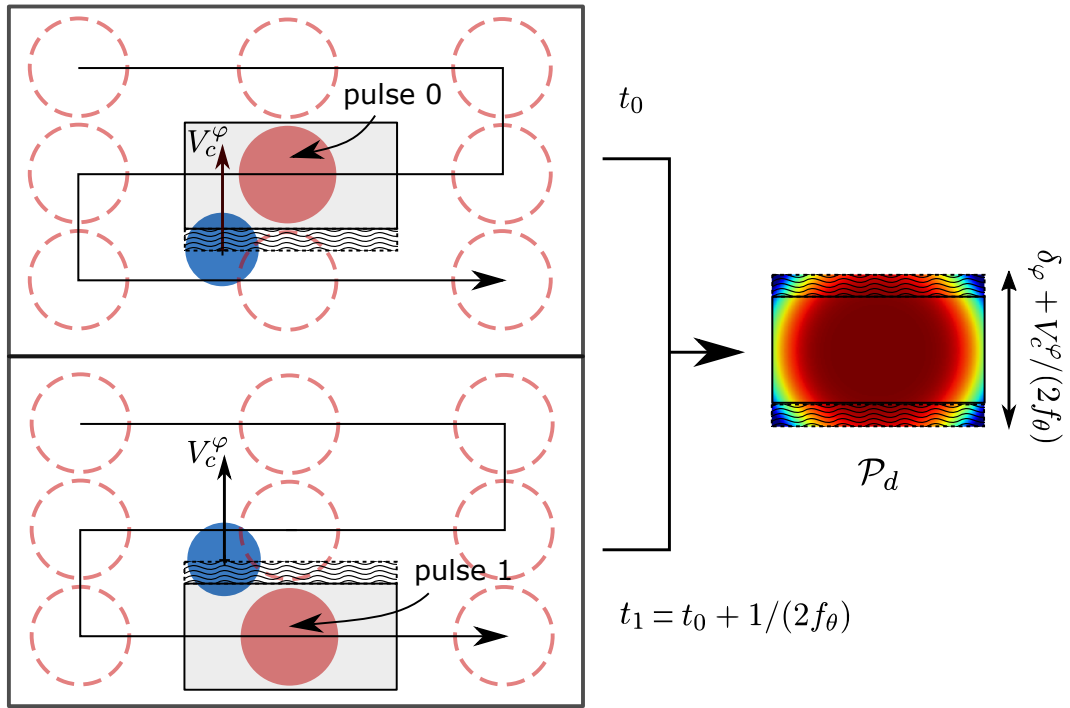


Figure 6.6: Illustration of the mesh \mathcal{Z} boundaries evolution (black rectangle and wave pattern) as a function of the target speed. Here the target speed is oriented purely in φ and in a direction opposite to the scan, which is a worse case.

suppose that both the target and the scan go to the same direction (scanning in elevation up to down and target going straight down). In this configuration, the target can only intersect with the scanner if

$$V_c \leq \frac{A_\varphi}{2T_{\text{scan}}} . \quad (6.20)$$

This expression defines the maximal speed after which it becomes unlikely to detect the target during a scan, because the target would have more than 1/2 chances to escape the scene before being reached.

Finally, all this development can be applied with reverted LiDAR axis, ie for raster-scan progressing from left to right instead of up to down. This can be used for targets evolving primarily on the azimuth axis θ , which present a much higher azimuthal speed than elevation.

6.2 Circle optimization for intrusion mode

In this section, we wish to find the relationship between the parameters of the circle (angular diameter A_s and frequency f_i) and the parameter of the intruder (diameter D_i , range R , speed V_i , etc..) with the LiDAR parameters previously seen. We can use a similar approach to what was done for the raster-scan, but with a circle. For simplicity we suppose again that the intruder is an uniform lambertian disk. Moreover, beside the circle, the pattern presents a spiral which is used to get echoes from the target at the center. In this mode of operation, the echo rate (1 Hz) is suppose to be much lower than the circle frequency (>100 Hz), meaning that the proportion of time spent by the system on the perimeter is much larger than on the center. To this effect, we are neglecting the time spent on the center and considering that the pattern is a full and complete circle at all time.

In this mode, the intruder is outside the circle and wishes to enter the inside area. Therefore, it has to cross the circle perimeter. Because of the laser PRF, the perimeter is discontinuous and composed of multiples laser beams. The probability of detection was presented on Eq. (6.4) and is a function of the depointing between the beam and the target via the surface overlap function \mathcal{G} . Because the circle repeats itself at frequency f_i , we can see it as a fixed lattice with a given mesh element. This is a similar approach to the raster scan, except the grid is not rectangular but circular, and is only comprised of the perimeter.

There are two dimensions to this mesh element, one following the circle radial direction, δ_i^r , and one following the orthogonal direction (the tangent), δ_i^o . Strictly, because of the radius of curvature of the circle, these two dimensions are bent along the perimeter curve. Here, we will make the assumption that the circle diameter A_s is much larger than the target, so that the radius of curvature is supposed infinite. This is done to fall back to rectangular mesh element, so as to simplify computations. δ_i^o can be deducted from the angular separations between pulses on the perimeter. The number of pulses on the circle perimeter are defined by f_t/f_i , and the perimeter is given by πA_s . Therefore, we have:

$$\delta_i^o = \pi A_s \frac{f_i}{f_t} \quad (6.21)$$

On the other direction, the dimension must be defined by the intruder speed. The pattern can be seen as mono-dimensional, especially if the circle radius of curvature is infinite. It becomes a

line which presents no boundary in the radial direction. Fortunately, we can use developments previously made for the raster-scan regarding target speed. Here, the intruder starting position is uniformly distributed across the scene. This means that the intruder may cross the circle at any time. Moreover, probability of detection is directly a function of the angular distance $\sqrt{\theta^2 + \varphi^2}$ between the center of a given beam and the center of the intruder.

We consider at time t_0 the closest pulse to the intruder, called pulse 0. While the scanner is drawing the circle, the intruder crosses the perimeter. At time $t_1 = t_0 + 1/f_i$ (the scanner has done a circle revolution), the intruder is at another distance to the same pulse 0, but at a later time. In the worse case, the intruder is at the same distance from the pulse at t_0 compared to t_1 , minimizing the probability of detection. This would mean that the intruder was at distance $V_i/(2f_i)$ (outside of the circle) at time t_0 , and again $V_i/(2f_i)$ (inside of the circle) at time t_1 . In any other case, the intruder would be closer at either t_0 or t_1 . Therefore this example gives us a boundary for the radial direction:

$$\delta_i^r = \frac{V_i}{f_i} \quad (6.22)$$

All these considerations are illustrated in Fig. 6.7.

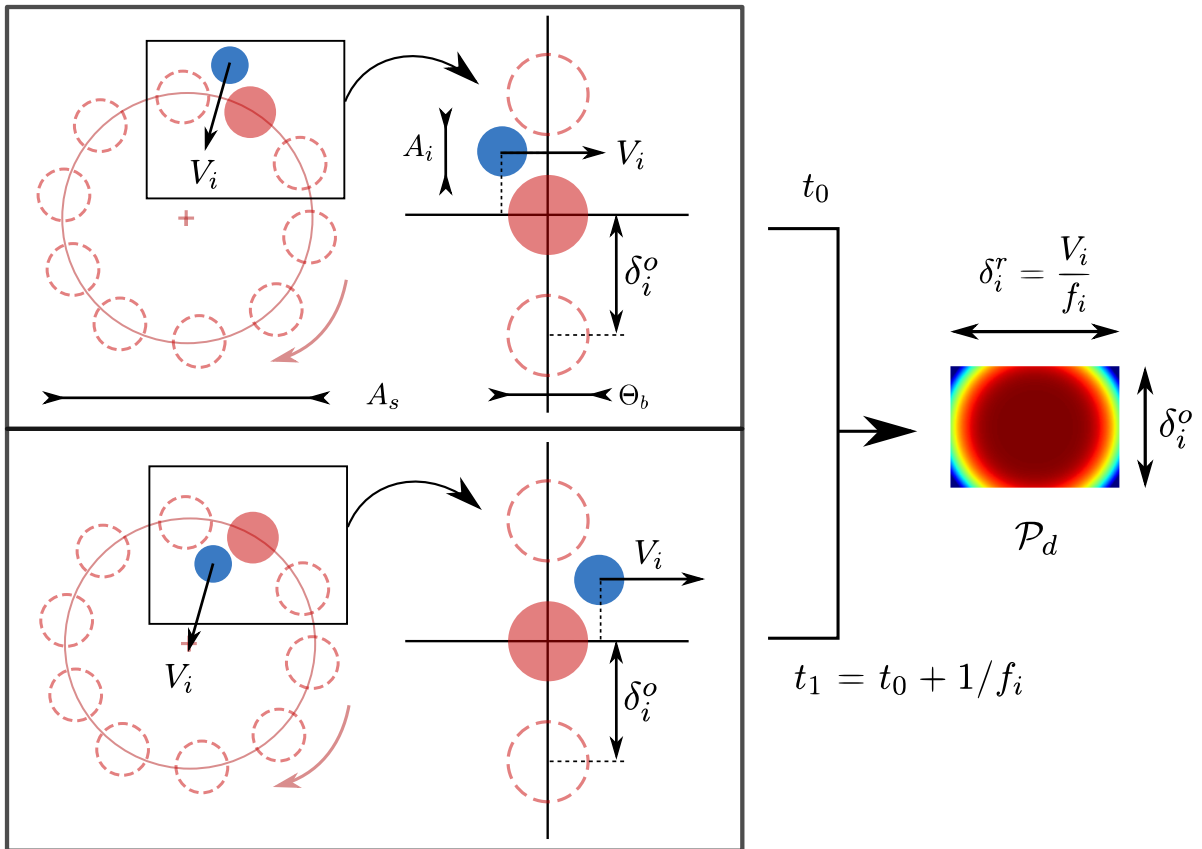


Figure 6.7: Illustration of the mesh element for the circle pattern in the case of an intruder of speed V_i , oriented in the radial direction.

Then, the probability of getting an echo can be found by integrated the probability of detec-

tion over the whole mesh element area (δ_i^o, δ_i^r) . From Eq. (6.17), we find:

$$P(N = 1) = \frac{1}{2\delta_i^r \delta_i^o} \int_{-\delta_i^o/2}^{\delta_i^o/2} \int_{-\delta_i^r/2}^{\delta_i^r/2} \left(1 - \operatorname{erf} \left(\frac{k - b \mathcal{G}(\theta, \varphi)}{\sqrt{2(1 + a b \mathcal{G}(\theta, \varphi))}} \right) \right) d\theta d\varphi. \quad (6.23)$$

This expression is the probability to get one echo on the intruder. It is possible to get the probability to gather multiple echoes from other pulses by using a combinatory formula akin to Eq. (6.9). Getting more than a single echo may provide more information of the nature of the intruder. This is especially important if the area to secure is moving, so that the circle pattern must follow along. Then, it may cross static objects such as trees or building which should be filtered. The same can be said for birds which could create false alarms. On this aspect, stronger recognition capabilities would be needed.

6.3 Pattern optimization for tracking mode

In a scanning LiDAR, sequentially scanning a scene takes a given time, noted T_p . This value correspond to the period of the pattern used during the scan. The pattern is sampled at a given rate, noted f_l , which for instance may be the laser repetition rate. Even at a constant period T_p , each pattern spreads laser beams in a different way in space (angular resolution between laser samples) and time (time it take for the beam steerer to go from one section to another).

In this section, we wish build a criteria able to rank patterns based on this resolution analysis, in both space and time. This way, a good pattern would provide a high beam density, uniformly spread across the scene. On the contrary, a less favorable one would present non-uniform beam density, leaving holes in some zones. One must keep in mind that the analysis cannot be done in two-dimension, but must include time as well to accordingly weight for a moving object or scene. This development can be applied to any kind of pattern, but for concision we will only apply it to the three different types of patterns displayed in the previous section: Lissajous, raster-scan and spirals. We believe that they provide a wide enough coverage for our analysis.

6.3.1 Pattern equations

Any beam steering device possesses a finite bandwidth, which is usually function of the pattern angular amplitude A_p (see chapter 7). The pattern is drawn at a certain speed, and therefore has frequency components of various amplitude, which must fall within the system bandwidth. It is therefore important to define a referent pattern frequency f_p , as well as a non-null integer n tuning the pattern shape, frequency content and duration. These two parameters constraint the pattern shape and speed. With this in mind, we can construct our equations so that each pattern may have a similar bandwidth and the same period $T_p = n/f_p$. Therefore, they have the same number of laser beams.

6.3.1.1 lissajous

The lissajous is a popular pattern used for detection and tracking in diverse laser scanning systems. We reduce here its expression to $(n, n + 1)$ forms. The pattern expression is

$$\begin{cases} \theta = \frac{A_p}{2} \sin(2\pi f_p t) \\ \varphi = \frac{A_p}{2} \sin\left(2\pi \left(\frac{n+1}{n}\right) f_p t\right) \end{cases}, \text{ with } t = \frac{k}{f_l}, k \in \mathbb{N}. \quad (6.24)$$

Its frequency content is purely harmonic.

6.3.1.2 Triangular raster-scan

The raster-scan is probably the most used pattern for scanning a zone. Several versions exist, with different types of waveform to control each axis. Here, we use the one that shows the highest uniformity [Nguyen *et al.* 2017b]. It is comprised of a stair waveform on one axis, and a triangle waveform on the other. The pattern expression is

$$\begin{cases} \theta = \frac{A_p}{2} \sum_{i=0}^{2\gamma n-1} \left(\frac{2i}{2\gamma n-1} - 1\right) \chi_i(t) \\ \varphi = \frac{A_p}{2} \text{tri}(2\pi\gamma f_p t) \end{cases}, \text{ with } t = \frac{k}{f_l}, k \in \mathbb{N}. \quad (6.25)$$

where tri is the triangle function and

$$\chi_i(t) = \begin{cases} 1 & \text{if } t \in \left[T_p \frac{i}{2\gamma n}, T_p \frac{i+1}{2\gamma n}\right] \\ 0 & \text{otherwise.} \end{cases} \quad (6.26)$$

γ is a real number that modifies the slope of the triangle function, creating more "folds" in the raster-scan within the fixed period T_p .

6.3.1.3 Spirals

We define a generic spiral of radius r_s and angle ψ_s across time by the following expression

$$\begin{cases} r_s(t) = \frac{A_p}{2} \left(1 - \frac{f_p t}{n}\right)^\alpha \\ \psi_s(t) = 2\pi n \frac{1}{\beta} \left(1 - \frac{f_p t}{n}\right)^\beta \end{cases}, \quad (6.27)$$

with A_p the spiral initial diameter, and α and β real numbers tuning the way the spiral amplitude and frequency behave with time. The complete 3D parametric representation is therefore

$$\begin{cases} \theta = \frac{A_p}{2} \left(1 - \frac{f_p t}{n}\right)^\alpha \cos\left(2\pi n \frac{1}{\beta} \left(1 - \frac{f_p t}{n}\right)^\beta\right) \\ \varphi = \frac{A_p}{2} \left(1 - \frac{f_p t}{n}\right)^\alpha \sin\left(2\pi n \frac{1}{\beta} \left(1 - \frac{f_p t}{n}\right)^\beta\right) \end{cases}, \text{ with } t = \frac{k}{f_l}, k \in \mathbb{N}. \quad (6.28)$$

The frequency content is very dependent on the value of β , which tunes the way the instantaneous frequency increases with time.

In Fig. 6.8, we represent low complexity patterns with $n=3$, which can be drawn by mechanical elements, such as scanning mirrors, at a frequency higher than 100 Hz. They can be used for local imagery with small angular field of view at high refresh rate. The number of laser beams inside a pattern is defined by $N=f_l n/f_p$. Here, we choose to use 100 pulses to accentuate the difference between patterns.

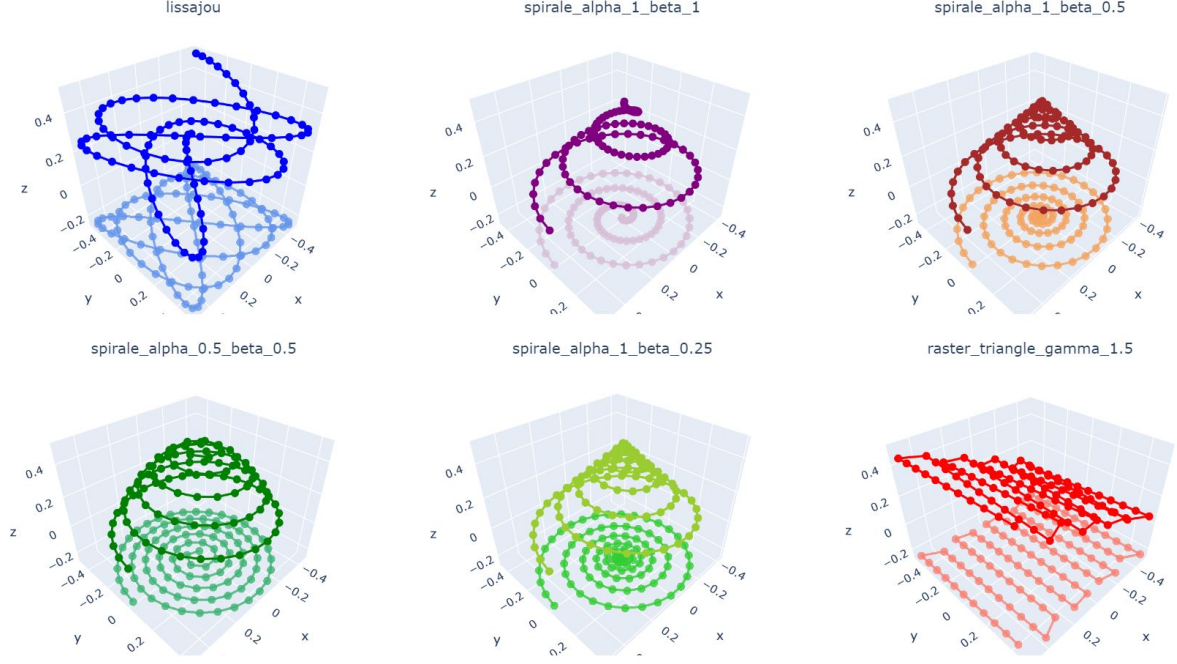


Figure 6.8: 3D representation and 2D projection of Lissajous, spirals and raster-scan with different values of α , β and γ , for $n=3$. z is the time axis. The round markers represents the laser beams, at a number of $N=100$ shown here.

6.3.2 Patterns ranked as a function of the probability of intersection

When one beam is sent to the scene, as seen previously, the probability to get an echo is depending of a vast number of parameters. There is the angular offset ψ between the center of the beam and the object to image, the object shape and orientation, the beam profile, divergence and energy density, etc... To compare patterns independently of these considerations, we have to reduce our intersection problem. Under a certain number of assumptions, it is possible to consider that an echo is obtained if the target is within the vicinity of a laser beam. By taking the supposition that the target is a flat lambertian disk surface and the beam Gaussian, the neighborhood can be assumed to be a disk. We can then assume the following proposition for the probability of detection \mathcal{P}_d :

$$P_d = 1 \iff \exists t \text{ such as } \psi(t) \leq \varepsilon, \quad (6.29)$$

with t the time and ε the minimal planar distance between the laser beam center and the object to image. ε usually decreases with range, as a result of losses in power density in the laser beam (due to divergence). At the very range limit of the system, we can consider a punctual

intersection with $\varepsilon=0$. With this simplification done, we can begin our study by considering the laser beam coordinates across the three-dimensional space (θ, φ, t) .

We can define holes in the laser pattern as the 3D coordinates (θ, φ, t) where the probability of intersection is null. As mentioned previously, we wish to minimize these holes. In order to achieve this, we need to introduce three quantities, each one overlapping a direction almost orthogonal to the other in our 3D space. We choose to use a local coordinate system (l, Γ, t) , which slides and deforms along the pattern curve (see Fig. 6.9). l is the curvilinear abscissa, representing the distance traveled by the laser beam across time t . Γ represents the void left when the pattern loops back onto itself, and is pattern dependent, which requires its own development.

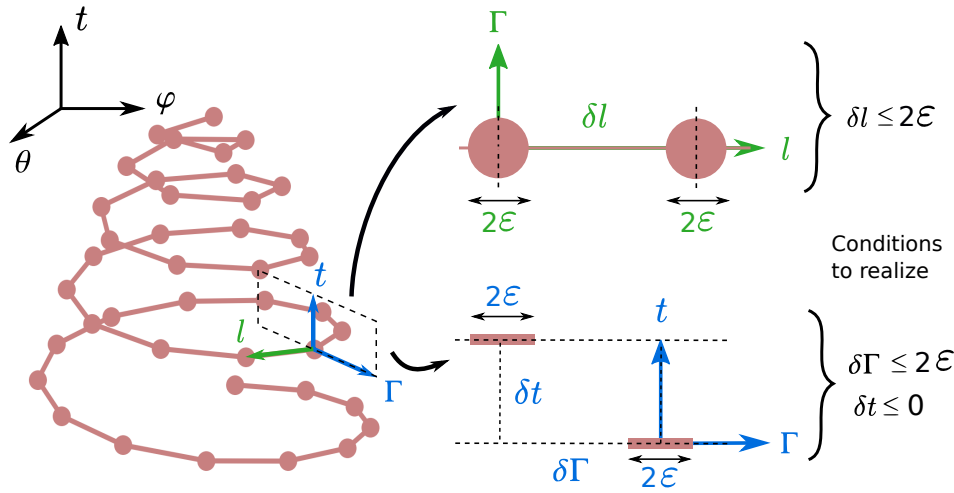


Figure 6.9: Definition of $(\delta l, \delta \Gamma, \delta t)$ with a spiral example. We can deduce three conditions to obtain an optimal, dense pattern.

The expression of the curvilinear abscissa l is given by the following integral:

$$l(t) = \int_0^t \sqrt{\frac{d\theta(\tau)^2}{d\tau} + \frac{d\varphi(\tau)^2}{d\tau} + \left(\frac{d(V_c\tau)}{d\tau}\right)^2} d\tau . \quad (6.30)$$

Here we have to multiply the time axis by a given speed V_c , to be able to scale it correctly compared to θ and φ . V_c represents here the speed of an object to image on the scene, and is equal to zero for static scenes. The distance δl between two consecutive laser beams, fired at a laser repetition rate f_l , is then given by

$$\delta l(t) = l\left(t + \frac{1}{f_l}\right) - l(t) . \quad (6.31)$$

δl gives access to the size of the holes along the curvilinear abscissa direction.

In the direction Γ , a hole is created between two rows of laser beams when the pattern loops back onto itself. The rows are delimited by the minima and maxima of a given function (discussed in the next paragraphs), which is pattern dependent, and are shown for three pattern type in Fig. 6.10. The planar distance in this direction is named $\delta \Gamma$. There are two kinds of patterns that have this coiling behavior:

- the ones that sporadically change direction (most patterns : raster, Lissajous, roses, etc...),
- the ones that continuously loop back onto themselves (circles and spirals).

It can be numerically analyzed by studying the behavior of the curvilinear abscissa direction $\Omega = \arctan(d\varphi/d\theta)$, or its derivative $d\Omega/dt$, across time. The results are displayed in Fig. 6.10 for a selection of patterns. We can see on this figure that it is possible to pinpoint the instant at which the pattern loops back into itself, either by the local extrema of $d\Omega/dt$, or by the 2π increment of Ω . $\delta\Gamma$ can then be computed for each laser beam as the planar distance between the current beam and its equivalent on the next row. The last orthogonal quantity, named δt , is simply the time difference between the instant these two beams were fired.

To formalize this description for patterns that sporadically change direction, let's define E as the set of laser beams on the current row, and F as the set of laser beams on the next row, each set being delimited by the conditions of Ω or $d\Omega/dt$ previously mentioned. τ_E is the corresponding time width of the set E . A laser beam i of the set E is fired at the time t_i , taken relative to the beginning of the set. The same can be proposed for set F . Then, for each laser beam i of the set E , it exists a corresponding laser beam j of the set F defined by $t_j = (t_i/\tau_E)\tau_F$, or by its closest value. Once found, we can then compute $\delta\Gamma$ and δt by

$$\begin{cases} \delta\Gamma(t_i) = \sqrt{(\theta(t_j) - \theta(t_i))^2 + (\varphi(t_j) - \varphi(t_i))^2} \\ \delta t(t_i) = t_j - t_i \end{cases} \quad (6.32)$$

For patterns that continuously loop back onto themselves, such as spirals, we would rather use the expression of Ω . Indeed, because the function is monotonous for each set E or F (cf Fig. 6.10, A left), we can simply pair t_i and t_j by computing

$$t_j = \operatorname{argmin}(\Omega_E(t_i) - \Omega_F) \quad \Omega \frac{d\Omega}{dt} \quad (6.33)$$

And then using Eq. (6.32) to find $\delta\Gamma$ and δt . An illustration is presented in Fig. 6.10.

We have defined three quantities (δl , $\delta\Gamma$, δt), mostly orthogonal between each other and representing holes left in the pattern in every direction. A 3D representation of these quantities is made in Fig. 6.9 with a spiral example. On this figure is also reported the intersection condition with the parameter ε . We can see from the figure that to minimize holes, we need:

$$\begin{cases} \delta l(t_i) \leq 2\varepsilon \\ \delta\Gamma(t_i) \leq 2\varepsilon, \text{ for } i \in [1, N] , \\ \delta t(t_i) \leq 0 \end{cases} \quad (6.34)$$

with $N = f_l T_p = f_l n / f_p$ the number of laser beams per pattern. Because at the limit, we have $\varepsilon \rightarrow 0$, we see that the previous set of equations is reduced to minimizing the three quantities to obtain the optimal pattern. To get a sense of the size of the holes on each direction, we computed δl , $\delta\Gamma$ and δt as a function of the curvilinear abscissa l using Eq. (6.31) and (6.32). We then reduced these three parameters by using an average Δ of expression:

$$\Delta(t_i) = \frac{\delta l(t_i) + \delta\Gamma(t_i) + V_c \delta t(t_i)}{3}, \text{ with } V_c = \frac{A_p}{2T_p} \text{ and for } i \in [1, M]. \quad (6.35)$$

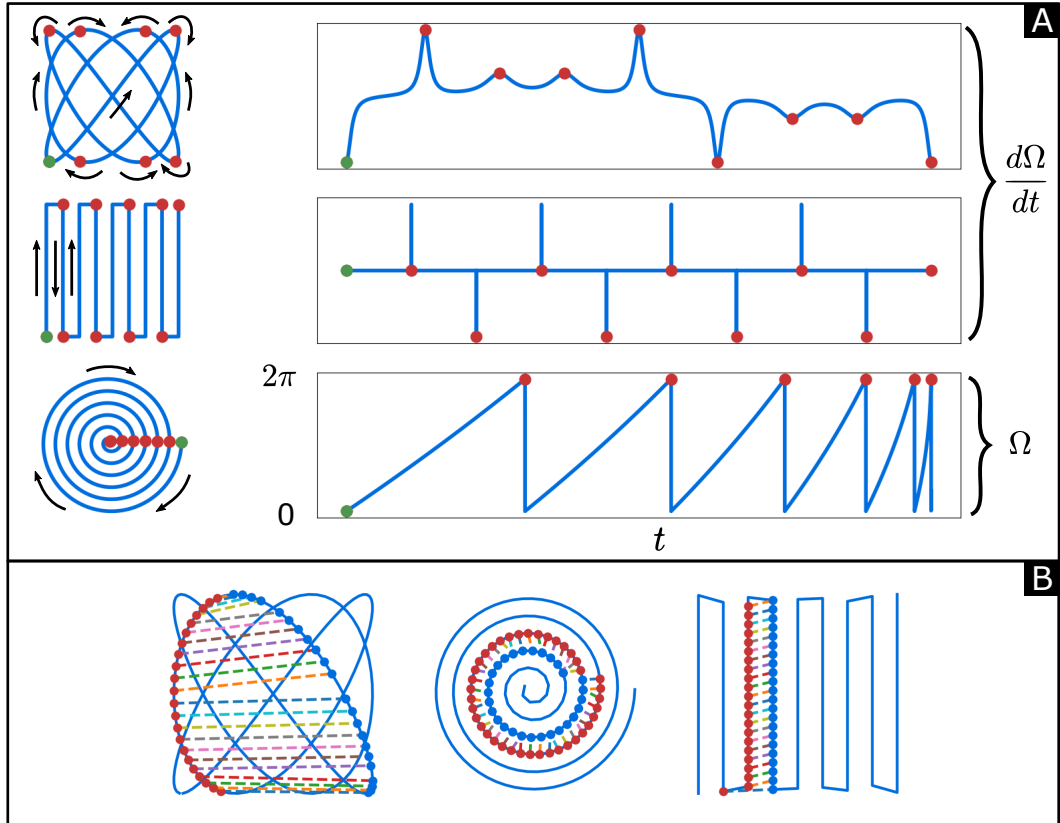


Figure 6.10: (A, left) Plots of Lissajous, raster-scan ($\gamma=3/2$) and spiral ($\alpha=1/2, \beta=1/2$) in the (θ, φ) plane, for $n=3$. (A, right) Corresponding $d\Omega/dt$ and ω as a function of time. For Lissajous and raster-scan, the local extrema of $d\Omega/dt$ defines the loop-back instant (red dots) and separates the rows. For the spiral, it corresponds to every 2π increment of Ω . Ω has clockwise positivity here. (B) Representation of $\delta\Gamma$ as the multicolor dotted lines between one laser beams row (red round markers), and their equivalent on the next row (blue round markers).

Here again we have to use the speed V_c to scale δt to the other angular dimensions. V_c can be a constant, for instance chosen as $V_c = A_p/(2T_p)$, with A_p the scanned FoV. This way, we can consider that an object starts at the center and reaches the boundary of the pattern during a period. The optimal pattern would have Δ as small as possible for every position on its curvilinear abscissa. To reduce even more the number of parameters, we can consider the mean μ_Δ and standard deviation σ_Δ of this quantity. An optimal pattern would have μ_Δ as low as possible, and a low dispersion, so that the conditions from Eq. (6.34) are satisfied all along the pattern.

In the end, we obtain two criteria, which are a function g of a number of parameters:

$$\mu_\Delta, \sigma_\Delta = g(\text{type}, n, f_p, f_l, v_c) \quad (6.36)$$

with "type" the type of pattern, including specific parameters such as α, β, γ .

For the numerical comparison, we limit ourselves to the Lissajous, the raster-scan $\gamma=3/2$, and the spiral $\alpha=1/2, \beta=1/2$. This spiral is also called the constant linear velocity (CLV) spiral and has been used in atomic force microscopy [Mahmood & Moheimani 2010] and optical discs [Christodoulakis & Ford 1989], precisely for its scanning uniformity. Our constraint for this comparison is that all patterns must have the same total curvilinear abscissa $l(T_p)$. This means that during a pattern period, the same length is traveled, or that the average drawing speed is equal for all three patterns. This is true for a wide values of n , represented in Fig. 6.11. We can see on this figure that the maximum difference is around 10 %.

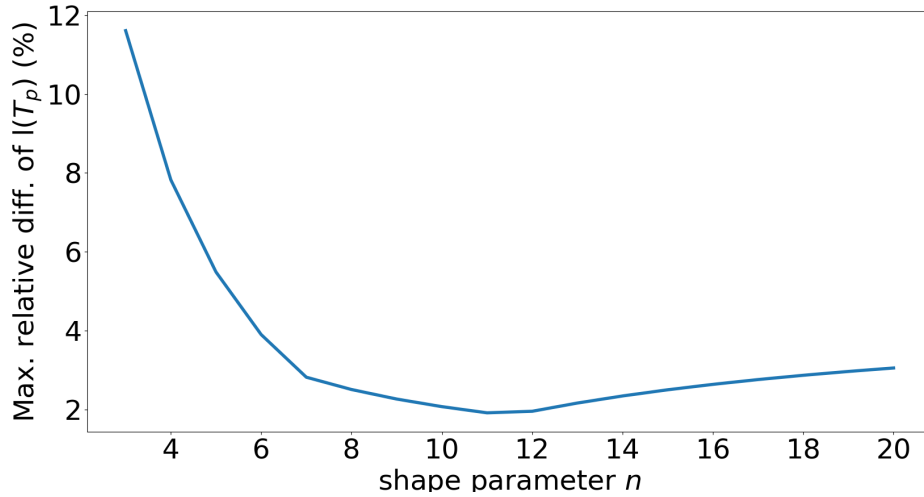


Figure 6.11: Maximum relative difference of the total curvilinear abscissa $l(T_p)$ between the Lissajous, raster-scan $\gamma=3/2$ and CLV spiral ($\alpha=1/2, \beta=1/2$) as a function of n .

Using these patterns with $n=3$, we present Δ as a function of l in Fig. 6.12. The optimal pattern would have Δ as small as possible for every position on its curvilinear abscissa. To reduce even more the number of parameters, we can consider the mean and standard deviation of this quantity. An optimal pattern would have a small average value of Δ , and a low dispersion, so that the conditions from Eq. (6.34) are satisfied all along the pattern. This is plotted in Fig.

6.12. The dominant term in Δ is always δT , and on the contrary δl is mostly negligible due to the high laser repetition rate compared to the pattern period.

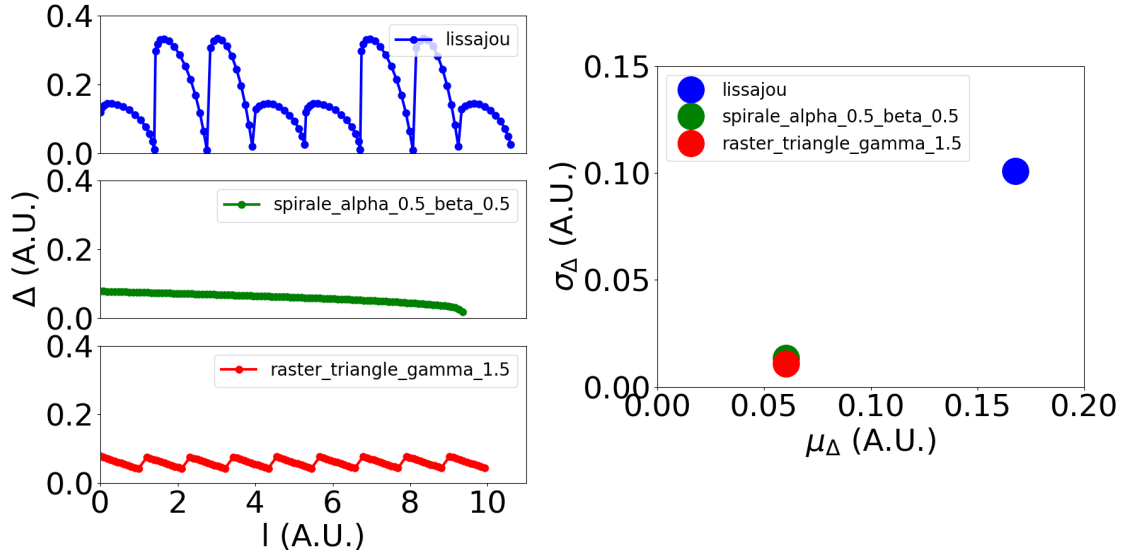


Figure 6.12: (Left) Δ as a function of the curvilinear abscissa l for the Lissajous (up), CLV spiral ($\alpha=1/2$, $\beta=1/2$) and raster-scan $\gamma=3/2$. (Right) σ_Δ as a function of μ_Δ . The patterns in lower left corners (minimizing mean and std) are better. All the patterns are computed for $n=3$ and are composed of 100 laser beams. They are shown in Fig. 6.8 with the same color code.

One major conclusion that can be drawn from Fig. 6.12 is that Lissajous are not very efficient pattern types in terms of uniformity of beam distribution. They offer a high density of beams in the corners compared to the center and show very large holes in the middle. The CLV spiral is much more uniform. The raster-scan show the same uniformity. Nevertheless, if the purpose is to trap targets in our tracking mode, it seems logical to go for a spiral, which circles around it and should maximize the probability of intersection. In the case of the raster-scan, the sequential left-to-right scan allow for the right space to stay unscanned for a good portion of its period.

6.4 Scanning frequency limitations

Now that we have seen the theoretical aspect of the detection, we must make sure that our physical system is able to draw these patterns at the chosen period. We must then look at the frequency limitations for our patterns. The mechanical bandwidth of the scanner is the main one. Nevertheless, the round-trip travel of light can also restrict the scanning speed.

6.4.1 Light round-trip travel

In our monostatic setup, when the pulse is fired, the scanner is oriented at a given direction (θ, φ) . Then, the pulse travels toward the scene at the light velocity in the medium (the atmosphere), c . At the same time, the scanner is not static but driven at a given frequency, which means that the angular pointing coordinates are continuously shifted. When the light scatters on an

object and travels back to the scanner, its is oriented at a given direction (θ_b, φ_b) . The APD instantaneous FoV, FoV_i , must be wide enough to include the previous orientation (θ, φ) , added to the laser beam divergence Θ_b . Because the FoV is often minimized to reduce background noise (see previous chapter), the limitation is more toward the frequency at which the scanner is driven. These considerations are illustrated in Fig. 6.13.

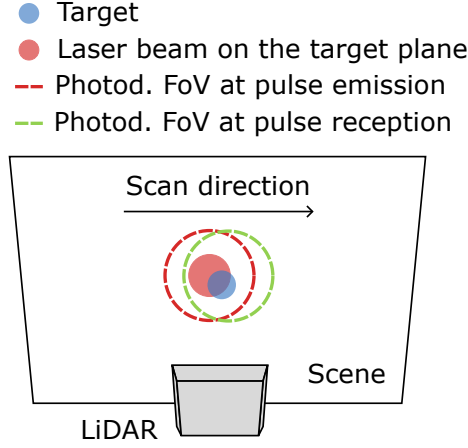


Figure 6.13: Illustration of the photodetector FoV_i angular displacement during the round-trip travel of light when scanning.

From this figure, we can see that the scanner angular driving speed V_θ must be limited by the following equation:

$$V_\theta \frac{2R}{c} \leq \text{FoV}_i - \frac{\Theta_b}{2}, \quad (6.37)$$

with R the target range. If we consider the worst case (fastest) of a triangular waveform of amplitude A_p and frequency f_c , then the driving speed is $V_\theta = A_p \cdot 2 f_c$. We then obtain the following limitation:

$$f_c^{rt} = \frac{c}{2R} \left(\frac{\text{FoV}_i - \Theta_b/2}{2A_p} \right). \quad (6.38)$$

This limit f_c^{rt} must be compared to the actual mechanical limits of the beam steerer.

6.4.2 Scanner bandwidth

In our platform, the beam steerer is a dual-axis galvanometer unit. Details are provided on chapter 7. We performed measurement of the mechanical bandwidth at multiple amplitudes. This measurement was made by driving the galvanometer with a sinus of constant amplitude but increasing frequency across time (chirp). The amplitude response can be read from the position detector, which was demodulated to obtain both the amplitude and phase response. From these curves, we found the cutoff frequency f_c of the system as the function of the peak-to-peak drive in optical radiant, A_p (see Fig. 6.14). It is important to note that both axis have very similar bode diagrams, despite one mirror being significantly larger than the other.

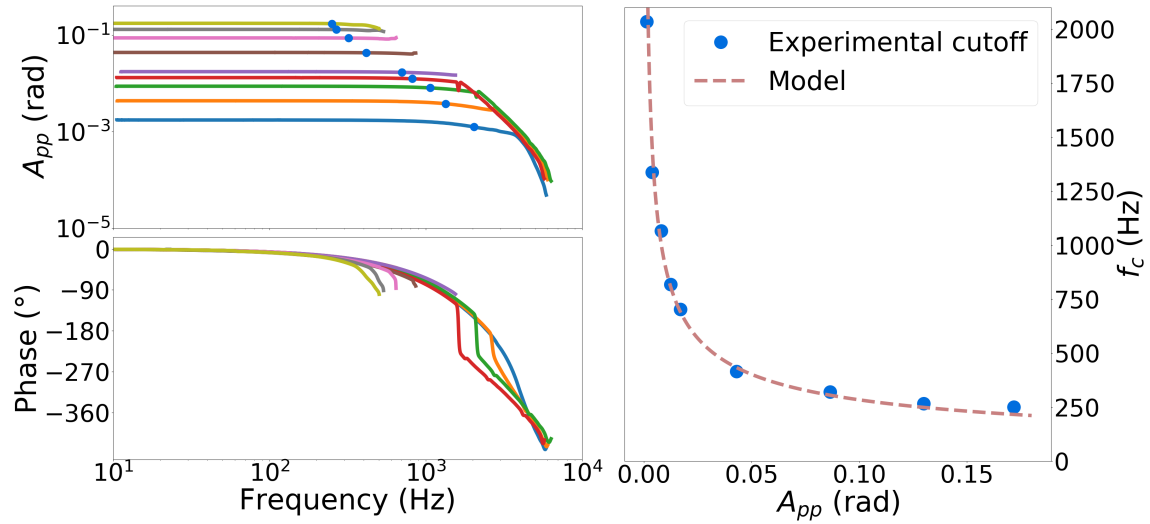


Figure 6.14: (Left) measured bode diagram of the galvanometer for driving peak-to-peak amplitude from 0.1° to 10° optical (1.7 mrad to 0.17 rad). The blue dots represents the extracted cut-off frequency. (Right) Cutoff frequency as a function of peak-to-peak amplitude.

The cutoff frequency was chosen as half the argument of the derivative maximum of A_p , so as to keep a reasonable margin. It can be model by a relatively simple expression:

$$f_c = \left(\frac{a_{fc}}{A_p} \right)^{b_{fc}} = \left(\frac{34390}{A_p} \right)^{0.45}, \quad (6.39)$$

with $a_{fc}=34390 \text{ rad.s}^{-1/b_{fc}}$ and $b_{fc}=0.45$. This expression is important to be able to place the frequency limits at which the patterns can be used. This limits applies to pure sinus, but can be extended to more complex waveforms. Using this equation and our patterns described previously, we can find their frequency limitations.

6.4.2.1 Lissajous

The Lissajous is a pure sinus on both axis. The frequency limit relative to the referent frequency f_p can be found from Eq. (6.24). We have to look at the fast axis, which is a function of n :

$$f_p < f_c^{liss} = \left(\frac{a_{fc}}{A_p} \right)^{b_{fc}} \frac{n}{n+1}. \quad (6.40)$$

6.4.2.2 Triangular raster-scan

For the triangular raster-scan, we are only considering the fast-axis triangular waveform, which is the bottleneck. This waveform contains an infinity of odd harmonics m . Thankfully, their amplitude scales with $1/m^2$, which means that in practice higher frequencies becomes negligible very quickly. The amplitude of the harmonics m , noted A_m , is given by:

$$A_m(m\gamma f_p) = \frac{A_p}{m^2} . \quad (6.41)$$

We wish to find the limitation of the referent frequency f_p for the harmonic m to have an amplitude within the characterized beam steerer bandwidth. From Eq. (6.39), the amplitude limitation given by the scanner as the function of frequency is $A_c = a_{fc}/f^{(1/b_{fc})}$. The limitation in amplitude imposed by the beam steerer is then:

$$\begin{aligned} A_m(m\gamma f_p) &< A_c(m\gamma f_p) \\ \text{i.e. } \frac{A_p}{m^2} &< \frac{a_{fc}}{(m\gamma f_p)^{\frac{1}{b_{fc}}}} \end{aligned} \quad (6.42)$$

Finally, we obtain the following frequency limit f_c^{tri} :

$$f_p < f_c^{tri} = \left(\frac{a_{fc}}{A_p} \right)^{b_{fc}} \frac{m^{2b_{fc}-1}}{\gamma} . \quad (6.43)$$

6.4.2.3 Spirals

Concerning the spirals, except for cases where $\beta=1$, (including the constant angular velocity (CAV) spiral $\alpha=1, \beta=1$), frequency is not constant during a period. The amplitude, which starts at A_p , decreases with time as well. Thus, we have to find an expression for the frequency as a function of the instantaneous peak to peak amplitude A_{inst} to find the frequency limit. We can use Eq. (6.28) to get the instantaneous frequency f_{inst} :

$$\begin{cases} f_{inst} = \frac{1}{2\pi} \frac{d}{dt} \left| 2\pi \frac{n}{\beta} \left(1 - \frac{f_p t}{n} \right)^\beta \right| \\ A_{inst} = A_p \left(1 - \frac{f_p t}{n} \right)^\alpha \end{cases} . \quad (6.44)$$

We finally get:

$$f_{inst} = f_p \left(\frac{A_{inst}}{A_p} \right)^{(\beta-1)/\alpha} \quad (6.45)$$

To set a proper limit for the frequency, we have to choose an amplitude at which the frequency should be behind the limits defined by Eq. (6.39). We can choose a fraction $1/m$ of the initial amplitude A_p , such that $A_{inst} = A_p/m$, at which the frequency should be equal to the scanner limitations. We have to solve the following equation:

$$\begin{aligned} f_{inst} &< f_c \\ \text{i.e. } f_p \frac{1}{m^{(\beta-1)/\alpha}} &< \left(\frac{a_{fc}}{A_p} m \right)^{b_{fc}} \end{aligned} \quad (6.46)$$

Finally, we obtain the following frequency limit f_c^{spi} :

$$f_p < f_c^{spi} = \left(\frac{a_{fc}}{A_p} \right)^{b_{fc}} m^{(\alpha b_{fc} + \beta - 1)/\alpha} . \quad (6.47)$$

6.5 Conclusion

In this chapter we presented the dynamic model we developed for the three modes of our system: detection using a raster scan, intrusion using a circle and tracking using a self-adjusting pattern. For detection and intrusion, we used a simplified target model to link the patterns key parameters to the probability of echoes. The impact of the speed was also quantified. Regarding tracking, we focused our efforts into ranking patterns regarding their likelihood to produce an echo. The frequency limitations of the scanner is also modeled and applied to our patterns. An overview is presented in Table 6.1.

The work presented in subsection 6.1.1 was published in an open-access, unpeer-reviewed paper [Quentel *et al.* 2020]. A previous version of the work presented in subsection 6.1.2 was published in an international peer-reviewed paper [Quentel *et al.* 2019].

	Model based on	Parameters included	Advantages	Drawbacks
Detection	Surface overlap function	Link budget + $\delta_\theta, \delta_\varphi, A_\theta, A_\varphi, f_l, T_{\text{scan}}, A_c, V_c$	End-to-end model (from geometry to link budget to probability), multi or single echo, impact of target speed	Computation time, no-closed form, uniform lambertian reflectivity assumption
Intrusion		Link budget + $\delta_i^o, \delta_i^r, f_i, A_s, A_s, V_i$		
Tracking	Pattern beam density	Any pattern parameters. Most uniform pattern is CLV spiral with $\alpha=1/2, \beta=1/2$	Fast computation, can be applied to any pattern	No target speed, no impact of pattern diameter or frequency on probability of echo

Table 6.1: Summary of the models developed in this chapter.

Experimental platforms

Contents

7.1 Platform components	79
7.1.1 Laser source	79
7.1.2 Beam steerer	82
7.1.3 Photodetector	83
7.1.4 Beam separator & collimation optics	87
7.1.5 Bandpass filter & transmission coefficients	90
7.2 System overview and control electronics	94
7.3 Platform integration	96
7.4 Conclusion	99

In this chapter, we present the experimental realization of the LiDAR described in the previous chapters. Due to the industrial ties of this PhD, the platform and its integration accounted for a significant amount of the candidate efforts and time. In some sections the presentation is divided between two platform types, the first prototype using a beamsplitter (BS) for beam separation, and the second using a holed off-axis parabolic mirror (PM). Components were carefully selected and characterized for best performance, which lead to this design changes between the two version.

In this chapter, the candidate wishes to show the plurality of fields that needed to be addressed to build a functional LiDAR prototype, steaming from optics to analog and digital electronics, including real-time programming. Component sourcing, electrical and mechanical integration were also addressed during integration.

7.1 Platform components

In this section we describe the components used in the two platforms, as well as their main characteristics.

7.1.1 Laser source

Considering the range we wish to obtain, we need a high peak power laser source with a good beam quality. To reduce scanning time, we also require a high pulse repetition frequency (PRF). If we refer to the specifications, we need to be able to scan $10^\circ \times 10^\circ$ optical in less than 10 s. If we use for the scan resolution the drone dimension (30 cm at 1 km), then we have from Eq. (4.7)

$$f_l = \frac{A_\theta A_\varphi}{\delta_\theta \delta_\varphi} \frac{1}{T_{\text{scan}}} > \frac{10^2}{0.017^2} \frac{1}{10} = 35 \text{ kHz} . \quad (7.1)$$

This gives us a rough value of the needed **PRF**. On the other end, the maximal **PRF** is given by the pulse travel time. Indeed, if a pulse is fired before the previous one had time to arrive, then a simple threshold can not discriminate if the return was from the first or the second pulse. The maximal value is then

$$f_l < \frac{c}{2R_{\text{max}}} = \frac{3e8}{2 * 1e3} = 150 \text{ kHz} . \quad (7.2)$$

Regarding the pulse width, we are not very constrained in range precision (1 m). This means that we can use a relatively long pulse, ie more than 5 ns, which relaxes the bandwidth of the photodetector, reducing noise and improving the overall link budget. The longer the pulse width, the lower the range precision, but the higher the SNR will be.

After a broad research, the laser selected is a fiber laser of the french company Keopsys (from Lumibird group), using a 1545 nm wavelength. Wavelength selection was covered on subsection 4.3.3. The gain medium of this type of laser is a fiber, which has been doped with Erbium elements. The fiber is pumped at another wavelength to realize population inversion and stimulated emission. This particular model is a distributed feedback laser (**DFB**), meaning that the cavity is created by periodical structures within the fiber, which provides optical feedback. Major operational characteristics are its very high beam quality, high peak power and **PRF** while maintaining a very small package. This type of laser is specifically designed for long range **LiDAR** applications. The specifications of the laser are shown in Table 7.1, and the laser itself is presented in Fig. 7.1.

Parameter	Value
Model	PEFL-K08-RP-020-010-1545-T1-ET1-PK2A-FA (Keopsys/Lumibird)
Type	Single mode fiber laser, Erbium doped
Size	Circular, 90 x 20 mm
Weight	200 g
Consumption	20 W
Recommended PRF	50 kHz
Pulse width (FWHM)	9.7 ns
Central wavelength	1544.4 nm
Energy bandwidth	99.9 % at +/- 1 nm
Average power	1.25 W
Peak power	2.5 kW at 50 kHz
M^2	<1.1

Table 7.1: Characteristics of the laser source selected.

This laser provided the best ratio between peak power and pulse width that we could find at the time with such a small package (at the end of 2017). Slightly higher peak power was possible with lower pulse width, but the needed bandwidth of the **APD** would possibly negate

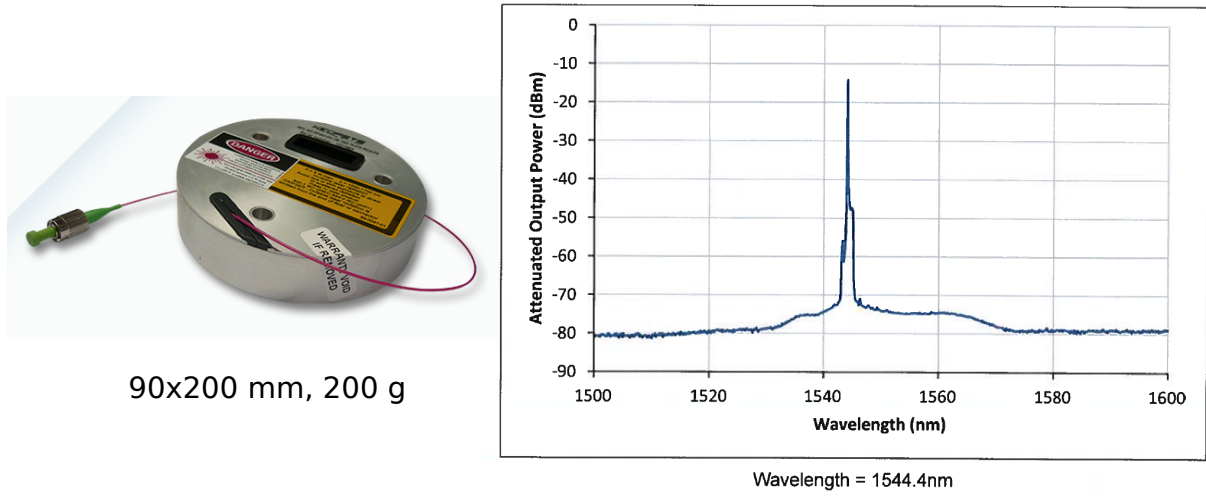


Figure 7.1: (Left) picture of the laser source of the LiDAR. (Right) measure of the central wavelength and energy bandwidth [supplier data].

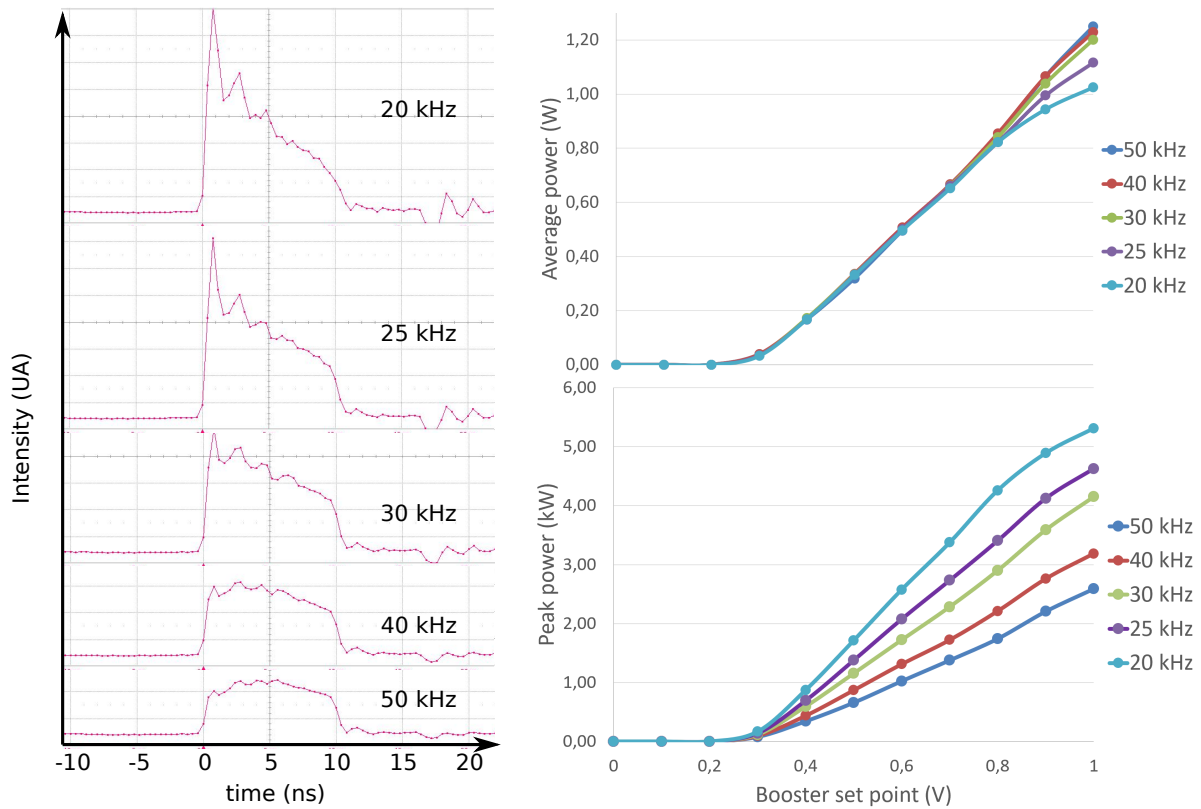


Figure 7.2: (Left) laser pulse shape as a function of the PRF using a 1.2 GHz photodiode. The reduction of HWHM is clearly visible. (Right) measured average and deduced peak power (supposing a 9.7 ns square pulse) as a function of the current drive and the PRF.

this advantage. The laser can be operated at a lower PRF than the 50 kHz specified so as to increase peak power. There is however a lower limit that should not be crossed, as too much peak power can damage the laser. Measures of the evolution of pulse shape and average power as a function of the PRF is shown in Fig. 7.2.

We can clearly see on this figure that reducing the PRF results in more peak power. This is due to a higher accumulation of energy between pulse. Nevertheless, the energy is not uniformly distributed within the pulse. We can observe that the shape becomes much more triangular as the PRF decreases, meaning that a higher portion of the energy is emitted at the beginning of the pulse compared to the end. As a result, the absolute peak is observed to be 4 times higher at 20 kHz compared to 50 kHz, even if there is only a theoretical 2.5 increased in energy. It could be even higher as we were limited by the 1.2 GHz bandwidth of the photo-diode used.

In any case, a lower PRF is linked to a higher peak power but also a sharper peak. Therefore the real gain in operation has to be measured using the final LiDAR APD, which may have a too limited bandwidth to take full advantage of this effect. Moreover, good thermal coupling between the laser and the supporting structure is necessary to dissipate power and maintain a stable temperature, otherwise power will drop. The study of the APD responsivity was done on section 5.3 and 7.1.3.

7.1.2 Beam steerer

As detailed on chapter 4, the architecture chosen is mono-static, meaning that the same beam steerer is used for both emission and reception. The aperture of the beam scanner is thus shared, limiting both the beam divergence Θ_b and the collection aperture D_r . To maximize the link budget from Eq. (5.21), we would want an aperture as big as possible. At the same time, we wish to preserve a high mechanical bandwidth for high speed scanning, most notably during tracking where a 200 Hz localization rate is needed.

For our application, the most important parameter is probably the aperture. Because we wish to detect small drones at one kilometer, we need to collect as much photon as possible. If we look at Table 2.1 in chapter 2, we can see that for this reason alone, the MEMS mirror and the OPA are not adapted. Another issue is the angular pointing precision and resolution. To reach our goal, we need high stability, repeatability and positioning with a resolution of at least a few tens of microradian (a 30 cm drone is 300 μ rad at 1 km). Open loop systems simply cannot guarantee that type of precision, as they are not robust to environmental variations, especially temperature. Overall, the galvanometer appears to be the best option, the only drawback being its size and power consumption.

A two dimensional galvanometer scanner is comprised of two actuators which rotates each mirror along its axis of rotation. The actuator is built on the rotor/stator concept, one being a coils and the other a permanent magnet [Aylward 2003]. The torque providing the rotation is therefore created by magnetic forces, and the rotor is suspended by a bearing technology. To reach the precision we need, the device must be made with quality precision engineering, which does not come without costs. Friction on the bearing can also wear the device and should be taken into account regarding its lifetime.

The angle of incidence on each mirror at the 0 position is 45°. As each axis is independent, the laser is first reflected by the first mirror, then travels up to the second one. This causes the first axis to "scan" the second axis mirror along one dimension. Therefore, the second mirror has

to be longer than the first to preserve the aperture. This means that dual axis galvanometers possesses a slow and fast axis, corresponding to the small and larger mirror, even though it is often corrected by the servo-controller to present identical characteristics on both axis.

The galvanometer we selected is from the German company Scanlab, which is specialized in these systems, usually for laser engraving applications. We got the biggest aperture available with an analog, ± 10 V command, which is 14 mm. This size is a good compromise between aperture and bandwidth. It is delivered with two electronic servo-boards, each one controlling a single axis. The complete specifications are given in Table 7.2.

Parameter	Value
Model	hurrySCAN III 14 Module, Analog (Scanlab)
Type	Dual axis galvanometer scanner
Size	136x90x101 mm
Weight	1.2 kg with holder
Consumption	30 W max per galvo, 60 W total
Aperture	14 mm
Mirror size	fast axis : 24x15.5 mm, slow axis : 35x30.8 mm
Optical FoV	40°x40°
Command input range	± 9.6 V, full optical FoV, 42.5 mrad/V conversion
Position output range	± 4.8 V, full optical FoV, 85 mrad/V conversion
Position detector	Optical (possibly shadow casting)
Optical resolution (sensor noise limited)	$\sim 10 \mu\text{rad RMS}$
Mirror coating	Dielectrically enhanced silver, $\eta_g=98$ % transmission per mirror at 1545 nm (extrapolated from similar coatings)

Table 7.2: Characteristics of the galvanometer selected.

in Fig. 7.3 is shown a picture of the unit and the servo boards. It is interesting to note that the angular noise is around $10 \mu\text{rad RMS}$. This means that to take full advantage of the resolution, we have to use a 16 bits resolution control electronics ($2^{15} < 0.408 \text{ rad}/10 \mu\text{rad} < 2^{16}$). Bode diagram were not available, so we had to perform measurements ourselves, shown in Fig. 6.14 on the previous chapter. Both axis have very similar bode diagrams, despite one mirror being significantly larger than the other, which is possibly the result of a factory-set compensation within the electronic servo board to equalize the response of both axis.

7.1.3 Photodetector

For sensitivity reasons, we are using an APD as our photodetector. But beyond sensitivity, at least two other parameters should be considered. The first one is the diameter of the APD, which is directly related to the detector instantaneous FoV. We need to have FoV_i at least greater than the beam divergence to collect as much photon as possible. We can obtain a condition on the APD diameter D_{APD} from Eq. (4.3):

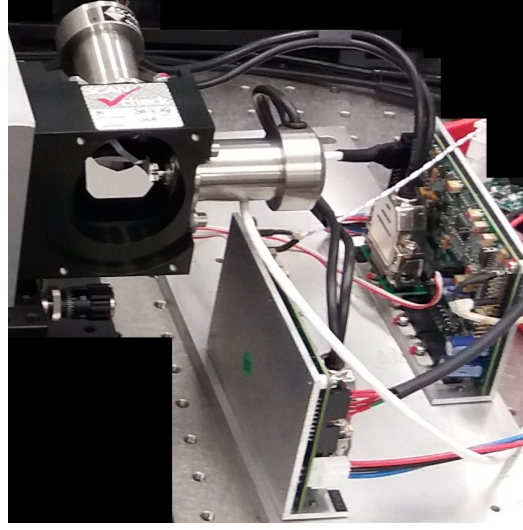


Figure 7.3: Photo of the galvanometer unit and its two servo boards.

$$\text{FoV}_i > \Theta_b \iff D_{\text{APD}} > fo\Theta_b , \quad (7.3)$$

with fo the focal of the detection chain. A smaller D_{APD} improves the noise figure of the APD (less primary dark current), and decreases the background average power, which scales as the square of the FoV_i , as seen from Eq. (5.27). The other parameter is related to bandwidth B . It should be high enough to respond to the short pulse, but not too high because the noise standard deviation scales as \sqrt{B} , as seen on Eq. (5.28). B is directly limited by the TIA used to build the APD sensor. If we consider a perfectly square pulse and a perfect sensor with a flat response, then the optimal bandwidth is the one which maximize the peak. It can be approximated by

$$B \sim \frac{1}{\tau_p} , \quad (7.4)$$

with τ_p the laser pulse width. In our case, we should use a sensor with a flat bandwidth close to 100 MHz. Moreover, a low-cut should be performed to remove slow moving fluctuations and continuous powers (from background illumination).

We used two different APD in our two different setups, which were changed for performance issues. The noise and probability of detection study presented on section 5.3 was done with the latest APD of the platform PM.

7.1.3.1 Platform "beamsplitter"

The first photodetector used is an APD from the company LaserComponent. The detector includes the APD, the trans-impedance amplifier as well as a way to control the bias voltage. Detailed specifications are shown in Table 7.3, and a picture is presented in Fig. 7.4.

The APD diameter is 200 μm , which, combined with a 100 mm lens, gives a 2 mrad FoV_i . This is in reality far too large compared to our expected beam divergence. Moreover, the bandwidth is also too wide. These two parameters were therefore not adapted in the first iteration of the platform, resulting in a large noise equivalent power (NEP) and degraded range performances.

Parameter	Value
Model	A-CUBE-I200-240 (LaserComponent)
Output	Analog
Size	41x41x40 mm
Weight	200 g
Consumption	7 W
APD diameter	200 μm
Gain	10
Bandwidth	240 MHz
Low-cut frequency	20 kHz
NEP (σ_n)	7.8 nW [from factory measures]
Analog output noise	11.9 mV
Analog output swing	2 V
Threshold at negligible FAR	$k=5$

Table 7.3: Characteristics of the APD of the BS platform.

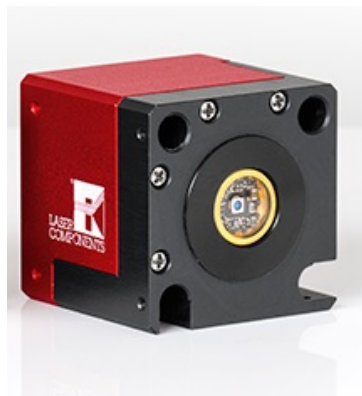


Figure 7.4: Picture of the A-CUBE APD.

Due to the lack of digital output, a supplementary device was necessary to perform threshold and to generate a digital output to the control system. We use the delay generator model DG645m. The threshold was put at $k=5$, which is much lower than for the APD of the platform PM. This is possibly due to the noise of the A-CUBE being TIA limited rather than limited by the dark current. The noise distribution is then closer to Gaussian, which allows for a better FAR at a lower threshold. Yet extensive measurements were not performed to confirm this hypothesis.

7.1.3.2 Platform "parabolic mirror"

Following this realization, we came across another APD, which was more in-line with the performance we needed. It is provided by the American company Voxel Opto. The detector includes the APD, the trans-impedance amplifier and a digital (0-1 V) output with an adjustable leading edge threshold. The developments of section 5.3 were made from this APD.

For this photo-detector, we performed measurement of the NEP, or σ_n , using developments made on chapter 5, and more precisely Eq. (5.30), which can be recalled here:

$$\sigma_n = \frac{P_{\text{mean}}}{\text{SNR}} \frac{1}{\tau_p f_l} \frac{D_r^2}{4R^2} \mathcal{R}_\pi \eta_r . \quad (7.5)$$

The detector was mounted and aligned in the system, operating outside with the same laser used in our system. The target used was a large, perfectly lambertian target of calibrated hemispherical reflectivity $\mathcal{R}_\pi=0.94$. The results are presented in Table 7.4.

R (m)	σ_n (nW)
121	0.42
100	0.38
71	0.41
54	0.44
34	0.44

Table 7.4: Measurements of σ_n from Eq. (5.30) for different ranges

The average value we get is $\sigma_n=0.42$ nW. Complete specifications are provided in Fig. 7.5

A considerable amount of data is provided by the supplier, which is very useful to understand the overall performance of the device. Some are shown in Fig. 7.5. First off, the bandwidth is not flat but is peaked between 0.8 and 15 MHz. According to the manufacturer, this is done to improve pulse detection. Nevertheless, the actual obtained bandwidth is rather short and may filter the highest frequency components of the pulse, especially at low PRF corresponding to sharp peaks, as shown in Fig. 7.2. This is visible in the second graph that is given in the datasheet, which shows the NEP as a function of the pulse width.

After correcting the curve using the value we measured of σ_n , we found the following fit:

$$\sigma_n = \frac{2.2 * 10^{-9}}{\tau_p^{3/4}} \text{ [W]} , \quad (7.6)$$

with τ_p in ns. From this equation, a 5 ns pulse must have 1.7 times more peak power to obtain the same sensitivity as a 10 ns pulse, which correspond to a 15% less pulse energy. In

Parameter	Value
Model	RUC1-KIAC (Voxtel)
Output	Analog and digital
Case size	Circular, 15x7 mm
Electronic interface size	75x50x5 mm
Consumption	5 W
APD diameter	75 μm , covered with a 500 μm half-ball lens
Gain	Up to 20
Excess noise factor F	5.6 at $G=20$
Bandwidth	Pulse optimized, 275 MHz
Low-cut frequency	5 kHz
NEP (σ_n)	0.42 nW for 10 ns pulse (measured)
Analog output noise	1 mV
Analog output swing	186 mV
Threshold at negligible FAR	$k=11$

Table 7.5: Characteristics of the APD of the PM platform.

summary, shortening the pulse will marginally decrease the pulse energy needed, thus marginally lowering average power and eye-safety issues.

The APD diameter is 75 μm , which is relatively small. Thankfully, there is an option to use an integrated half-ball lens directly soldered to the sensor. Supplier data show an effective collection diameter of 150 μm with this setup, provided that the f-number is higher than 4. With our 14 mm collection and a 100 mm focal, our f-number is 7.1, which is well within the specifications. The FoV_i can then be approximated at 1.5 mrad. One drawback is that the addition of the half-ball lens induces more complexity to model the size of the laser return spot on the APD surface. While the sensitivity of the detector is very high, this is counterbalanced by the necessity to use a high threshold ($k=11$ from Fig. 5.4) to reach a FAR low enough for our application. At last, it possess a digital output with embedded threshold for ease of integration with digital components.

7.1.4 Beam separator & collimation optics

As mentioned in section 4.3, the optical design was first developed with a beamsplitter to separate the emitted and received beam (platform BS), the second using a parabolic off-axis holed mirror (platform PM).

In our monostatic set-up, the cross-talk between the emission and the reception represents a challenge. At emission, the pulse peak power is at several kiloWatt, whereas the APD sensitivity is in the range of the nanoWatt. To prevent cross-talk, we would need an optical isolation of 120 dB. Such an isolation is far from easy to realize. On the literature, a 45 dB isolation using polarization-based separation is described as a best result in [McManamon 2015]. Cross-talk is caused by some degree of scattering on every optical surface the beam interacts with, even mirrors. In our architecture, the galvanometer mirror surfaces themselves produce enough backscattering to blind the APD for tens of ns after emission.

With this in mind, using an unpolarized BS is challenging because at emission, half the power

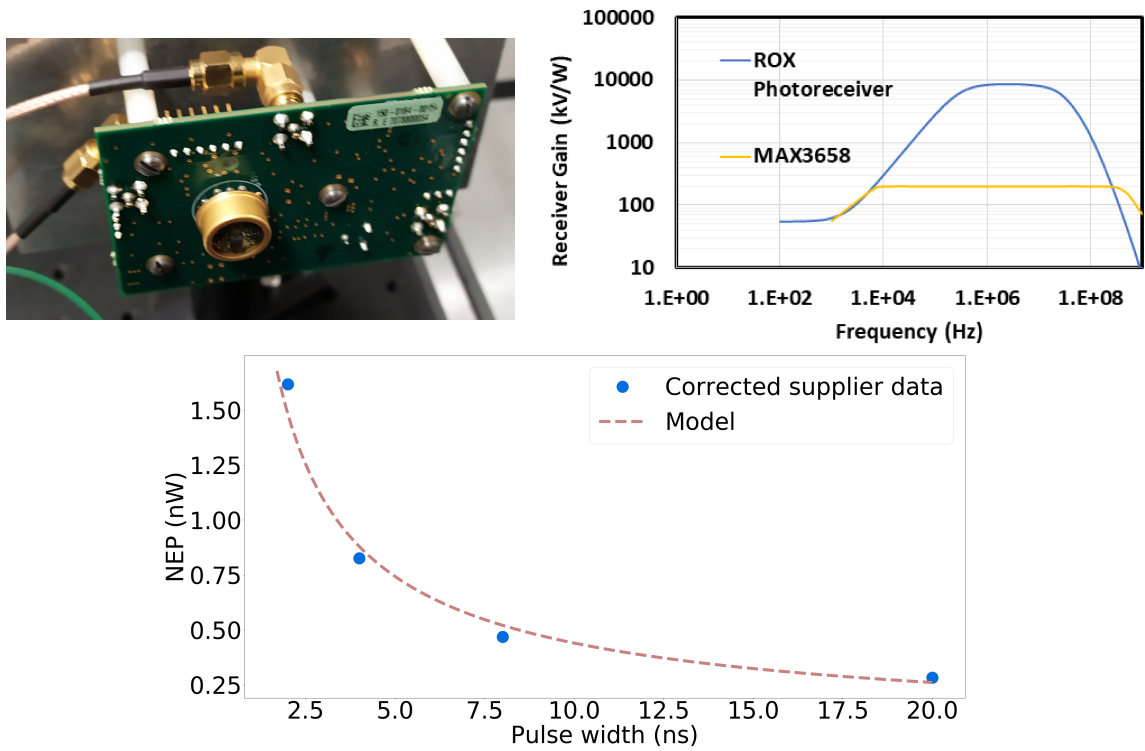


Figure 7.5: (Up, left) picture of the Voxel APD and its electronic card adapter. (Up, right) Bandwidth of the TIA compared with a classic commercial one [supplier data]. (Down) NEP as a function of the pulse width. The data comes from the supplier but were modified to fit the value of σ_n found with a 10 ns pulse. The fit is our addition.

must be discarded into a beam dump, leading to a heavy amount of backscattering. Our second architecture using a holed **PM** achieves less backscattering by reducing the amount of optical interfaces. Another solution could be to turn off the detector when the pulse is fired, but the time it takes for the **APD** to cycle is too long compared to the 1 km range wanted in our application.

7.1.4.1 Platform "beamsplitter"

This platform uses a beamsplitter to separate the emitted beam from the receiving one. We are using the beamsplitter plate BSW12R from the company Thorlabs, of dimensions 25x36x1 mm. At 1545 nm, transmission efficiency is $\eta_e^{BS}=54$ % and reflectance is $\eta_r^{BS}=46$ % [Thorlabs data]. This type of separation allows to have a beam waist almost as large as the system aperture D_r . To improve our link budget regarding the low **APD** sensitivity, we have to increase the energy density on the target, so we made the choice to use a $W_0=10$ mm beam diameter waist.

We use a triple lens collimator, model TC-18ACP1550, of 3.33 mm of beam waist diameter, coupled to a x3 beam expander, model GBE03-C. These two components were supplied from Thorlabs. The triple lens collimator provides very low wavefront error, resulting in a value of M^2 generally much lower than 1.05 [Thorlabs data].

7.1.4.2 Platform "parabolic mirror"

This platform uses a holed off-axis parabolic mirror to separate the emitted beam from the receiving one. The hole diameter D_h limits both the beam waist at emission, and the collection surface at reception. The transmission and reception coefficients are given by Eq. (4.5), which we recall here for simplicity:

$$\begin{cases} \eta_e^{PM} = 1 - \exp\left(-\frac{2D_h^2}{W_0^2}\right) \\ \eta_r^{PM} = 1 - \frac{D_h^2}{D_r^2} \end{cases} . \quad (7.7)$$

For component availability, we chose to keep the triplet lens collimator, model TC-18ACP1550, of beam waist diameter $W_0=3.33$ mm. The size of the hole was chosen at 5 mm to minimize transmission losses in reception. The transmission is then 99 % in emission and 87 % in reception. The **PM** is a custom piece from the supplier Thorlabs, adapted from an existing component. More details are given in Table 7.6. A picture is shown in Fig. 7.6.

Parameter	Value
Model	MPD249V5-M01
Dimensions	Circular, 63x50.8 mm
Aperture	>45 mm
Reflected focal lens	101.6 mm
Off-axis angle	90°
Coating	Protected gold, 96 % transmission at 1545 nm [Thorlabs data]
Surface quality	40-20 scratch dig

Table 7.6: Characteristics of the off-axis parabolic mirror.

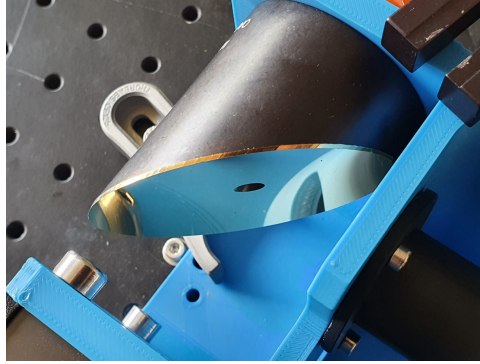


Figure 7.6: Picture of the off-axis parabolic mirror with a 5 mm through hole.

At last, we needed to be sure that the fixed focus triplet collimator specifications were correct and that the beam was well collimated. To do so, we used an InGaAs camera to image the beam on a portion of a plastic coating on a wall. The laser power, camera integration time and aperture were carefully chosen to have enough dynamic range for a reliable measure. 30 images were taken and averaged to reduce speckle noise, and then fitted with a 2D Gaussian, shown in Fig. 7.7. We obtained a beam diameter of 76.8 mm at 100 m, against 72.8 mm in theory (from Eq. (5.3) using $M^2=1.1$), knowing that the pixel resolution is 2.7 mm on our images. The fit is close enough to validate the theoretical value, even though more measurements at different range could be made to have a stronger confirmation.

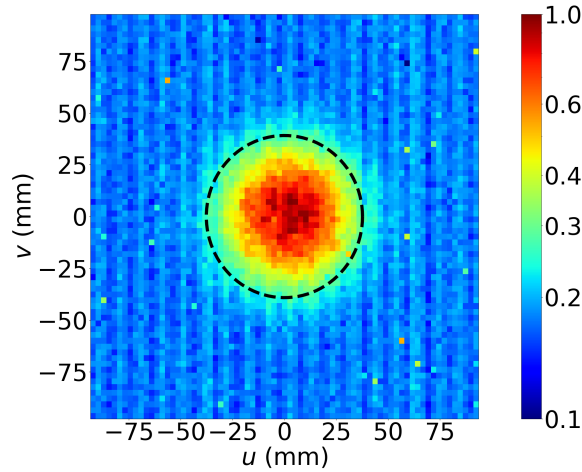


Figure 7.7: Average of 30 accumulated images of the fixed LiDAR beam from the triplet collimator at a 101.5 m range. The colorscale is logarithmic. The dotted ellipse represents the beam waist diameter at this range, 75.4 mm along u and 78.3 mm along v . Pixel resolution is 2.7 mm.

7.1.5 Bandpass filter & transmission coefficients

The last element in our system is the bandpass filter. It is used to block the background illumination coming from the sun, which impact the noise figure as shown on Eq. (5.26). The

bandwidth of the filter should be chosen so that the resulting background noise is negligible:

$$\sigma_{bg} < \sigma_n \iff \frac{2qFB}{\mathcal{R}_0} P_{pg} < \sigma_n^2. \quad (7.8)$$

If we use the expression of P_{bg} as a function of the bandfilter bandwidth Δ_λ from Eq. (5.27), we have (neglecting transmission efficiency) :

$$\Delta_\lambda < \frac{4}{\pi} \frac{1}{L_F D_r^2 \text{FoV}_i^2} \frac{\mathcal{R}_0}{2qFB} \sigma_n^2. \quad (7.9)$$

We have in our setup $D_r=14$ mm, $\text{FoV}_i=1.5$ mrad, \mathcal{R}_0 , $F=5.6$, $B=275$ MHz and $\sigma_n=0.42$ nW. The missing value is L_F , which is the background radiance. [Bell *et al.* 1960] give orders of magnitude of sky radiance in the infrared region. Near 1 μm , the radiance of a brightly sunlit cloud was measured at around 0.1 $\text{W.m}^{-2}.\text{sr}^{-1}.\text{nm}^{-1}$. We obtain $\Delta_\lambda < 11$ nm. This value is relatively large, even on this worst case scenario. This is largely due to the small instantaneous FoV of the sensor, and the small aperture.

We used a hard coating filter from Thorlabs, model FBH1550-12. This filter has a full width at half maximum (FWHM) of 12 nm, centered on 1550 nm, and an excellent transmission of more than 95 %, while having a 10^{-5} transmission in the blocking region. In the case of the PM architecture, we had to place the filter within the focus of the received beam. This means that the angle of incidence is not the same for all the rays within the beam. The bandpass filter we use is based on a dielectric-stack Fabry-Pérot interferometer design, meaning that it relies on optical path difference between rays to constructively interfere at the wanted wavelength, and reject all the others. Angle of incidence will therefore impact the filter characteristics, as it changes each ray optical path length. An equation giving the dependency of the center wavelength λ_i on the angle of incidence i can be found from geometrical consideration [Baumeister 2004]:

$$\lambda_i = \lambda_0 \sqrt{1 - \frac{\sin(i)^2}{n_*^2}}, \quad (7.10)$$

with λ_0 the center wavelength at normal incidence and n_* the effective coating stack refractive index. Measurement of the filter were performed for different angle of incidence, and a good fit was found for $n_*=1.83$ (see Fig. 7.9). Transmission efficiency and overall bandpass shape stays the same up to 10° of incidence, but starts to drop after. It is very well modeled by a supergaussian of order p of expression:

$$\eta(\lambda, \lambda_i) = \eta_0 \exp \left(- \left(\frac{2(\lambda - \lambda_i)^2}{\sigma_\lambda^2} \right)^p \right), \quad (7.11)$$

with η_0 the peak transmission and σ_λ the transmission window diameter. The data and corresponding models are represented in Fig. 7.8. Experimental fit for these parameters are shown in Table 7.7.

For a filter placed on the focus side of a lens or parabolic mirror of focal fo , and system aperture D_r , the transmission can be found by integrating the previous equation for angle of incidence between 0 and $\tan(D_r/2fo)$ over the circular surface:

Angle of incidence	0°	5°	10°	20°	30°
λ_i (nm)	1550.0	1548.6	1543	1523.4	1490.5
σ_λ (nm)	9.78	9.80	10.0	11.2	13.4
η_{a0}	0.989	0.986	0.978	0.913	0.786
p	1.83	1.79	1.50	1.10	1.08

Table 7.7: Parameter fit for the bandpass filter transmission curve as a function of angle of incidence.

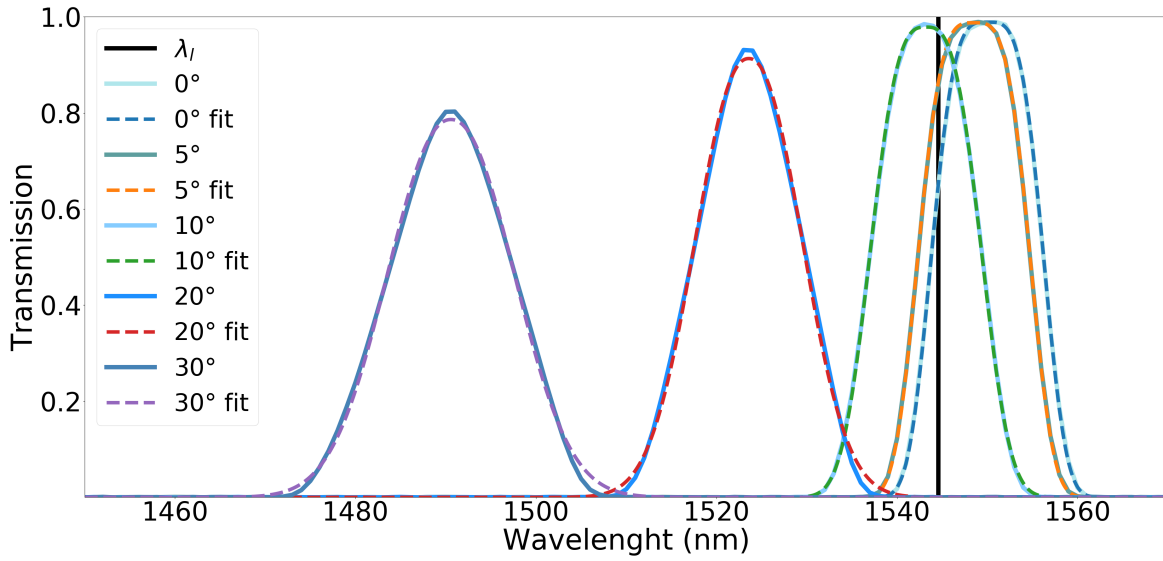


Figure 7.8: Experimental values of the transmission of the bandpass filter as a function of wavelength for several angle of incidence (full lines). The black line shows the laser wavelength, and the dotted line are the supergaussian fit from Eq. (7.11).

$$\begin{aligned}
\eta^{BP}(\lambda) &= \frac{4f^2}{\pi D_r^2} \int_0^{2\pi \tan(D_r/2fo)} \int_0^{\tan(D_r/2fo)} \eta(\lambda, \lambda_0 \sqrt{1 - \sin(i)^2/n_*^2}) \, ididj \\
&= \frac{8f^2}{D_r^2} \int_0^{\tan(D_r/2fo)} \eta_0(i) \exp \left(- \left(\frac{2(\lambda - \lambda_0 \sqrt{1 - \sin(i)^2/n_*^2})}{\sigma_\lambda(i)} \right)^{2p(i)} \right) \, idi
\end{aligned} \tag{7.12}$$

with λ our laser wavelength. This equation does not have a closed form, but can be numerically solved. A representation of the bandpass transmission coefficient as a function of the incident angle is made in Fig. 7.9 for $\lambda=1544.4$ nm. Calculated transmission is found to be $\eta^{BP}=0.72$. This value is relatively low, and clearly not optimized. If the filter was tilted at 7.9° along one direction, then transmission would have been 0.96. This is an oversight and will be corrected in future versions of the LiDAR.

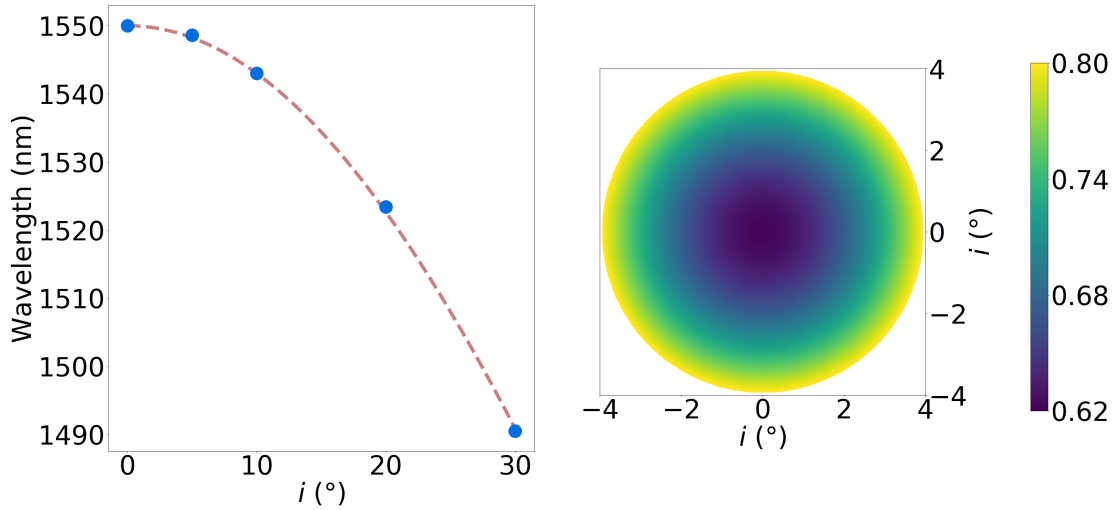


Figure 7.9: (Left) experimental data and fit (from Eq. (7.10)) of the center wavelength shift as a function of the angle of incidence i . (Right) transmission at $\lambda=1544.4$ nm through the bandpass filter for a focal cone of maximal angle $\tan(D_r/2fo)$.

For the platform PM, emission and reception transmission coefficients are given by the following calculation:

$$\begin{cases} \eta_e = \eta_e^{PM} \eta_g^2 = 0.95 \\ \eta_r = \eta_g^2 \eta_r^{PM} \eta^{BP} = 0.58 \end{cases} \tag{7.13}$$

For the platform BS, emission and reception transmission coefficients are given by the following calculation:

$$\begin{cases} \eta_e = \eta_e^{BS} \eta_g^2 = 0.52 \\ \eta_r = \eta_g^2 \eta_r^{BS} \eta^{BP} = 0.32 \end{cases} \tag{7.14}$$

The global transmission is 3.3 times better with the **PM** architecture than with the **BS** platform.

7.2 System overview and control electronics

Now that we have defined the performance of each component of the optical architecture, we can describe the control electronics used. It is equivalent for both platform, except that the **BS** platform have a pulse generator (model DG645m) to trigger on the A-CUBE analog output and generate a proper digital signal for the control electronics.

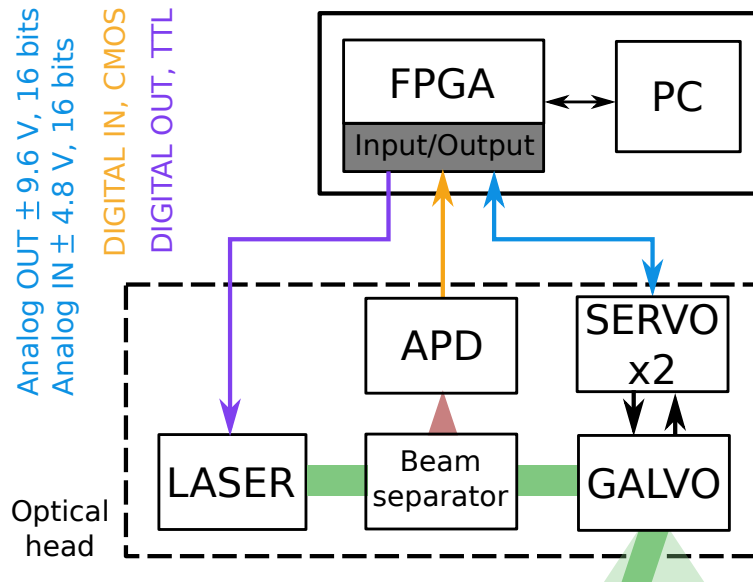


Figure 7.10: Schematic of the system. The control unit is made of a real-time loop implemented on a **FPGA**, with both analog and digital input and outputs. The **APD** is saturated by cross-talk during pulse emission.

A schematic of the complete system is done in Fig. 7.10. Due to the high refresh rate requirement, the system operate in real-time on a **FPGA**. This component is a programmable array of logic elements in which each section execute its own code. This way, a **FPGA** truly support parallel execution with very fast and accurate loop cycles. The downside is the heavy compilation time (more than 20 minutes for large codes), the low-level programming language and the size of the executable code that can be programmed into the device.

Our **FPGA** was supplied by National Instruments and coded in Labview FPGA, which is fast to learn, structure and modify, which made it really useful for prototyping. Its base loop rate is 40 MHz, but can be increased several times for specific loops if the numbers of operations is low enough to be executed within that type frame. We chose to directly connect the output of the **APD** to a digital input of the **FPGA**. The timestamp was therefore made using the **FPGA** clock, which was increased at 240 MHz in the specific loop. Pipelining with shift register was used to reach this high-rate clock by reducing the number of operations needed within a single clock cycle, at the expense of a higher delay. We obtained a 62.5 cm range resolution. The **FPGA** also

presented analog input and output ports, which are used to drive the dual axis galvanometer. The full specifications can be found in Table 7.8.

Parameter	Value
FPGA card	NI 7847R
Host Computer	PXIe-8133
Chassis	PXIe-1075
FPGA Chip	Kintex-7 160T
Programming language	LabView FPGA, LabView
Clock	40 MHz, can be derived
Digital I/O	48 channels, TTL, LVTTTL or LVCMOS compatible, clock dependent frequency
Analog input	8 channels, ± 1 V, ± 2 V, ± 5 V or ± 10 V, 16 bits, > 1 G Ω impedance, 0.5 MSa/s per channel, ~ 2 mV calibrated accuracy at full scale, ~ 0.2 mV noise
Analog ouput	8 channels, ± 10 V, 16 bits, 0.5 Ω impedance, 1 M/s per channel, 2.5 mV calibrated accuracy at full scale

Table 7.8: Characteristics of the **FPGA** and control electronics.

As seen on this table, the **FPGA** has the correct analog I/O to drive the galvanometer mirror, ie ± 10 V for command and ± 5 V for position reading, with the adequate 16 bits resolution. The digital I/O is also compatible with the TTL levels required for triggering the laser, and the LVCMOS level for reading the **APD** digital output. Oscilloscope measurements of the waveforms are shown in Fig. 7.11, with a target located at 343 m. There is a 200 ns delay between the electrical TTL trigger and the laser optical pulse. As we can see, the **APD** is saturated by the initial cross-talk, creating a blind zone which can extend up to 30 m at full laser power. The analog output is far too fast to be sampled by the analog input of our **FPGA**, therefore we cannot have access to the target reflectivity. A workaround using peak hold electronics was used to "slow down" the pulse in imagery mode (see the next chapter).

Developments of the LabView FPGA code took several months, spanned on more than a year, with occasional improvements. Low level developments included several signal generator functions for the various patterns used (raster-scan, spirals, Lissajous, circle-spiral, ...), synchronization between loops (laser trigger, **APD** read, signal generation) and transitions between modes, data exchange between the host and the target using buffering first in, first out (**FIFO**). Custom cables were also designed by the candidate between the **FPGA** electric terminals and the electro-optical components. A picture of the system at a early state of development is shown in Fig. 7.12. Close-up of the **BS** and **PM** platform are shown on the same figure.

The platform is put on a 2-axis rotational mount. Several additional sensors are usually used during alignment and operation, including a high-bandwidth oscilloscope, a **VIS** and **SWIR** camera with a long-focal objective and a voltmeter. The platform faced a restricted access square field of dimensions of around 120x120 m. The field is clearly not long enough for long range tests, but several elements at a longer range (buildings, trees, ...) were present. For drone tracking, specific trial sessions were organized and are described in the next chapter.

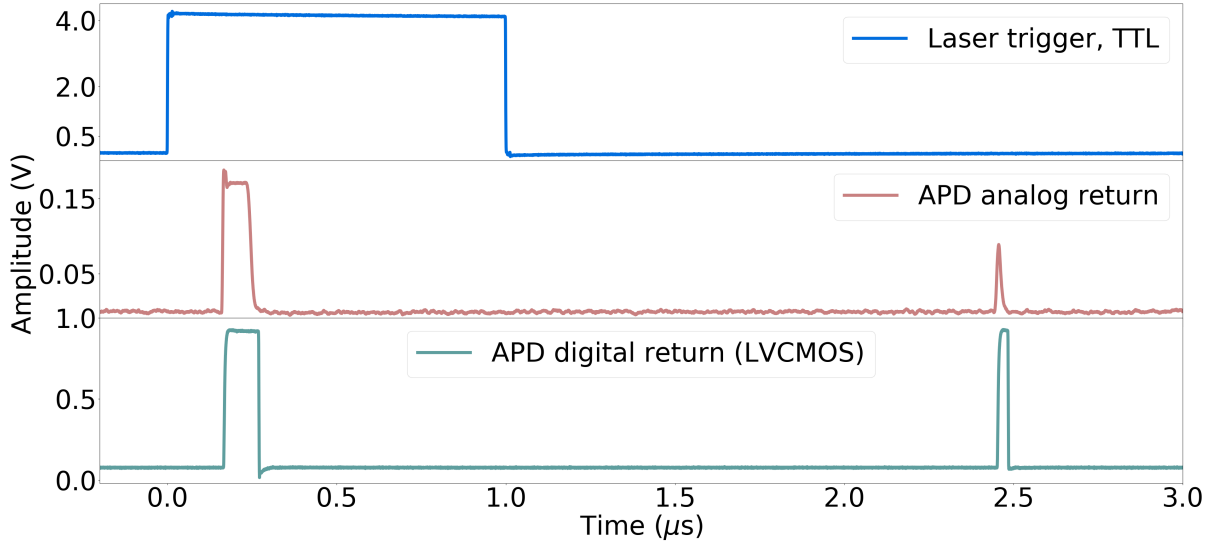


Figure 7.11: Laser trigger, APD analog and digital returns of our LiDAR system pointing at a target 343 m away.

7.3 Platform integration

After a series of test and validation steps (results shown in the next chapter), the platform was ready to be integrated. This step is a pre-integration of the product, which is at the demonstrator maturity level, and consists of the realization of a case as well as an independent FPGA card for control. A RS-422 communication interface between the FPGA and a host system was also developed for bi-directional data exchange. This way, we made sure that every LiDAR mode was fully configurable. We made the choice to have two components: one optical head, and one rack apparatus containing both the power supplies and the FPGA. A series of cables of 4 m length connects the two systems, transporting both analog and digital signals. Therefore, special care was taken against cross-talk (via shielding) and voltage drops.

Mechanical design and electrical connections were realized according to the candidate plans. Mechanical design was heavily expanded into a full 3D computed aided design (CAD). These two tasks were handled by internal offices within the company. A short thermal study was also performed to make sure that the system won't overheat confronted to high summer temperatures. An engineer, supervised by the candidate, was recruited to develop and test the RS-422 bi-lateral communication. Realization of the FPGA card and electronic interface (analog I/O with correct signal levels) was done under the constant supervision of the candidate. Complete specifications and documentations were produced regarding the core programming as well as the electronic interfaces and RS-422 protocol. The integration took around 10 months to complete and test. The resulting product is shown in Fig. 7.13.

Of the components presented previously, the FPGA card and the electronic interface is the only one that was changed for integrability. Analog input and output noises were characterized at respectively 0.27 mV RMS and 0.43 mV RMS (using a 20 MHz bandwidth oscilloscope). The bandwidth of the galvanometer being limited to a few kHz at best, it is likely that the actual

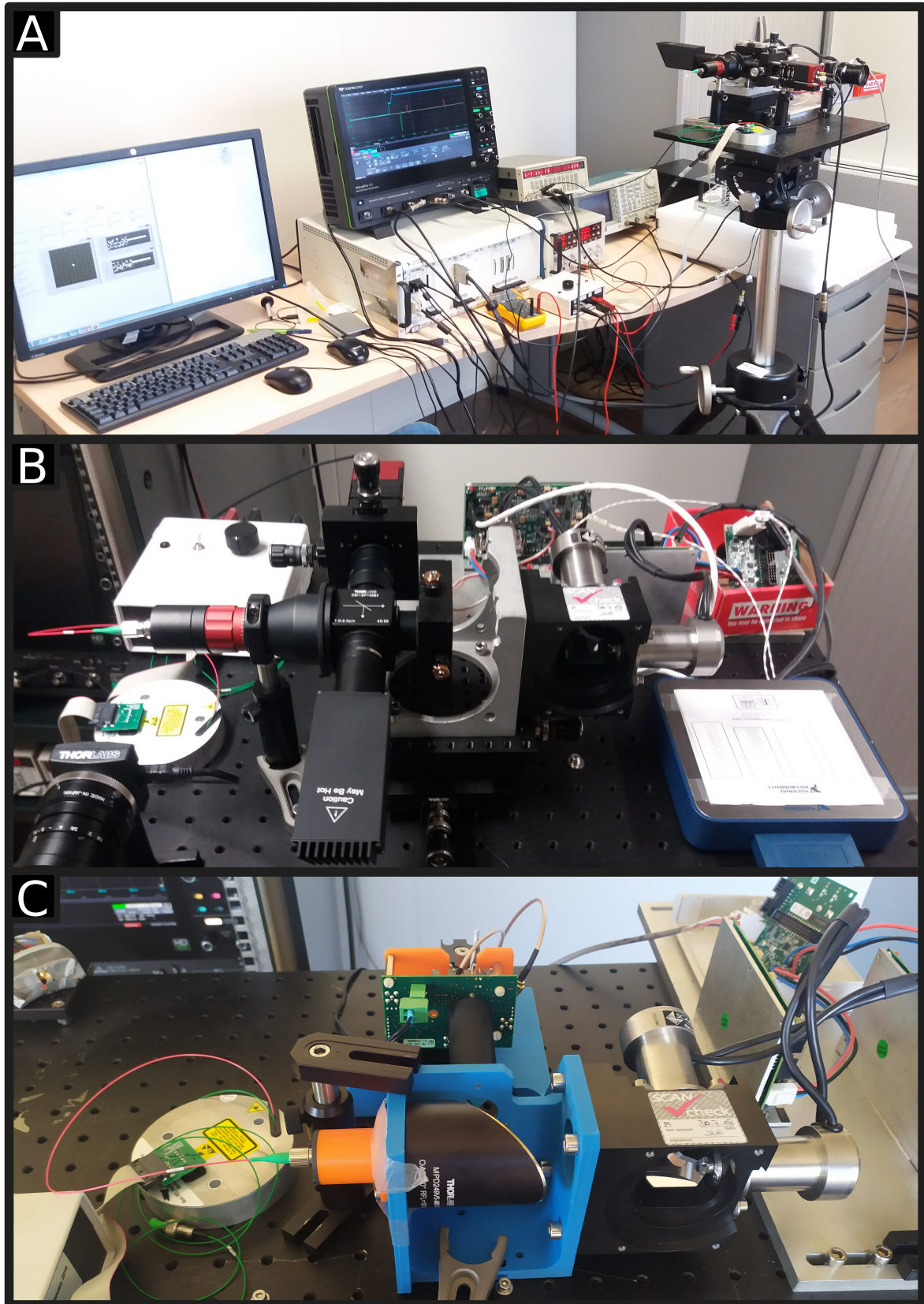


Figure 7.12: (A) Global overview of the platform BS in a early stage of development. (B) Close-up of the BS platform with Thorlabs mechanical assembly. (C) Close-up of the PM platform using a custom 3D-print mechanical mount.

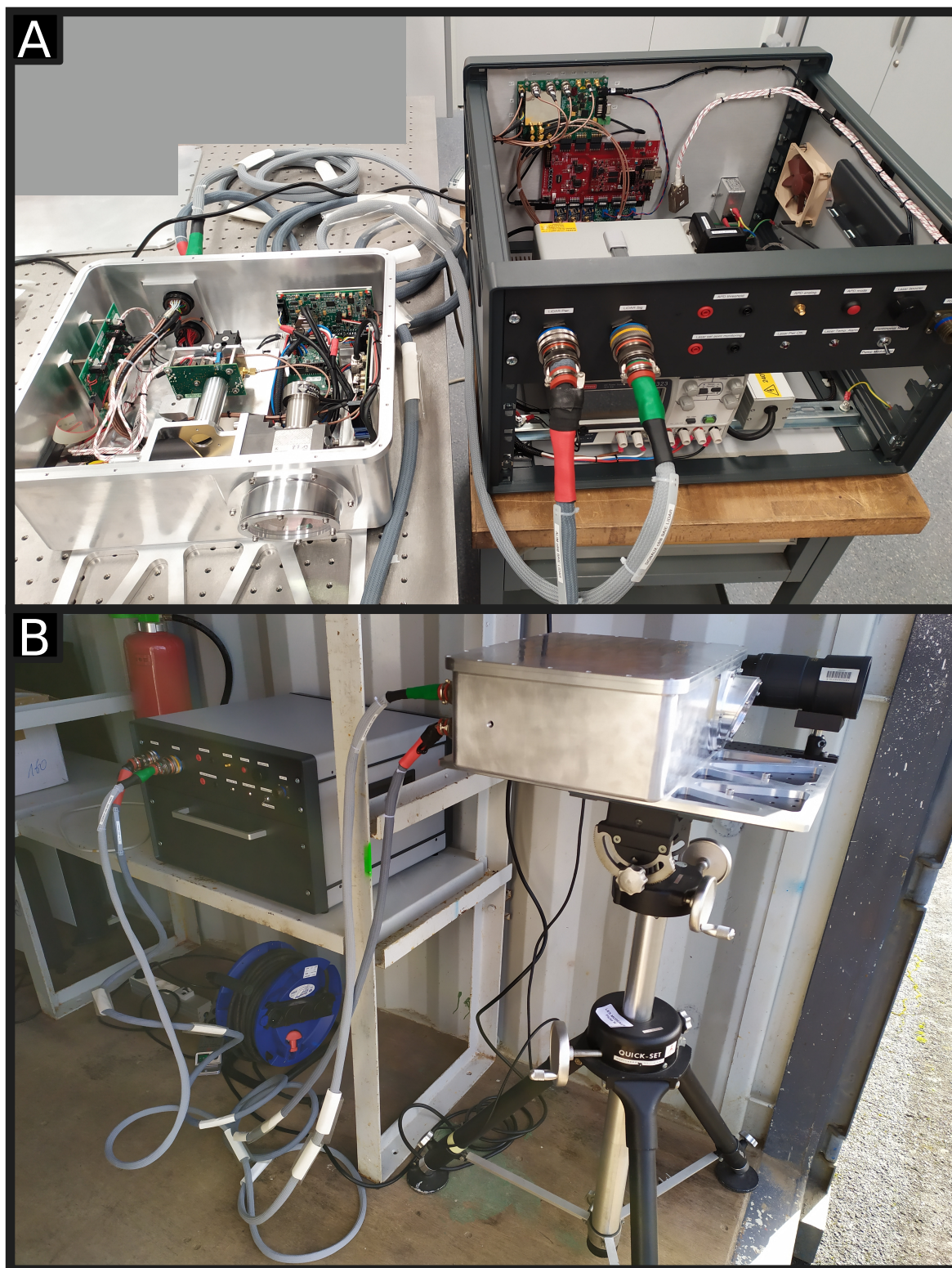


Figure 7.13: (A) Integrated LiDAR optical head and rack with their covers off. The FPGA card is located in the rack, with the power supplies. (B) Closed system, ready to operate next to a long focal SWIR camera.

resulting mechanical noise is much lower. Still, if we use these values we can obtain the global pointing **RMS** noise Δ_p :

$$\Delta_p = \sqrt{(10 \mu\text{rad})^2 + (0.43 \text{ mV} * 42.5 \text{ mrad/V})^2 + (0.27 \text{ mV} * 85 \text{ mrad/V})^2} = 30 \mu\text{rad}. \quad (7.15)$$

This value does not take into account the accuracy of the analog input or output, nor the mechanical accuracy of the galvanometer axis positioning. Nevertheless, it gives an indication of the pointing stability and readout position in the center of the field ($\theta=0^\circ$, $\varphi=0^\circ$). This value is still very acceptable, corresponding to 3 cm at 1 km.

7.4 Conclusion

In this chapter, we presented each individual components of our platform. We detailed their characteristics, often using complementary measurements if data provided by the suppliers were incomplete. The laser source was characterized in mean and peak power, pulse shape and divergence. The bode diagram of the galvanometer (for beam steering) was measured, from which a frequency limit regarding the amplitude was extracted. The **APD** sensitivity, **FAR** and probability of detection was quantified, as well as its behavior with pulse width. The filter transmission was measured and modeled for diverse angle of incidence, from which we could deduce the global transmission of the system.

Finally, the overall platforms were shown in various pictures, with details regarding the real-time control electronics based on a **FPGA**. Significant efforts were put into these platforms and their development, leading to an integration process supervised by the candidate. Global system configuration and performance are described on the next chapter.

Experimental results

Contents

8.1	Laser safety for field trials	101
8.2	Frequency limitations	102
8.2.1	Raster-scan for detection mode	103
8.2.2	Circle-spiral for detection mode	103
8.2.3	Lissajous for tracking mode	104
8.2.4	CLV spiral for tracking mode	104
8.3	Trials and results	105
8.3.1	03/2019 with the platform "beamsplitter"	108
8.3.2	02/2020 with the platform "parabolic mirror"	108
8.4	Imagery mode	117
8.4.1	3D point clouds	117
8.4.2	4D point clouds with signal intensity	117
8.5	Conclusion	119

In this chapter we present the experimental results of the [LiDAR](#). Our focus is toward the tracking data, which we have accumulated during our trials against drones. But beforehand, we have to address both the laser safety and the scanner frequency limitations so as to define operational limits in which our system must operate.

8.1 Laser safety for field trials

The first element to consider when testing a [LiDAR](#) system is the laser safety. To quantify laser hazard to exposed personals, we have to refer to laser safety norms. International laser safety standard EN 60825-1:2007 defines a maximal permitted exposure ([MPE](#)) of the eye in $[J/m^2 \text{ or } W/m^2]$ for each wavelength and observation time. Two limiting regimes must be studied, either using a single pulse or continuous exposure ($> 10 \text{ s}$).

The [MPE](#) for a single impulsion of 10 ns , noted MPE_s , is 10^4 J/m^2 at 1544.3 nm . For continuous exposure or pulse accumulation ($> 10 \text{ s}$), we use the notation MPE_c , and its value is 1000 W/m^2 . At this wavelength, the [MPE](#) is identical for the skin and for the eyes, because light is mainly absorbed by the cornea and does not reach the retina. The effect is purely thermal. Quantification of eye-safety limits can be done by computing nominal hazard zone ([NHZ](#)), within which safe exposure levels may be exceed. In this zone, restrictive measures and protective wear should be used. [NHZ](#) is given by the following formula, modified to use $1/e^2$ laser characteristics instead of the $1/e$ defined in the norm:

$$\begin{cases} \text{NHZ}_s = \frac{\sqrt{\frac{8P_{\text{mean}}\eta_e}{\pi\text{MPE}_s f_l} - W_0^2}}{\Theta_b} \\ \text{NHZ}_c = \frac{\sqrt{\frac{8P_{\text{mean}}\eta_e}{\pi\text{MPE}_c} - W_0^2}}{\Theta_b} \end{cases} \quad (8.1)$$

The parameters and computations are shown for both the platform **BS** and **PM** in Table 8.1. It can be noted that the **PRF** is kept quite low at a few tens of kHz, compared to what is possible with this type of fiber laser. This is done to increase the maximal range of the system, at the expense of the scanning rate, link to the **PRF**.

Parameter	Platform BS	Platform PM
Mean power P_{mean}	1.25 W	1.25 W
Pulse width τ_p	9.7 ns	9.7 ns
PRF f_l	20 kHz	30 kHz
Emission transmission coefficient η_e	0.52	0.95
Waist diameter W_0	10 mm	3.33 mm
Full angle divergence Θ_b	220 μrad	710 μrad
NHZ_s	eye safe for 1 pulse	eye safe for 1 pulse
NHZ_c	182 m	77 m

Table 8.1: Laser safety calculations.

As we can see, the system presents a level of hazard for skin and eyes up to non-negligible ranges. One way to reduce the hazard is to reduce the laser power, at the expense of a reduced performance. During trials, specific restrictions and adapted personal protective equipment (**PPE**) were adopted to manage the risk. It is also interesting to note that, even though almost twice as much energy is emitted with the **PM** platform compared to the **BS**, the difference in divergence is enough to obtain more than twice the **NHZ**.

Finally, it should be noted that these values are given for a constant, static exposure of at least 10 s, which is very conservative in terms of safety. Our **LiDAR** being a scanning system, such a case is never realized in practice. Further developments should be made to more accurately represent the laser hazard of such a system in its various modes, each of them including a scanning pattern.

8.2 Frequency limitations

We can use here the developments that were made on chapter 6 regarding the frequency limitation. We can summarize the results in Table 8.2.

Now we have to compute the values of the frequency for each mode and each pattern to see if we are within one of the limitations described in this table. For the light round-trip, for the platform **PM**, we have $\text{FoV}_i = 1.5 \text{ mrad}$ and $\Theta_b = 710 \mu\text{rad}$. We can also use the farthest range

Name	Reference	Limitation on f_p
Light round-trip f_c^{rt}	Eq. (6.38)	$\frac{c}{2R} \left(\frac{\text{FoV}_i - \Theta_b/2}{2A_p} \right)$
Circle-spiral (pure sinus) f_c	Eq. (6.39)	$\left(\frac{a}{A_p} \right)^b$
Lissajous f_c^{liss}	Eq. (6.40)	$\left(\frac{a}{A_p} \right)^b \frac{n}{n+1}$
Triangular raster-scan f_c^{tri}	Eq. (6.43)	$\left(\frac{a}{A_p} \right)^b \frac{m^{2b-1}}{\gamma}$
Spirals f_c^{spi}	Eq. (6.47)	$\left(\frac{a}{A_p} \right)^b m^{(\alpha b + \beta - 1)/\alpha}$

Table 8.2: Frequency limitations for the LiDAR system.

$R=1$ km. For the galvanometer limitations, we can also remind here that $a_{fc}=34390$ rad.s $^{-1/b_{fc}}$ and $b_{fc}=0.45$.

8.2.1 Raster-scan for detection mode

The frequency limitation as a function of the wanted amplitude for the raster-scan is shown in Table 8.3. We use the cutoff $m=9$, which corresponds to the 5th odd harmonics. We also use $\gamma=3/2$ as described in the chapter 6.

Triangle peak-to-peak amplitude A_θ (or A_p) ($^\circ$)	Maximal allowed frequency f_c^{tri} (Hz)	Maximal allowed round-trip frequency f_c^{rt} (Hz)
2	266	2460
4	195	1230
6	162	820
8	142	615
10	129	492

Table 8.3: Triangle waveform frequency limitations for raster-scan.

In any case, the scanner bandwidth imposes stronger limitations than the round-trip light travel. This is true for any pattern, and as such we will not display it in the next tables. As we will see in the experiment, we always choose frequency values far lower than the scanner limitations, because the wanted resolution is constrained by the laser repetition rate, which is fairly low at 30 kHz.

8.2.2 Circle-spiral for detection mode

In this mode, we will neglect the spiral, which is operated at the same frequency f_i as the circle but at a lower amplitude. The circle is created by driving each axis using a sinus, meaning that we can directly use Eq. (6.39). One has to keep in mind that the actual frequency for the circle depends on the intruder, its speed, and the range at which it should be detected, as well as the LiDAR parameters. These results are presented in the next chapter. Here we simply wish to give the maximal permitted frequency f_i at a given circle diameter A_s . The results are shown in Table 8.4.

Circle optical diameter A_p or A_s ($^\circ$)	Maximal allowed frequency for f_p (or f_i) using the expression of f_c (Hz)
2	500
4	360
6	300
8	265
10	240

Table 8.4: Circle-spiral frequency limitations.

8.2.3 Lissajous for tracking mode

In tracking mode, the frequency limitation is directly linked to the localization rate f_{loc} , which is linked to the pattern period by $T_p = n/f_p$. Here, the most constraining frequency limit is achieved at close distance, when the pattern has the maximal peak-to-peak amplitude. We choose $A_p = 0.5^\circ$ (90 cm at 100 meter distance). This correspond to 3 times a 30 cm drone at 100 meters. If the drone goes at a higher range, then the angular amplitude is going to get smaller. We can find the frequency limitation as a function of the pattern parameter n , shown in Table 8.5.

Shape parameter n	Maximal allowed frequency for f_p using the expression of f_c^{liss} (Hz)	Maximal allowed localization rate $f_{loc} = f_p/n$ (Hz)
2	620	310
3	696	230
4	743	185
5	774	155
6	796	132

Table 8.5: Localization frequency limitation as a function of the shape parameter for a Lissajous.

8.2.4 CLV spiral for tracking mode

In the case of the CLV spiral, which was found on section 6.3 to be the pattern providing the highest beam density, we have $\alpha = \beta = 1/2$. We use the same maximal amplitude $A_p = 0.5^\circ$. In this case, the maximal allowed frequency for f_p using the expression of f_c^{spi} gives 434 Hz with $m=4$ (only 1/4 of the spiral in the center should be deformed). We show in Table 8.6 the corresponding maximal localization rate f_{loc} as a function of the CLV shape parameter n , which is half the number of spires in this case.

It is interesting to note that CLV spirals of the same shape parameter are at best 1.5 times slower than their Lissajous counterpart. In practice, this may create a limitation depending on the wanted localization rate. Nevertheless, a too high frequency can be detrimental if the laser PRF is not high enough to get a sufficient number of beams per period (to keep a high beam density on the pattern).

Shape parameter n	Maximal allowed localization rate $f_{loc}=f_p/n$ (Hz)
2	217
3	145
4	108
5	87
6	72

Table 8.6: Localization frequency limitation as a function of the shape parameter for a CLV spiral.

8.3 Trials and results

We used several locations for platforms developments and trials. We have a optic lab, whose range is limited to 10 meters, which was used for very early tests. Then, we moved to a 120x120 m open field, with restricted access. Laser power was tuned to reduce the [NHZ](#) within this boundary if it was needed. The platform was kept inside an small building, and could be used at any time, which greatly facilitated developments. It is shown in Fig. 8.1.

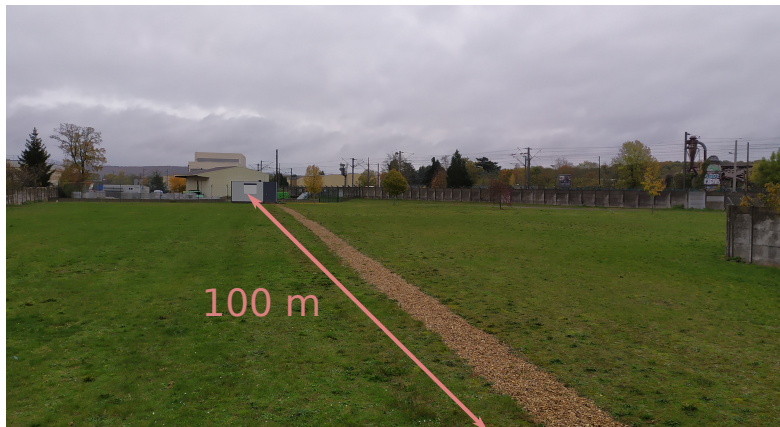


Figure 8.1: Open field used for medium range (100 m) tests and developments.

For long range, we had to organize specific trials with drone pilots in accordance to the regulation of the country. We did two sets of trials, 2 weeks in March 2019 with the platform [BS](#) and 1 week in February 2020 with the platform [PM](#). Each trials required a fair amount of organization for approval, logistic and drone flight preparation. Both trials were done at the same location, which offered an open field of around 1.7x2 km in surface, with the ability to fly different kind of drones. Pictures of the field and the [LiDAR](#) installations are shown in Fig. 8.2. Three types of drones were tested, their characteristics are described in Table 8.7.

These drones present rather different shapes and types of trajectories. Fixed wings have higher maximal speed, but lower accelerations and more curved trajectories compared to their rotary equivalent. They also present significant cross-section variations depending on their orientation. The twinstar for instance is much more difficult to detect when coming from the front (thin nose and wings) than from its profile or when turning. This was highlighted in some of our



Figure 8.2: (Left) picture of the modular container in which was operated the [LiDAR](#). (Right) picture of the open field in which the drones flew.




	Phantom4 (DJI)	Twinstar RD RR (Multiplex)	Black Widow (Vulcan UAV)
			
Wing type	Rotary	Fixed	Rotary
Dimensions	35 cm diagonal	110 cm length, 140 cm wingspan	45x40x30 cm
Weight	1.4 kg	1.4 kg	3 kg
Maximal speed	20 m/s	-	-

Table 8.7: Description and pictures of the drones used during trials.

collected data.

During these trials, our priority went toward the detection and tracking mode. Intrusion mode was tested as a proof of concept at very close range, but we could not operate two drones simultaneously to get telemetry in the center and intrusion on the perimeter. Overall, we had to process tracking data to gather experimental information on the system performance. To this effect, during tracking we monitored:

- angular position (θ, φ) and range R of the drone,
- the number of echoes per period N_p ,
- the frequency localization f_{loc} , which is the rate at which localization data are available. For this value, we consider discrete time bins delimited by each pattern period T_p . During each time bin, the average angular position (θ, φ) and range R is computed from the temporal positions of the echoes in the pattern. This average is temporally assumed to be at the middle of this time bin. f_{loc} is then defined as the inverse of the time between consecutive time bins presenting at least one echo. Therefore, if there is at least one echo per period ($N_p \geq 1$), then the localization frequency is at its nominal value, which is defined by $1/T_p$. Then, if there is at least one echo on one defined period, succeeded by x periods without an echo, and at the period $x+1$ there is at least an echo, the resulting f_{loc} is equal to $1/((x+1)T_p)$. f_{loc} is therefore a discrete function.

These last two parameters are very important indicators of tracking quality. A high number of echoes means a strong average localization and a high pointing stability. Drops in frequency localization give a good indication of the range limit of the system, or at least the range at which tracking quality starts to seriously degrade. The evolution of N_p with the distance is also directly linked to the probability of detection, and can be used to fit a number of parameters in the models described in the previous chapters. Detection data (during raster-scan) could not provide enough info because, as described in chapter 4, the transition between detection and tracking mode is automatic upon a single echo. To gather more data using this mode, an imagery mode was developed (see next section), but unfortunately could not be tested with drones.

During trials, our LiDAR system was mounted on a tripod and oriented toward the open field, as shown on Fig 8.2. As it will become apparent in the figures, during tracking some data were periodically lost because of an error in the size of the buffer between the host collecting the data and the FPGA. Yet, if some holes in the trajectories can be visible due this buffer issue, tracking was fully active during that time period.

The purpose of these trials was to characterize the system on three main aspects: maximal range, tracking speed and pointing accuracy. To achieve this, drone trajectories were separated into two kinds. The first is named "distancing" or "approach": the drone is hooked at short/long range, and get away/close from/to the system while minimizing its displacement in azimuth or altitude. This trajectory is used to find the maximal range at which the drone can be tracked. The second is named "left-right": at a fixed, or almost fixed range, the drone alternate acceleration and deceleration to reach maximal speed in azimuth. This trajectory is used to confirm that tracking is robust to high speed and acceleration.

8.3.1 03/2019 with the platform "beamsplitter"

With this platform, we had to use the lower laser PRF usable (20 kHz) to maximize the range. During these trials, the spiral was not implemented, and so only the Lissajous was tested. We used a $n=3$ Lissajous, with $f_{loc}=120$ Hz, relatively far from the maximum values shown in Table 8.5. This way, the number of beams per pattern period during tracking is 167. The localization rate was set at a relatively low value, but it was the first trials so we took a margin.

For the detection mode, the value of the angular resolution δ_θ and δ_φ , as well as the FoV (A_θ, A_φ) were often changed to reduce the scanning time T_{scan} so as to increase the probability to detect the target.

The LiDAR parameters used during these trials are shown in Table 8.8.

Parameter	Value
P_e	5 kW
f_l	20 kHz
Θ_b	220 μ rad
D_r	14 mm
σ_n	7.8 nW
k	5
η_e	0.52
η_r	0.32
Tracking pattern	Lissajous
n	2
f_p	360 Hz
f_{loc}	120 Hz
A_p	0.3° at 100 m

Table 8.8: LiDAR parameters used during the second trials.

The resulting data from the tracking of a phantom4, a twinstar and a black widow are shown in Fig. 8.3, 8.5 and 8.4. The black dot at position (0,0,0) represents the LiDAR position.

On these figures, we can see that the number of echoes per period N_p and the localization frequency f_{loc} add important information. N_p clearly decreases with range, and there is a range limit at which f_{loc} starts to decrease as well. We can see in Fig. 8.6 that, when combining all these trajectories, f_{loc} drops to 60 Hz or less only when there is less than 7 echoes per period. Keeping a higher number of echoes per period at a higher range may be possible, but it should be kept in mind that the fundamental range limit of the link budget remains.

Finally, rough range limits for each drone is reported in Table 8.9. As seen on this table, we are relatively far from the 1 km on the specification Table. Improved performance are presented on the next subsection with the PM architecture. The data registered during trials are used on the next section to characterize the probability of detection for each drone.

8.3.2 02/2020 with the platform "parabolic mirror"

During these trials, we had a more advanced FPGA code, with the CLV spiral implemented, as well as more robust knowledge of the system in general. For detection mode, the value of the

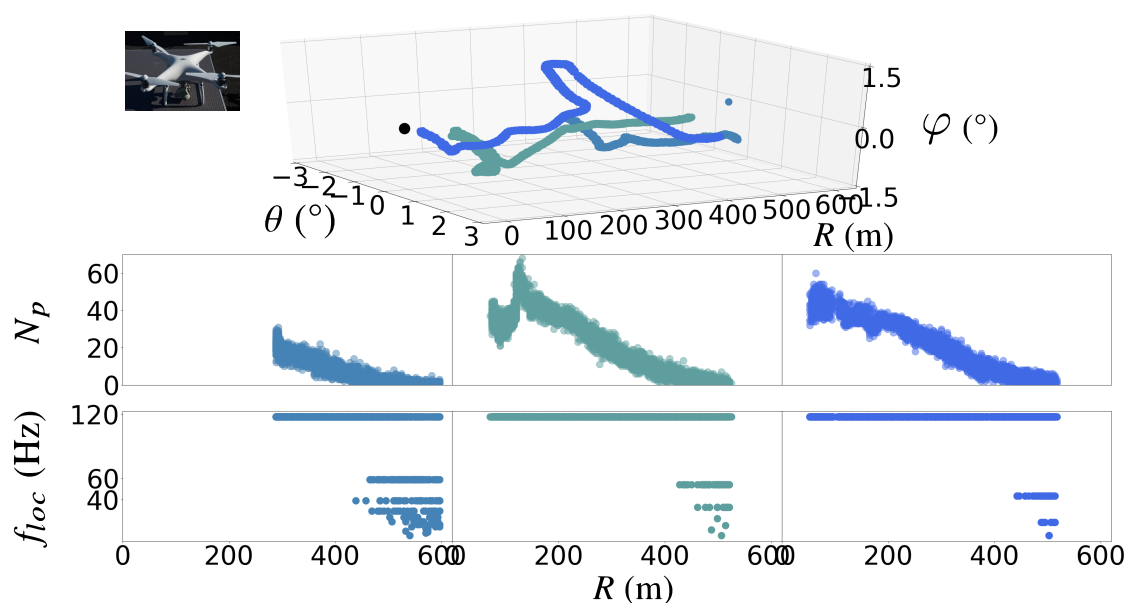


Figure 8.3: "Distancing" tracked trajectories of the phantom4.

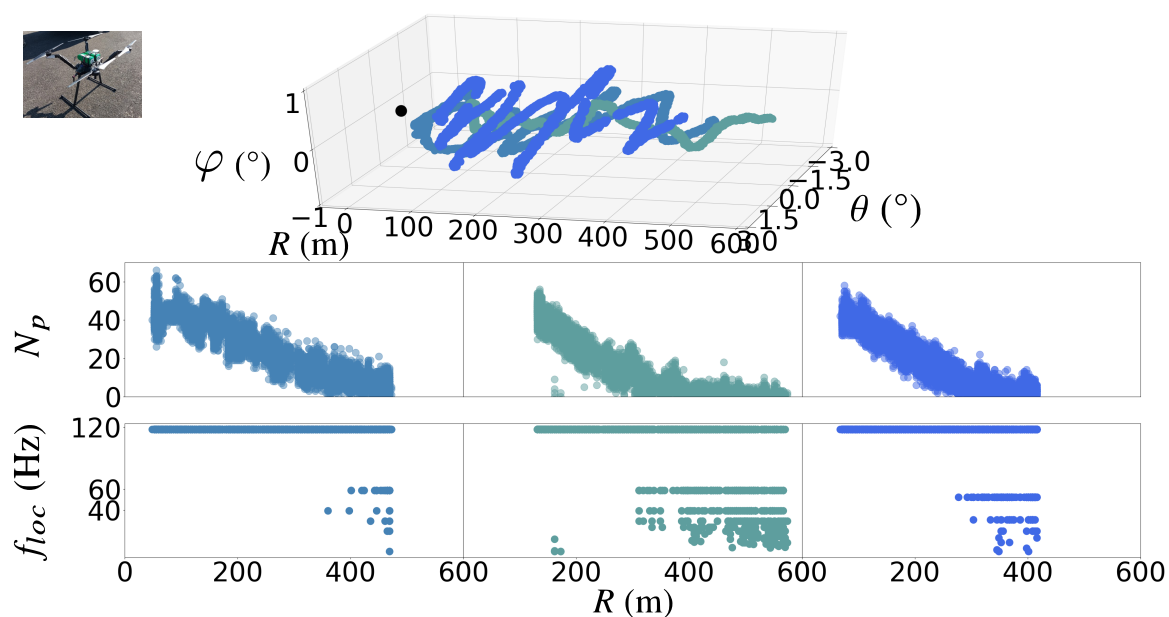


Figure 8.4: "Distancing" tracked trajectories of the black widow, with some "left-right" maneuvers.

Drone type	Max range at 120 Hz localization (m)	Max observed range (m)
Phantom4	430	610
Twinstar	280	420
Black widow	300	580

Table 8.9: Tracking range limits of the different drones.

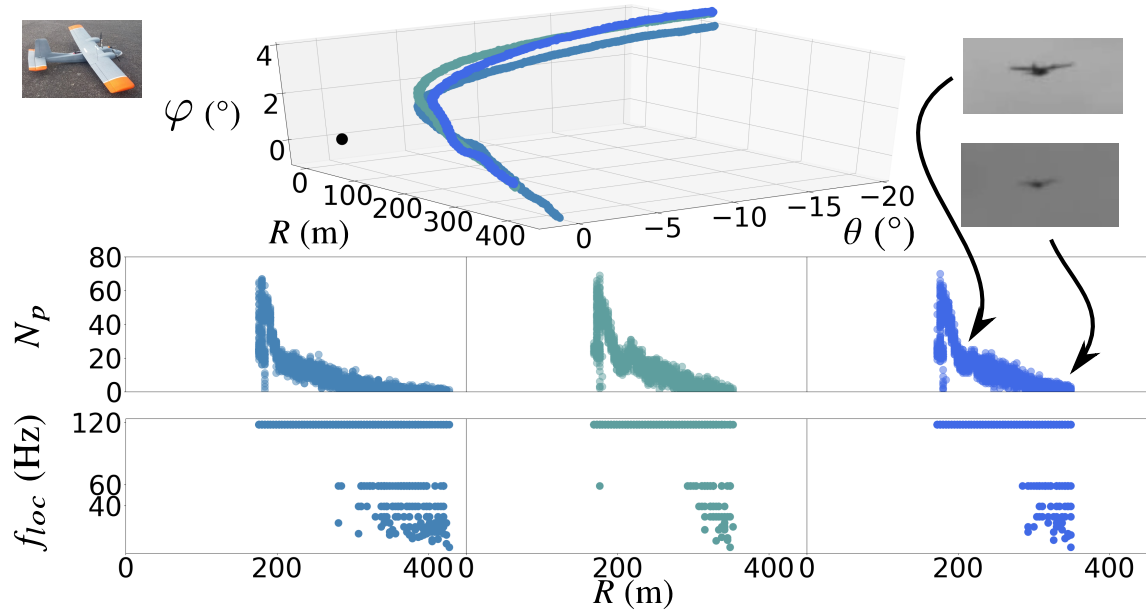


Figure 8.5: "Approach" tracked trajectories of the twinstar.

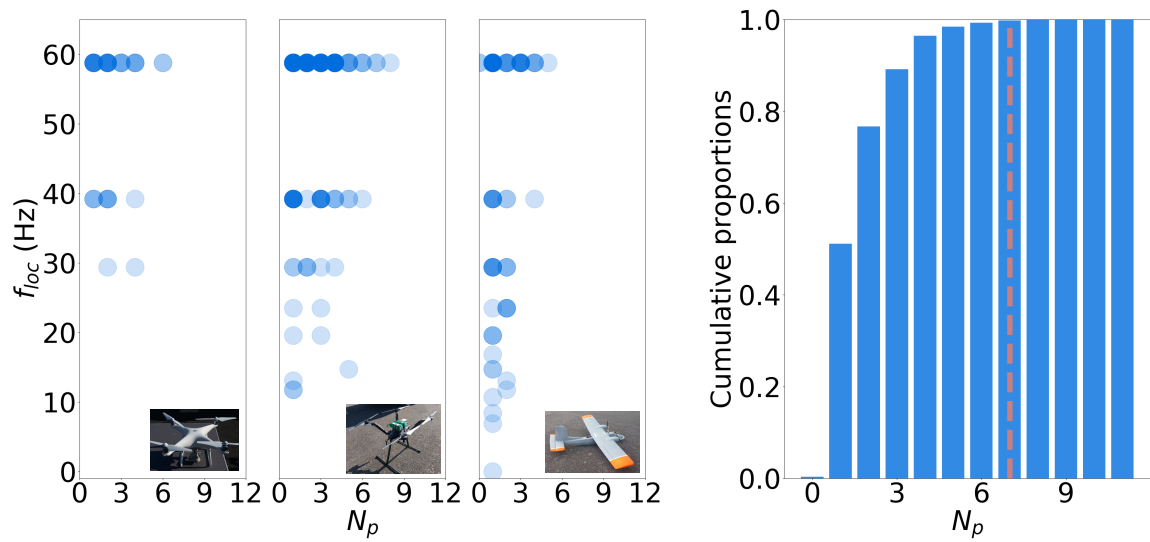


Figure 8.6: (Left) Histogram of the number of echoes per period for localization rates of 60 Hz or less for phantom4, black widow and twinstar trajectories. (Right) cumulative proportions of the number of echoes corresponding to localization rates of 60 Hz or less. $N_p=7$ (red dotted line) corresponds to more than 99% of the points.

angular resolution δ_θ and δ_φ , as well as the FoV (A_θ , A_φ) were fixed to get a scanning time T_{scan} of 8.7 s. The localization frequency of both the Lissajous and the CLV spiral were increased to 240 Hz, getting closer values shown in Table 8.5 and 8.6. We used a 30 kHz PRF, which is still relatively low, but necessary to get the wanted range. Unfortunately, due to a technical issue, the photodetector was replaced during the experiment and the alignment was remade quickly, resulting in a poorer sensitivity than the aforementioned 0.42 nW. Moreover, due to an error, the value of the threshold was set at $k=18$. The expected value of the sensitivity was closer to $\sigma_n=1$ nW.

The LiDAR parameters used during these trials are shown in Table 8.10.

Parameter	Value
P_e	4.1 kW
f_l	30 kHz
Θ_b	720 μrad
D_r	14 mm
σ_n	1 nW
k	18
η_e	0.95
η_r	0.58
Detection pattern	Raster-scan
(A_θ, A_φ)	(10°, 10°)
$(\delta_\theta, \delta_\varphi)$	(0.023°, 0.017°)
T_{scan}	8.7 s
Tracking pattern	Lissajous
n	2
f_p	720 Hz
Tracking pattern	CLV spiral
n	2
f_p	240 Hz
f_{loc}	240 Hz
A_p	0.43° at 100 m

Table 8.10: LiDAR parameters used during the first trials.

At first, we compared Lissajous and CLV spiral regarding range performance on a "distancing" trajectory. The results are displayed in Fig. 8.7 for a phantom4. The data on this figure confirms the theoretical analysis performed in section 6.3, knowing that the CLV spiral increases the probability of detection and thus produces much more echoes per period than the Lissajous (around a factor 2), while having the same period. As a result, tracking quality is maintained over a longer range, as f_{loc} start to drop from 240 Hz to 120 Hz 100 m later for the CLV spiral compared to the Lissajous. This also implies that tracking can work at longer range, as demonstrated here where the CLV spiral reaches almost 900 m while the Lissajous loses the target at 750 m. For all these reasons, the CLV spiral was the pattern used for the rest of the trials.

Then, we wanted to qualify the system for target speed and acceleration using "left-right" trajectories. Azimuthal speed V_c and acceleration a_c can be calculated from the trajectories by

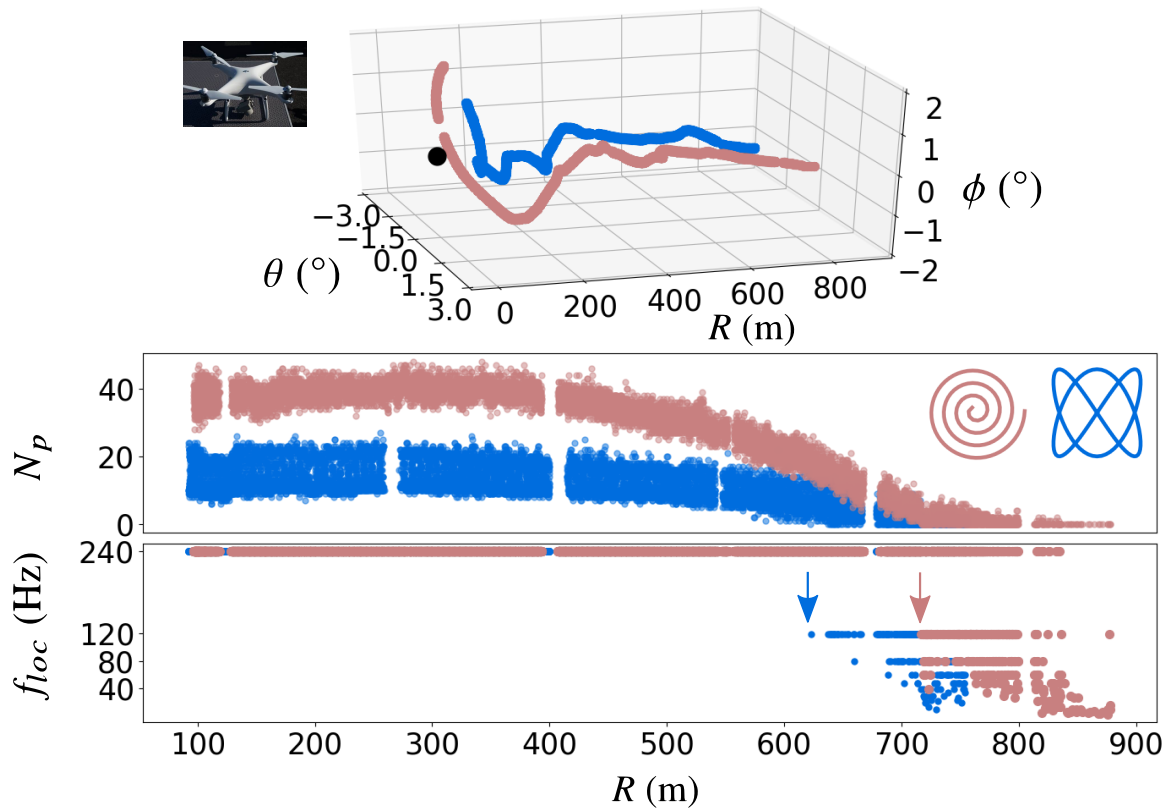


Figure 8.7: Tracked "distancing" angular trajectories for a phantom4 with a Lissajous (blue) and a spiral (red). The two colored arrows indicates the range at which tracking quality starts to drop. The spiral shows a 100 meter increase in performances compared to the Lissajous.

filtering the data and applying the derivative. Results are displayed in Fig. 8.8.

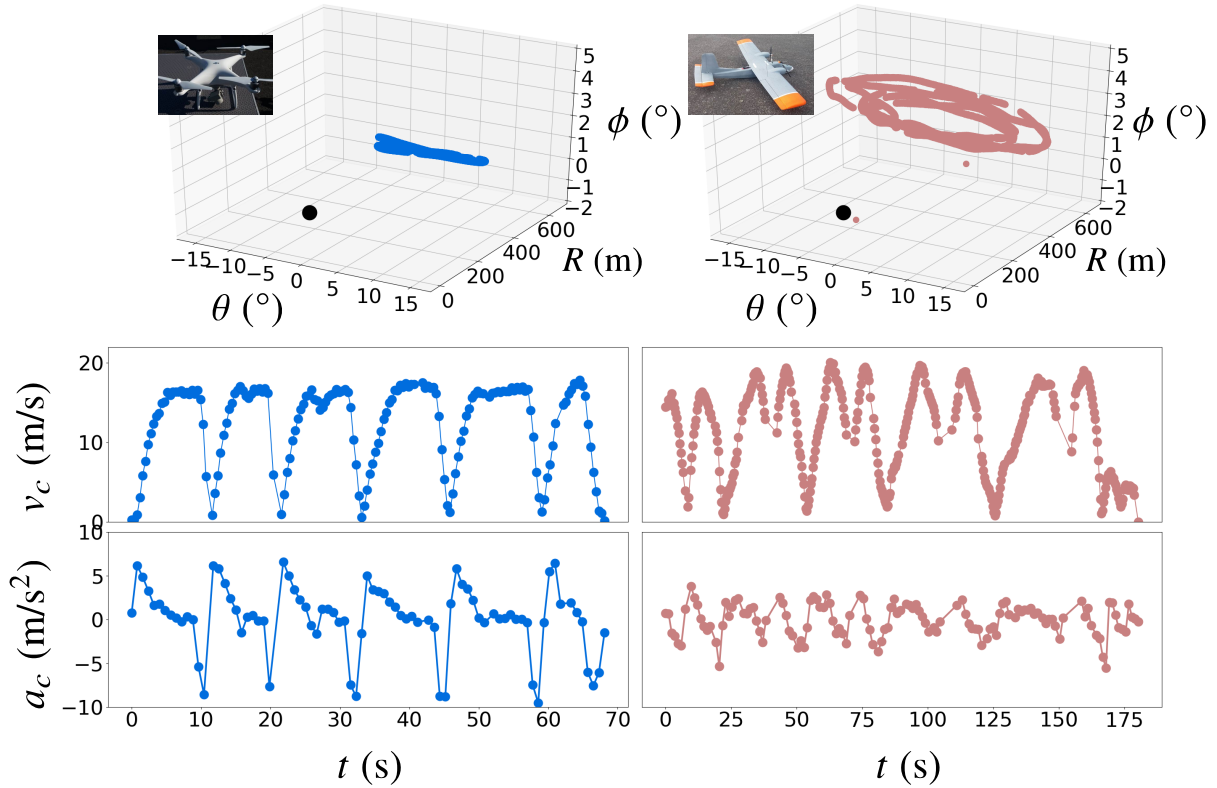


Figure 8.8: Tracked "left-right" angular trajectories for a phantom4 (left) and a twinstar (right), from which the filtered speed and acceleration can be deduced as a function of time.

The phantom4 was kept at 650 m with a perfectly one dimensional trajectory, whereas the twinstar had to do wider three dimensional loops and ranged from 400 to 650 m. In the trajectory, the succession of acceleration, top speed and deceleration can be clearly identified in the phantom4 data. Its maximum speed was measured at 17.5 m/s, which is close to the 20 m/s provided in the datasheet. Its deceleration is more powerful than its acceleration, reaching 1g at its peak. The smaller acceleration of the twinstar did not allow to reach the drone top speed. Nevertheless, speed up to 20 m/s is seen on the data. At closer range, tracking speed of 10°/s were recorded with our tracking method. In Fig. 8.9 is displayed a twinstar trajectory which shows increasing angular speed, up to 7°/s, as the drone is getting closer and abruptly turning from the system.

Because we did not have a GPS reference on our system, direct comparison with the drone registered trajectory was not possible. Therefore, pointing accuracy could not be gathered from tracking of a dynamic target. We had to settle for a static target, which we put fairly close to the system, adjusted in size to represent a 30 cm drone at 770 meters. Results are presented in Fig. 8.10. The standard deviation is 45 μ rad for 30 seconds of tracking, several times lower than target size. We can expect these results to be worse for moving targets, as blur effects and delays may induce offsets in the ecartometry. Shorter pattern periods can be used to reduced these effects, at the expense of a higher needed beam steerer bandwidth. Finally, a calibration

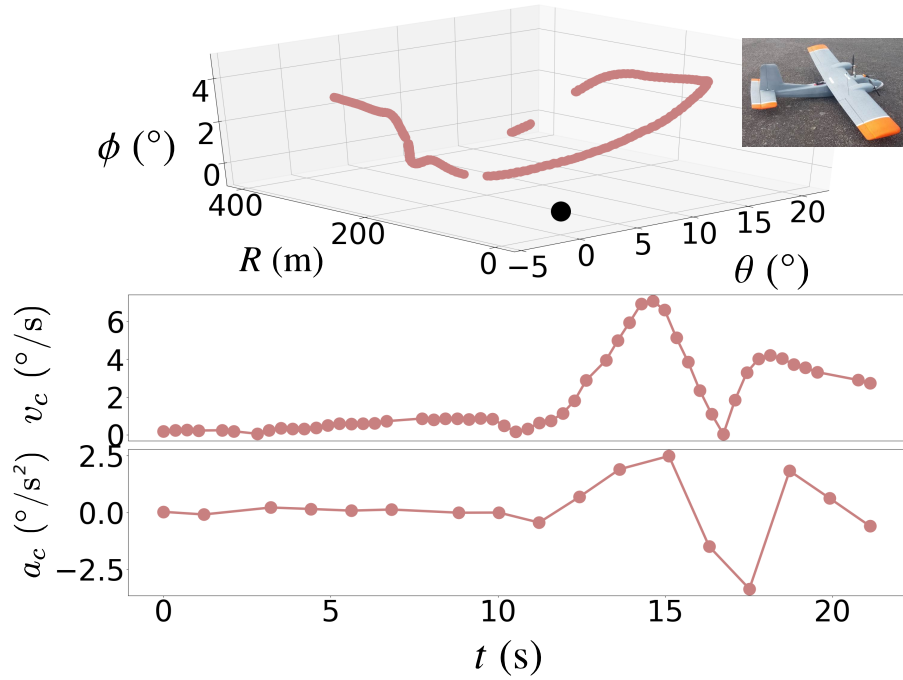


Figure 8.9: Twinstar trajectory showing angular speed up to $7^\circ/\text{s}$ at a close 200 m range.

(using a camera for instance) could be performed to accurately measure the bias and dispersion of the pointing system, completing these measurements.

We gathered a lot of data trajectory from the tracking of a phantom4, a twinstar and a black widow, which are shown in Fig. 8.11, 8.13 and 8.12.

It is interesting to note that tracking performance is strongly related to the drone type. For profiled flying wings such as the twinstar, its trajectory may expose different part of its structure to the LiDAR (long profile against narrow front), resulting in much more chaotic values of N_p and thus a potential lesser quality of tracking. This was only marginally seen on the previous trials because the twinstar evolved at an almost constant profile (see Fig. 8.5), except at the end when it turns. This can also be observed for the black widow, where we can perceive oscillations due to differences in profile, but they are less acute than with the twinstar.

It is also confirmed in Fig. 8.14, in the same fashion as in the previous trials with the Lissajous, less than 6 or 7 echoes correspond to a drop of the localization frequency. Finally, rough range limits for each drone is reported in Table 8.11. Performance have much improved compared to the BS architecture. The data registered during trials are used on the next section to characterize the probability of detection for each drone.

Drone type	Max range at 240 Hz localization (m)	Max observed range (m)
Phantom4	700	880
Twinstar	550	750
Black widow	650	810

Table 8.11: Tracking range limits of the different drones using a CLV spiral.

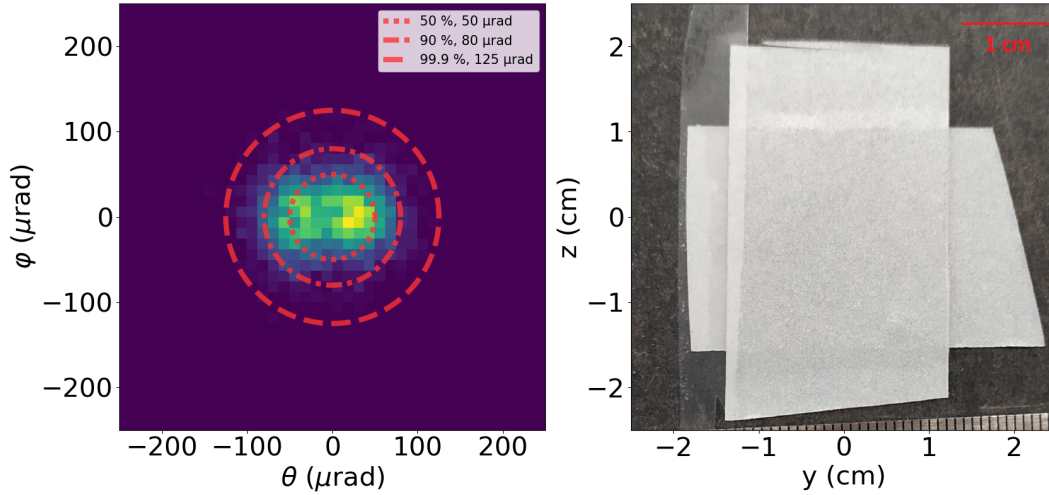


Figure 8.10: (Left) 2D Histogram of the pointing dispersion in tracking mode (CLV spiral at 240 Hz localization rate) for a 4 cm static target (right) at 102 meters, representing a 30 cm static drone at 770 meters. Both pictures are shown to scale, showing that angular dispersion is several times smaller than the target dimensions. The histogram pixel resolution is $12.4 \mu\text{rad}$ (galvanometer scanner resolution).

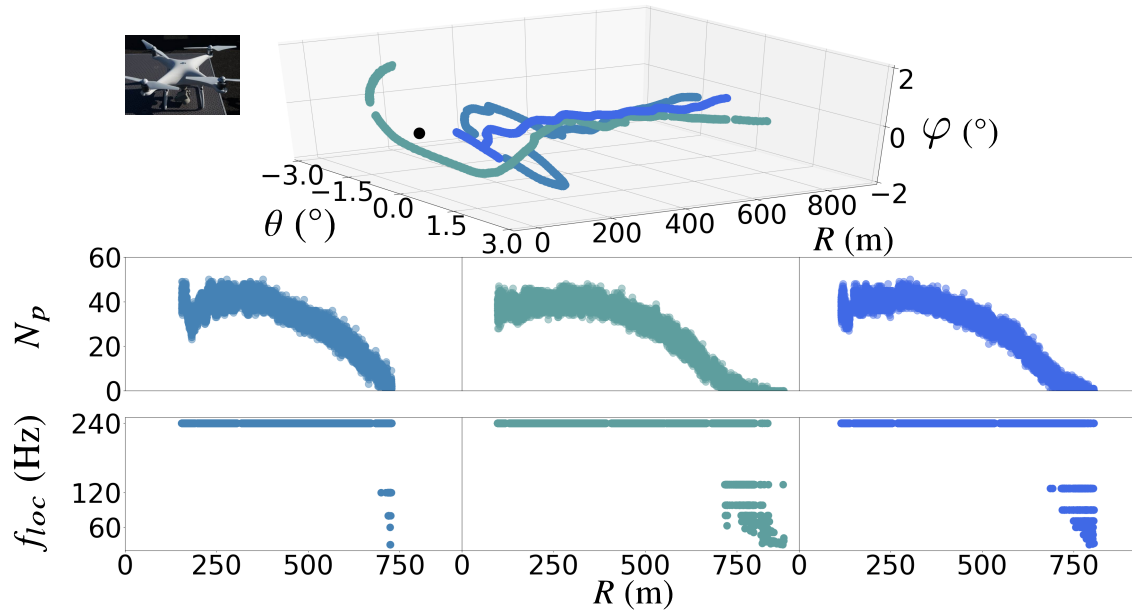


Figure 8.11: "Distancing" tracked trajectories of the phantom4 using a CLV spiral at 240 Hz localisation frequency.

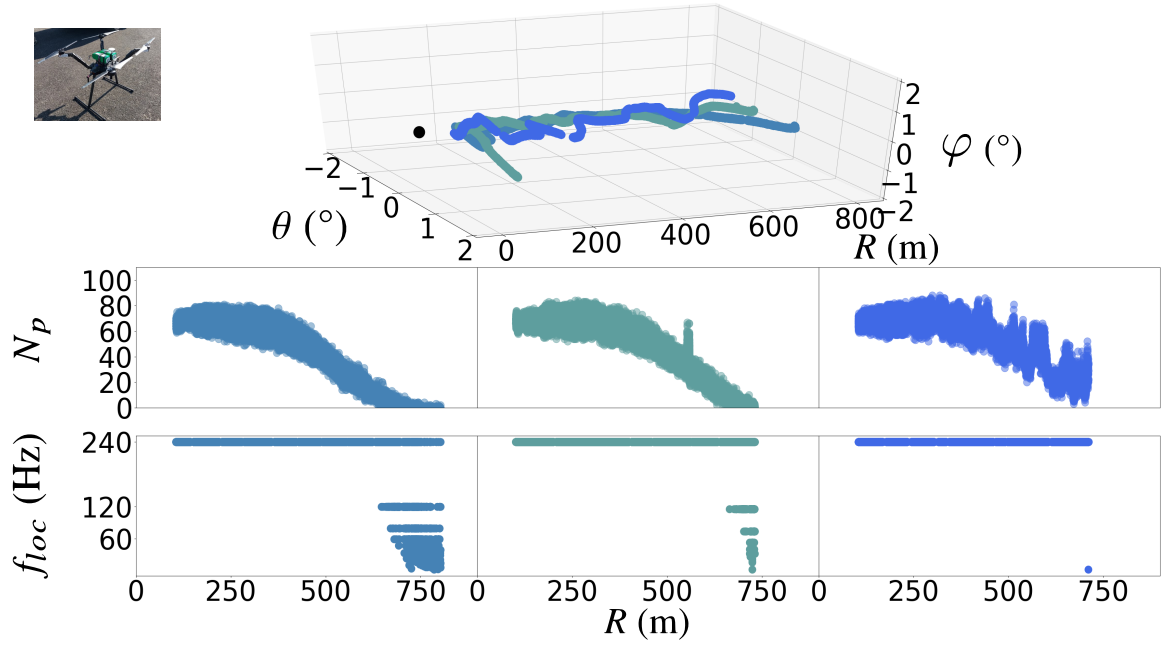


Figure 8.12: "Distancing" tracked trajectories of the black widow using a CLV spiral at 240 Hz localisation frequency.

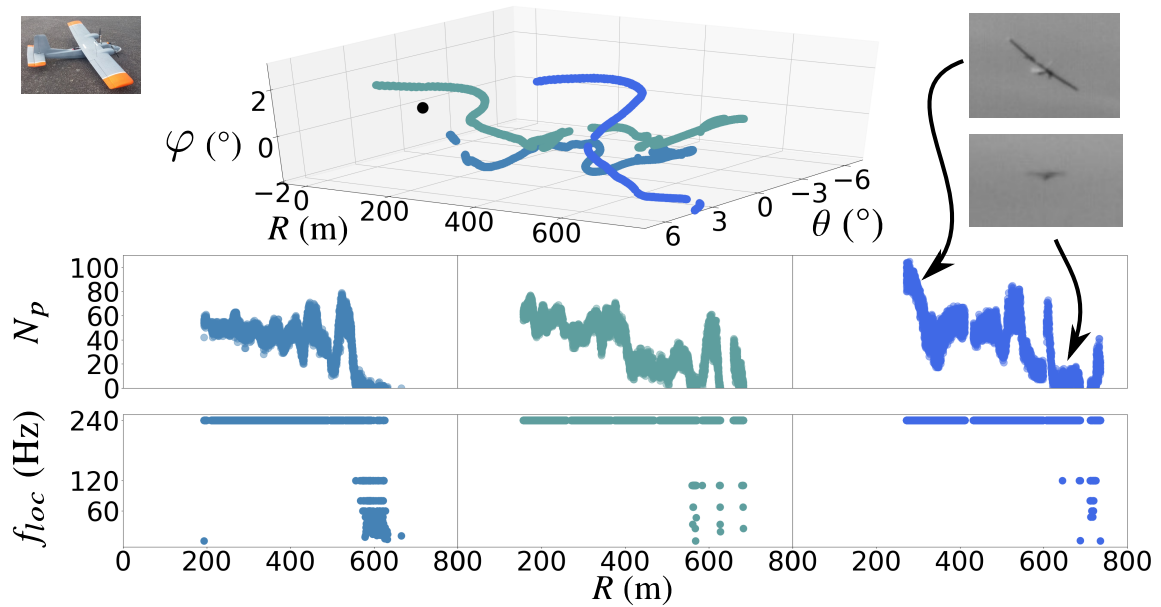


Figure 8.13: "Distancing" tracked trajectories of the twinstar using a CLV spiral at 240 Hz localisation frequency. We can note how N_p oscillates with the profile presented by the drone.

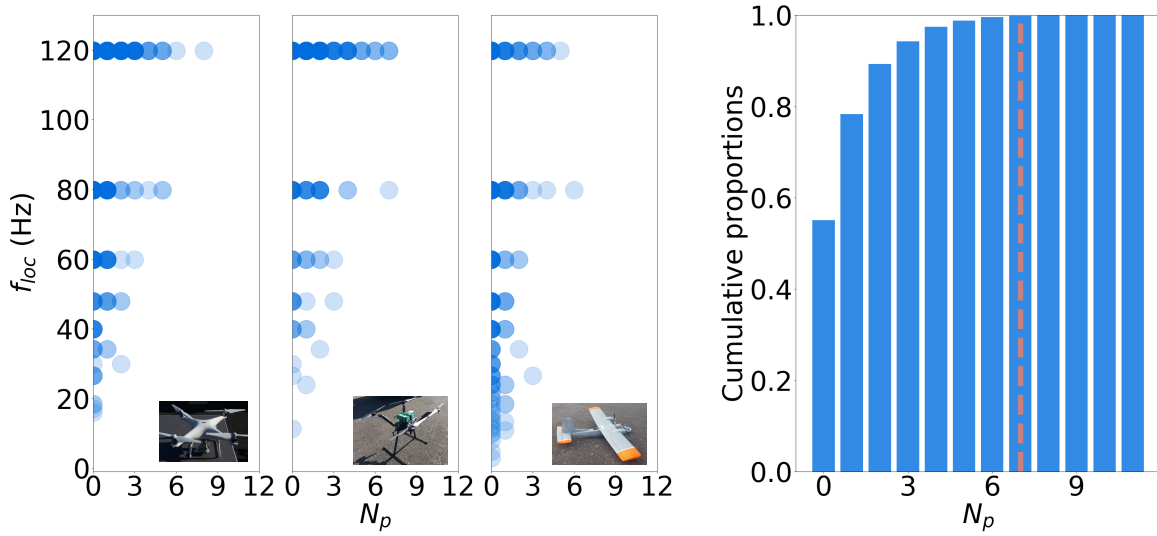


Figure 8.14: (Left) Histogram of the number of echoes per period for localization rates of 120 Hz or less for phantom4, black widow and twinstar trajectories, using a CLV spiral. (Right) cumulative proportions of the number of echoes corresponding to localization rates of 120 Hz or less. $N_p=7$ (red dotted line) corresponds to more than 99% of the points.

8.4 Imagery mode

8.4.1 3D point clouds

We also developed an imagery mode for our LiDAR system. In this mode, the scene is sequentially scanned and the complete point cloud is streamed from the FPGA to the host. Single image and videos are available, with the same performance as previously described. We added to possibility to gather multiple echoes from the same laser line, provided that they are separated by enough time to trigger individually the APD. This allows us to gather data points behind an another object, provided that is at least partially transparent. A point cloud example is displayed in Fig. 8.15, where we can see data behind the fence.

8.4.2 4D point clouds with signal intensity

We improved the system to be able to gather the return signal level on the APD receiver. One way to do it is to use a fast digitizer to sample the full signal waveform and to extract the return intensity from it. The sampling rate should be close to 1 GSa/s. And because we need it in real-time, this computation should be done on FPGA, which adds several levels of complexity. To simplify the design, we chose to use an envelope tracking and peak hold detector. The device is the HMC1120, with an envelope detection bandwidth >150 MHz. There is a digital selector which we can wire to the FPGA to switch between mode.

We use it as a way to "slow down" the return pulse so as to digitize the signal level with the 1 MSa/s ADC of our FPGA. To do so, we have to stay in envelope tracking mode during the pulse emission, which saturates the APD, then switch to peak hold. The device then conserves

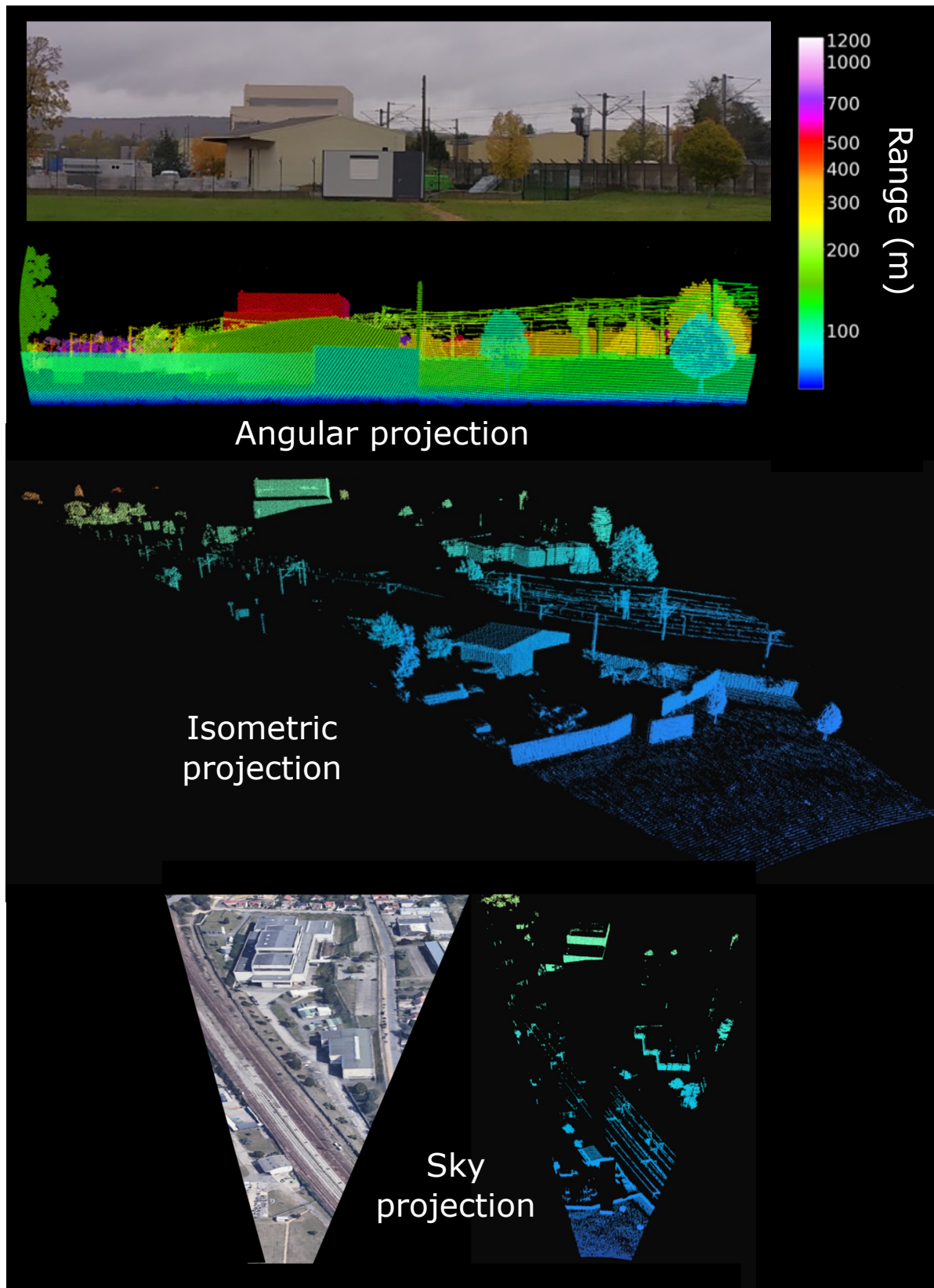


Figure 8.15: 3D point cloud made of different projections of our test field. Maximal range at this location is 1250 m. This image has a 0.02° lateral resolution for a $25^\circ \times 9^\circ$ FoV and took 12.5 second to scan. The range resolution is 65 cm.

the highest voltage level it comes across. If an echo is detected, we can then read this value with the ADC, and switch back to envelop tracking. This is presented in Fig. 8.16.

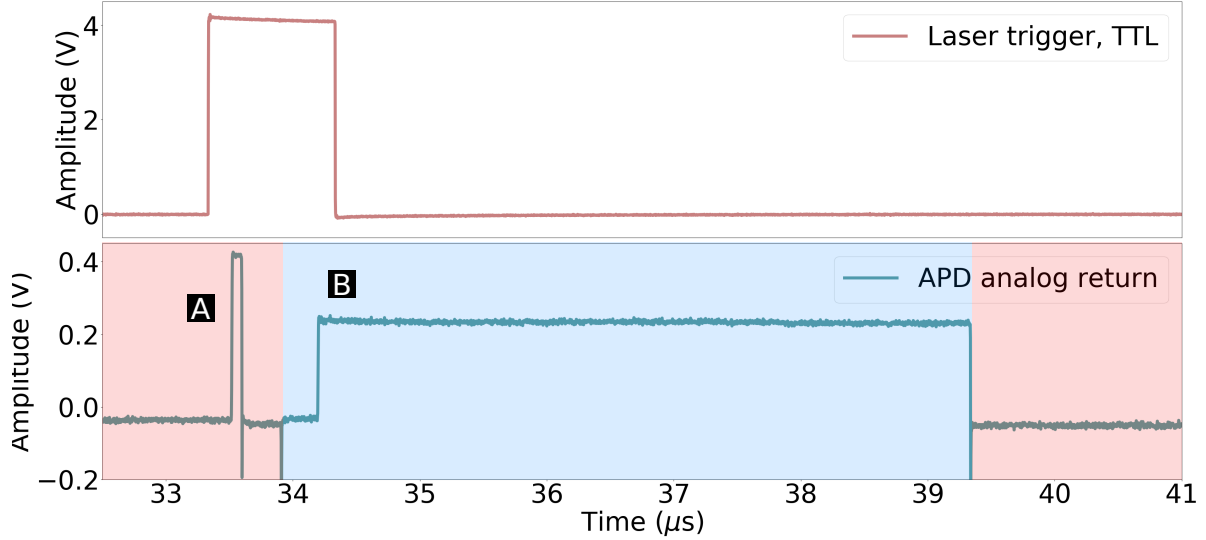


Figure 8.16: Temporal waveform of the LiDAR using signal intensity detection for a target located 104.5 meter away from the system. Envelope tracking is highlighted in light red and peak hold in light blue. (A) Initial pulse, which saturates the sensor. (B) Echo signal intensity, which is hold by the electronics until the ADC can read the value.

One drawback of this setup is that, due to the low digitizer rate, only a single intensity value can be read per emitted pulse. This can be seen in Fig. 8.17, where the same surfaces at the same range do not present the same intensity value because of others, more reflective object that are behind them. Another issue is the sensor dynamic range. Considering the peak power of the laser, close objects produce very intense echoes, which usually saturates the APD. Finally, color correction with range must be implemented to account for the link budget. In Fig. 8.17, we used a correction in $1/\ln(R)$.

8.5 Conclusion

In this chapter we calculated some limiting parameters of the LiDAR before the trials, such as the nominal hazard zone and the mechanical frequency of the different patterns. In the trials, we gathered 3D trajectory data points from three different drones, as well as two parameters indicators of the tracking quality: the number of echoes per period and the localization frequency. Two platforms were tested, and results showed a significant increase in maximal tracking range using the new platform, of around 300 meters or more (more than 30 % increases in performance). Localization frequencies of 240 Hz were performed, with drone speed reaching $7^\circ/\text{s}$ in angular speed at close range. Maximum phantom4 speed of more than 20 m/s was also measured at longer range. Finally a precision better than $100 \mu\text{rad}$ was confirmed using a static, placeholder target representing a 30 cm drone at 770 m.

One missing comparison in these trials is the comparison with the real drone position, by

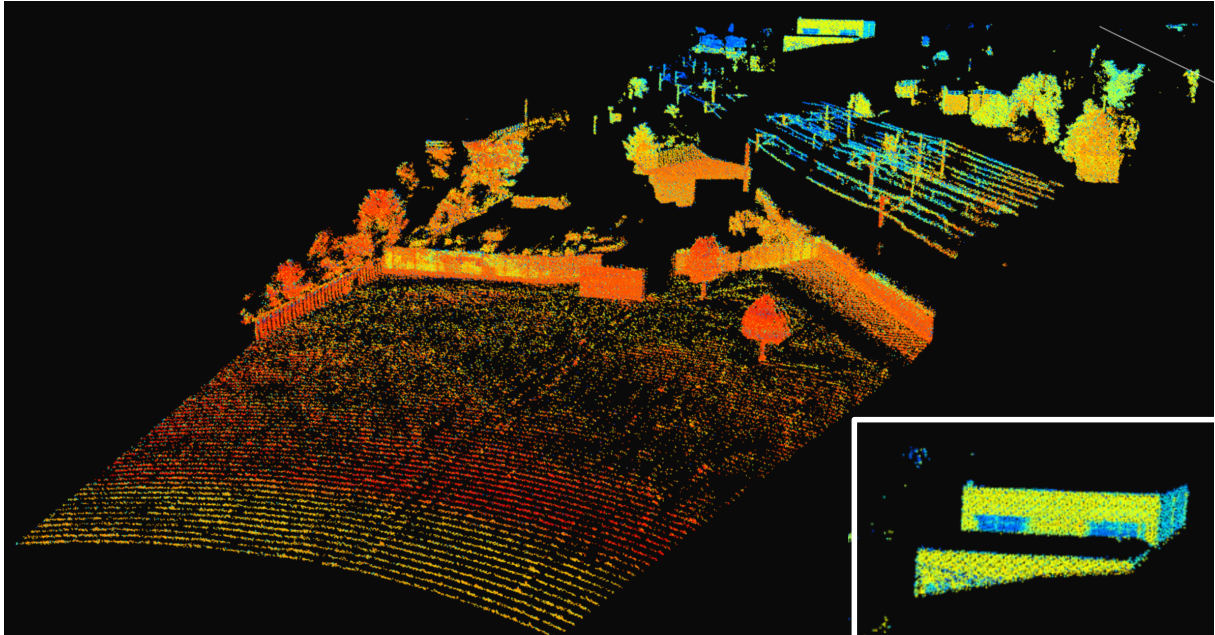


Figure 8.17: 4D Point cloud of the same scene. Colors represent the echo intensity corrected with range. The insert shows the windows on the building, a detail that was invisible before.

using GPS data for instance. This would highlight linearity issues of the beam steerer and potential systemic errors in the 3D data provided. Beyond that, these results are used in the next chapter to tune our models and simulations.

Model predictions and experimental confrontation

Contents

9.1	Fitting tracking data	121
9.2	Extrapolation to detection mode	125
9.3	Extrapolation to intrusion mode	129
9.4	Conclusion	130

In this chapter, we wish to use the data gathered during trials to fit some of our model parameters. More precisely, we wish to confirm if both the lambertian reflectivity and the simple disk hypothesis, despite their simplicity, can be enough to accurately describe the data. Here we are relying exclusively on the tracking data, more precisely the number of echoes per period N_p and the localization frequency f_{loc} .

9.1 Fitting tracking data

For each drone and each platform, we merged the three tracking trajectories presented on the previous chapter, to get an "average" of the spread of the number of echoes as a function of range. We chose to only consider the trials done with the platform **PM**. Indeed, the platform **BS** had a different detector, whose probability of detection was not measured. To reconstitute the value of N_p , noted N_p^{sim} , for each range R , we use the following numerical algorithm:

1. compute laser center positions within the pattern, as both the pattern diameter is known and the laser repetition rate f_l is known,
2. using a triangular distribution, randomly generate a number m of target center positions within u^*A_p ($u \in [0, 1]$) depending of the wanted dispersion. The triangular distribution means that it is slightly more likely to generate the target positions toward the center. For each target position:
 - (a) by numerical convolution, compute the list of surface overlap coefficients \mathcal{G} between each laser beam and the current target position,
 - (b) using Eq. (5.21), compute the list of corresponding expected average returned power P_r from the list of \mathcal{G} . Then, sample the value of $SNR = P_r / \sigma_n$ using the distribution whose cumulative distribution function is displayed on Eq. (5.40) (it is a Gaussian),

- (c) each generated SNR greater than the threshold is counted as an echo. The number of echoes per period N_p^{sim} for the current target center position is the sum of these echoes for a single period.

The N_p^{sim} values represent an interval of confidence for N_p , as we don't know the exact relative position of the target within the pattern for each periods. From this simulation, we can also compute the average value of the localization frequency. The localization frequency behavior is described on section 8.3. If we introduce m_0 as the number of target positions within the pattern not producing an echo for each range R, then the average value of the localization frequency f_{loc}^{sim} can be approximated by:

$$\langle f_{loc}^{sim} \rangle = \frac{1}{T_p} \sqrt{1 - \frac{m_0}{m}}. \quad (9.1)$$

This expression is more akin to a regression to fit the curve than a complete description of the process behind the localization rate. Nevertheless, as seen on the next figures, it provide a good fit.

For the simulation, every parameter was kept the same as during the experiment, either measured or known by design, and were previously reported in Tables 8.8 and 8.10. The atmospheric attenuation coefficient was chosen as $\kappa=0.1 \text{ km}^{-1}$, which corresponds to standard visibility around 1500 nm for an horizontal path at sea level [Carter 1974]. The target parameters that best fitted the data are presented in Table 9.1.




	Phantom4 (DJI) 	Twinstar RD RR (Multiplex) 	Black Widow (Vulcan UAV) 
D_r	30 cm	20 cm	45 cm
\mathcal{R}_π	0.2	0.09	0.1

Table 9.1: Diameter and equivalent lambertian reflectivity that best fit the tracking data recorded with our model.

We first compared the fit between a CLV spiral and a Lissajou with a phantom4 in a distancing trajectory. Results are shown in Fig. 9.1.

As seen on this figure, both the value difference and the decrease of N_p with range between the spiral and the Lissajous are very accurately fitted. These results are produced by using a target distribution extremely close to the center ($0.1 \cdot A_p$ dispersion range) for the spiral, and fairly wide for the Lissajous ($0.6 \cdot A_p$ dispersion range). This observation can be explained by the nature of our algorithm, as we are using a simple average of echoes localization rather than a barycenter during tracking. This means that high density areas on the pattern have more weight because of the higher number of potential echoes located there. This may result in an over compensation of the offset and, if repeated, to an oscillation effect of the pattern center around the target. It also explains the higher dispersion of the value of N_p for the Lissajous, as

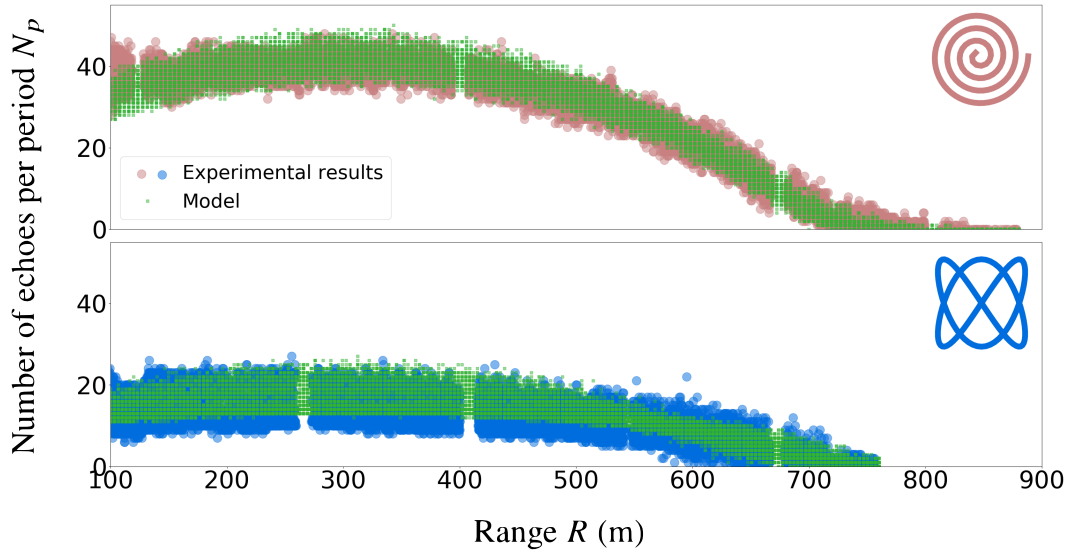


Figure 9.1: Experimental and theoretical fit of the number of echoes per period as a function of range for a phantom4 tracked in a distancing trajectory, using a [CLV spiral](#) (up) and a [Lissajou](#) (down) pattern.

the target is sometimes located in the low density area (center), sometimes on the high density one (edges). In case of the spiral, the high uniformity seems to prevent this oscillation.

The simulation proves that our model can accurately describe the tracking behavior for both types of patterns. Then, we applied our simulation to the three types of drones. The results are presented in [Fig. 9.2](#), [9.3](#) and [9.4](#), using for each figure three trajectories (previously presented in [Fig. 8.11](#), [8.12](#)) and [8.13](#), which are merged into a single one.

It is very clear on these figures that the fit is the best for the phantom4, which shows high symmetry and rotational invariance, translating into a reflectivity invariance. The black widow is an intermediate case, being of relatively high symmetry, and mostly fit our model. There are some divergence visible in [Fig. 9.3](#), with some parts highlighting a higher than predicted number of echoes. It may be possible that some structures of higher reflectivity intermittently intersect with the pattern.

Finally, the twinstar behavior is the farthest away from our model. The difference of color of the material, i.e. its ability to absorb light rather than back-scatter it, might explain the short range observed. Indeed, the twinstar is grey compared to the phantom4 which is a bright white. Another possibility is a difference in cross-section. Indeed, for the trajectories in [Fig. 9.4](#) the twinstar is performing some "left-right" maneuvers, exposing a more or less surface to the [LiDAR](#). We chose to fit our model on the minimal amount of echoes, which represent a worst case scenario, when the drone nose is facing the system.

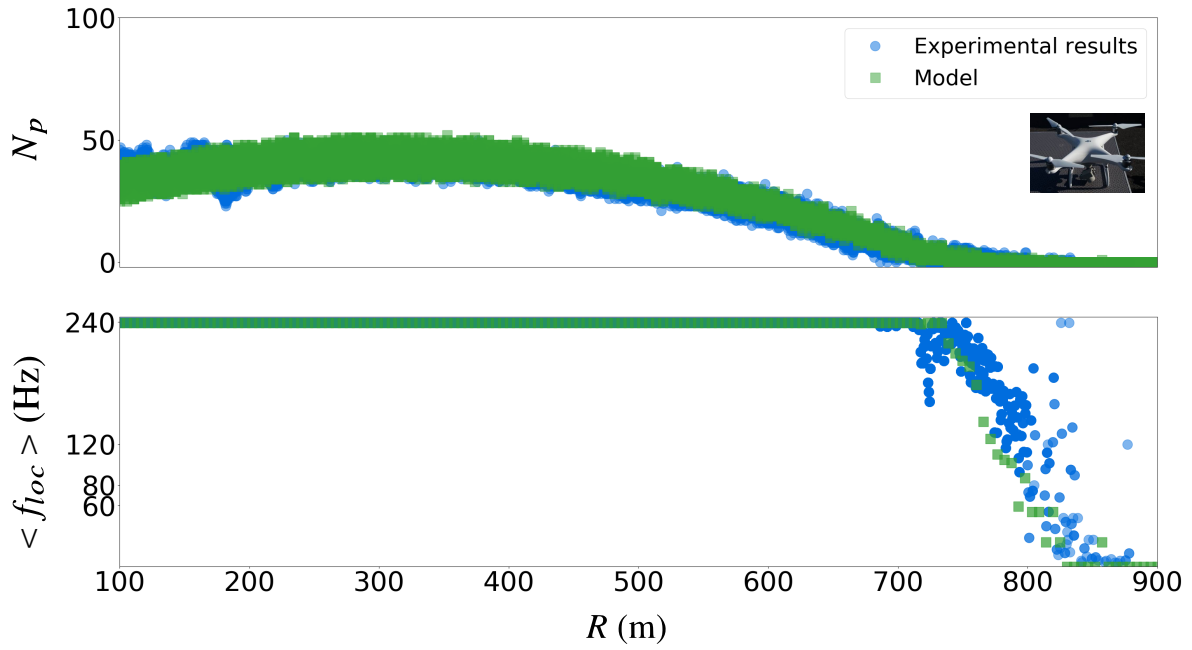


Figure 9.2: Comparison of simulated and measured data of N_p and $\langle f_{loc} \rangle$ for 3 combined trajectory of the phantom4 using a CLV spiral of 240 Hz frequency.

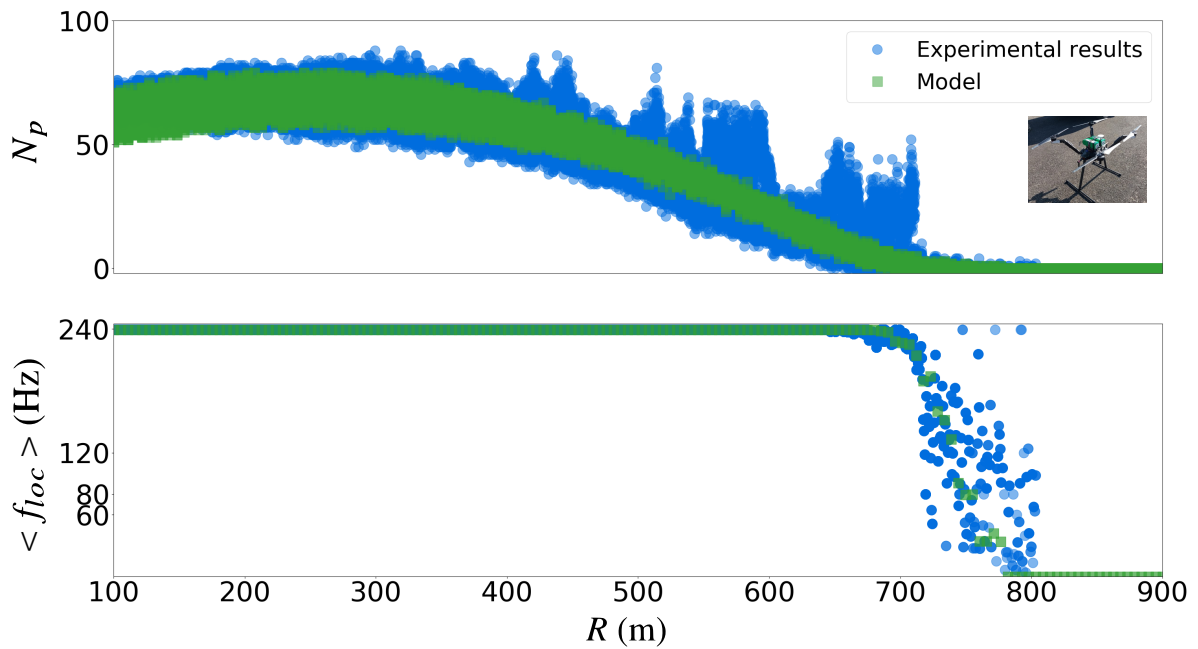


Figure 9.3: Comparison of simulated and measured data of N_p and $\langle f_{loc} \rangle$ for 3 combined trajectory of the black widow using a CLV spiral of 240 Hz frequency.

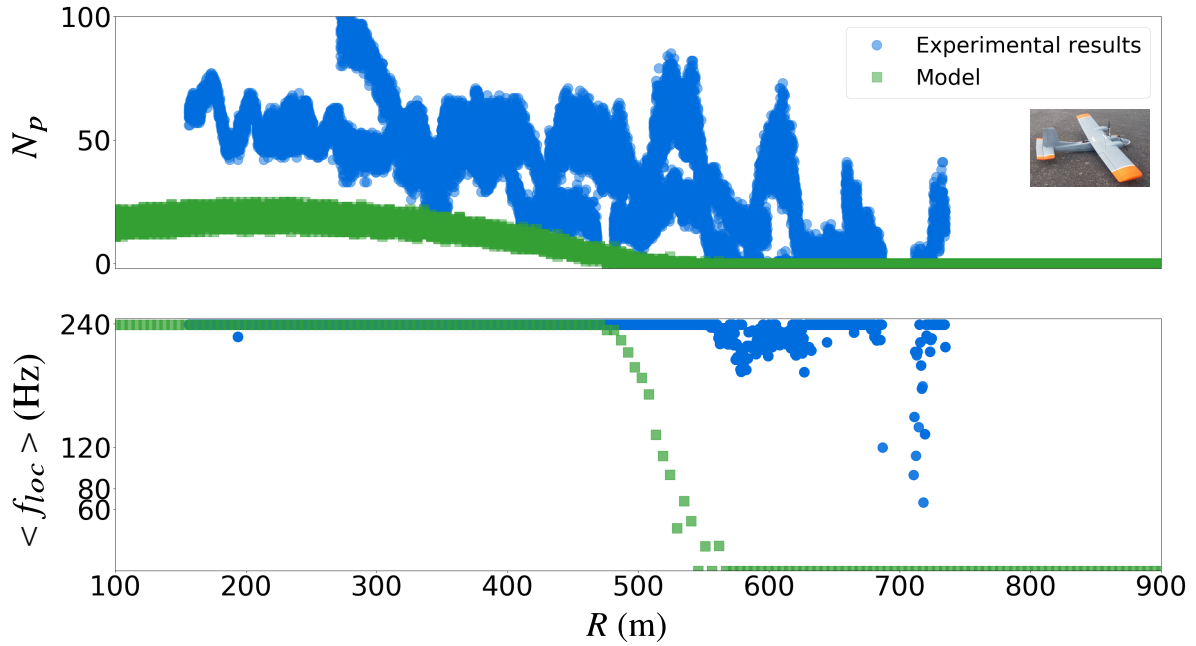


Figure 9.4: Comparison of simulated and measured data of N_p and $\langle f_{loc} \rangle$ for 3 combined trajectory of the twinstar using a CLV spiral of 240 Hz frequency.

9.2 Extrapolation to detection mode

The tracking data gave us information on two main parameters, that is the hemispheric reflectivity of the lambertian model, and the drone diameter. We have seen that the model perfectly fits the phantom4, but much less so the twinstar. This means that we can fortunately use the phantom4 as a point of reference for performance comparison in detection mode between the platform BS and PM. The pattern parameters are described in Table 9.2. The other system parameters are presented in Tables 8.8 and 8.10. The APD sensitivity is set to its nominal value for the platform PM, as there was oversight on that part during trials.

Parameter	Value
Detection pattern (A_θ, A_φ) ($\delta_\theta, \delta_\varphi$) T_{scan}	Raster-scan ($10^\circ, 10^\circ$) ($0.023^\circ, 0.017^\circ$) 8.7 s
platform σ_n k	BS 7.8 nW 5
platform σ_n k	PM 0.42 nW 11

Table 9.2: Raster-scan and APD parameters used in this section.

We want to compare both system with a static drone, assuming $V_c=0$. To do so, we used the single-echo model presented on Eq. (6.17). For each range R , the numerical algorithm is as follow:

1. generate a target matrix containing a disk of size $D_r * D_r$. Generate a centered Gaussian beam matrix of waist W . The matrix dimension is at least $D_r + R\delta_\theta$ and $D_r + R\delta_\varphi$ on each dimension to be able to compute the overlap matrix,
2. by numerical convolution of the two matrices, compute the surface overlap matrix \mathcal{G} ,
3. using Eq. (6.17), compute the probability of detection for this range R , the integral being replaced by a sum on the matrix pixels.

This algorithm must undergo heavy computations regarding the numerical convolution. The pixel resolution must be kept high enough for each range R . This is difficult to balance because at close range, the target is much bigger than the beam, and the reverse is true at long range. In any case, the simulation spans several minutes. We can see the results of the simulation in Fig. 9.5, which shows that the range is almost doubled between platforms. Subsequent tests confirmed detection of the phantom4 up to 1050 m, which correlates pretty well with what was found on the simulation.

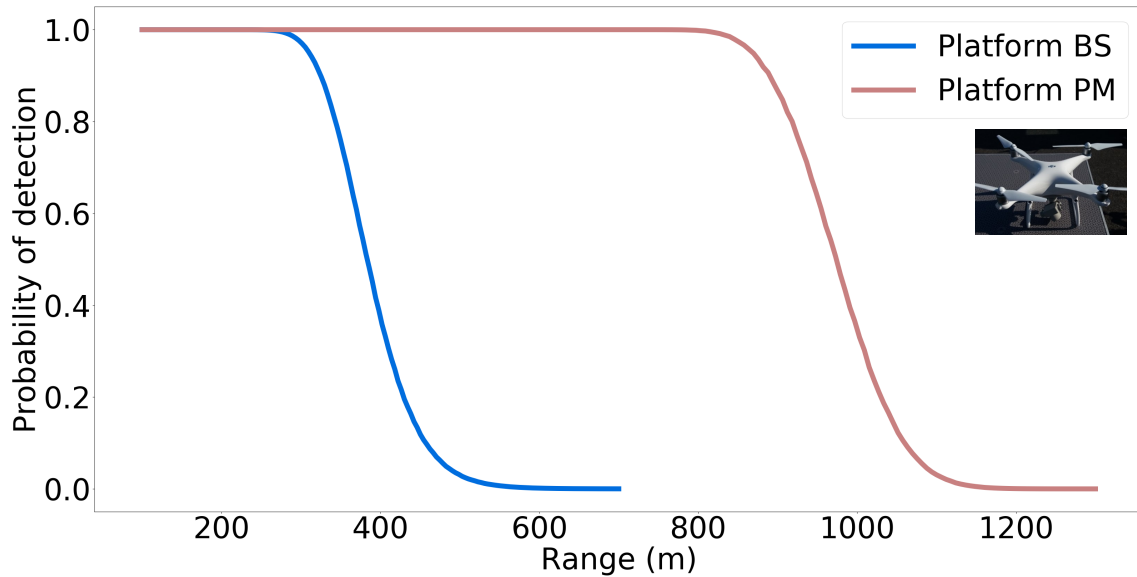


Figure 9.5: Comparison of simulated \mathcal{P}_d in a detection sequence of a static phantom4 between the two platforms using the same scanning parameters. The range performance is almost doubled.

We now wish to compare the results of two of our models: the single-echo, which was used for the comparison between platforms in Fig. 9.5, and the mutli-echo. To this effect, we are using the same parameters as before, but only considering the platform PM. The algorithm for the single-echo was described previously. The algorithm for the multi-echo was described on subsection 6.1.1. We are using the same mesh resolution in both cases. The multi-echo is limited

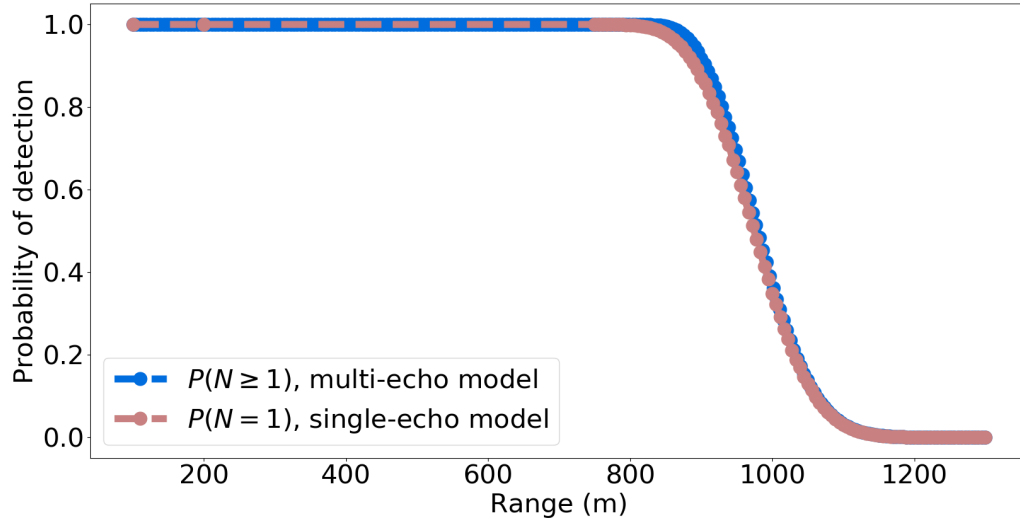


Figure 9.6: Comparison of the simulated probability of detection for the multi-echo versus the single-echo, for a phantom4 using the platform PM. The same scanning parameters are used in both cases.

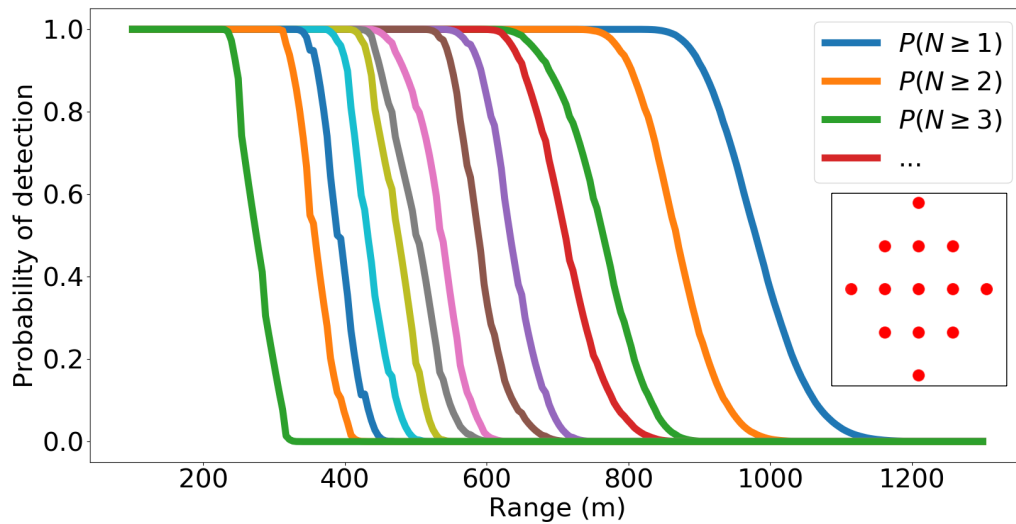


Figure 9.7: Simulated probability of having m echos among $N=13$ pulses, for a phantom4 using the platform PM. The red dots in the insert show the N pulses arrangement.

to 13 beams, arranged in the form of a losange (see insert in Fig. 9.7). The results are displayed in Fig. 9.6 and 9.7.

On these figures, we can see that both algorithms gives very close results for one echo. It is very important to note that this result heavily depends on the scanning configuration. Here, the target has a smaller angular size than the beam at ranges where the probability starts to drop, and the values of δ_θ and δ_φ are also on the same order of magnitude. This means that the impact of beams other than the center one are almost negligible, and justifies the use of the single-echo algorithm to drastically reduce computation time (single-echo is 130 times faster). Nevertheless, it is interesting to see that to get 10 echoes, which could be a threshold needed by a recognition algorithms, we need to have a drone at 500 meters, which is half the system maximal range. One way to go around this is to use a more resolved pattern (such as in tracking mode) to increase the number of echoes and thus allow for proper recognition.

At last, we wish to quantify the impact of the target speed v_c on the probability of detection. This was studied on section 6.1.3. We concluded there that we could use an expression close to the one that one found for the single-echo development, by including the target speed in the integral domain. The full expression was given on Eq. (6.23). We can therefore reuse the same algorithm previously described. Using the parameters shown in Table 9.2, the fast axis driving frequency is $f_\theta=26$ Hz. We plot the probability of detection as a function of both the range and the speed in Fig. 9.8, using a phantom4 and the platform PM.

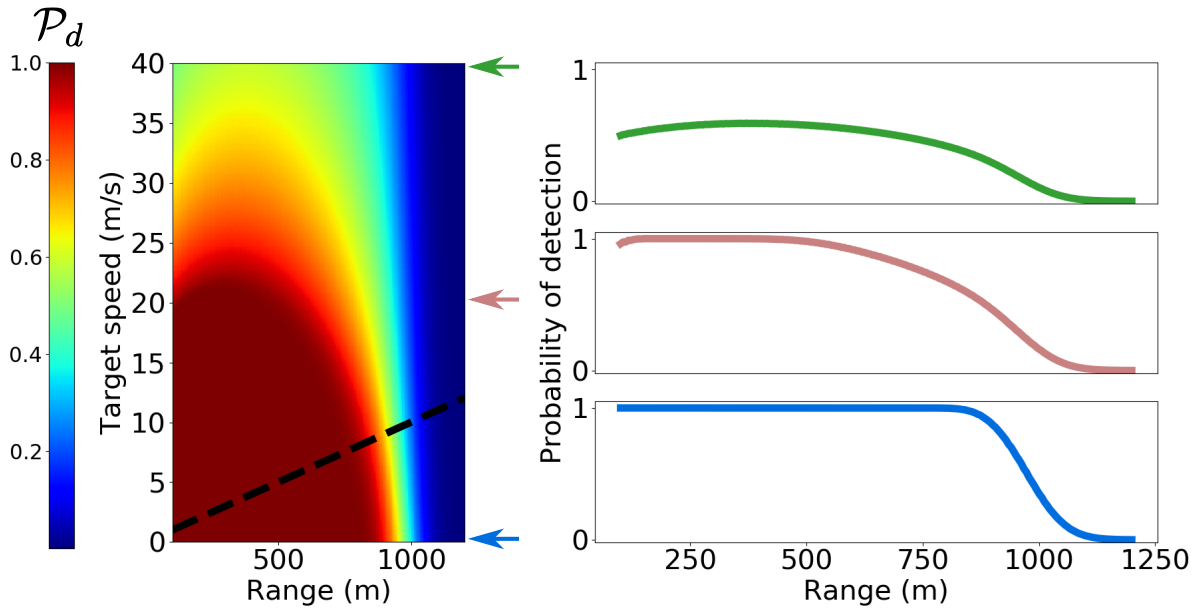


Figure 9.8: (Left) simulated probability of detection as a function of both range and target speed, for a phantom4 with the platform PM. The black dotted line represents the limited by the scanning duration (from Eq. (6.20)). (Right) Probability of detection for (up to down) 40, 20 and 0 m/s a function of range. The simulation is done for a phantom4 using the platform PM.

On this figure, we can see that target speed does play a significant role in the probability of detection. It is interesting to note that for relatively high speed, \mathcal{P}_d increases slightly with

range before decreasing again. This is due to the beam divergence, as the beam is smaller at close range, which decreases the probability of detection because the angular surface in which the target can be found is much larger than the beam. At longer range, the beam is larger, but at the same time the link budget is less favorable. Therefore, we observe a distance at which the beam diameter and link budget are at an equilibrium. Moreover, for the considered target speed, the probability never goes under 50% at close range. This can be roughly explained by saying that even for fast targets, there is always a substantial probability that the target finds itself close enough to a beam to trigger an echo.

Another thing to note is that with 10° optical and 8.7 s of scan, the maximal target speed is very limiting (black dotted line). This limit represents a target starting at the center of the field, and going to the same direction as the scan, meaning that it can escape the field before the beam has the time to catch up (see Eq. (6.20)). In any case, it is still a good indicator that the scanning time is a hard limit for detecting fast targets.

9.3 Extrapolation to intrusion mode

Finally, we can use our model to predict the performance of the intrusion mode. We continue to use the **PM** platform, with parameters described in Table 8.10. The remaining parameters used are shown in Table 9.3.

Parameter	Value
A_s	5°
f_i	50 Hz
\mathcal{R}_π	0.2
σ_n	0.42 nW
k	11

Table 9.3: Intrusion mode parameters used in this section.

We use $\mathcal{R}_\pi=0.2$, as this seems to be a relatively balanced value for the reflectivity, neither too low nor too high. The diameter of the angular cone to secure is 5° . This is an operational specification, but it could be scaled to a reaction time compared to a given intruder speed. Low circle frequency f_i provides smaller "holes" in the circle via a smaller δ_i^o (see Eq. (??)), meaning that caching small intruder is easier, but at the same time get a higher chance to miss high speed target via a higher δ_i^r (see Eq. (5.4)). Here 50 Hz is a fairly achievable frequency at 5° and represents a good compromise.

We decided to plot the probability to detect the intruder as a function of both the intruder diameter D_i and its speed V_i . We run the simulation for 3 ranges: 500, 1000 and 1500 meters. The results are displayed in Fig. 9.9.

We can see on this figure that the probability of detection regresses with range, which is due to the link budget being less favorable. At 1 km, detection of small targets is not possible. The impact of the intruder speed is weaker than range, with detection still holding at 50% and more for intruders evolving at 50 m/s (180 km/h).

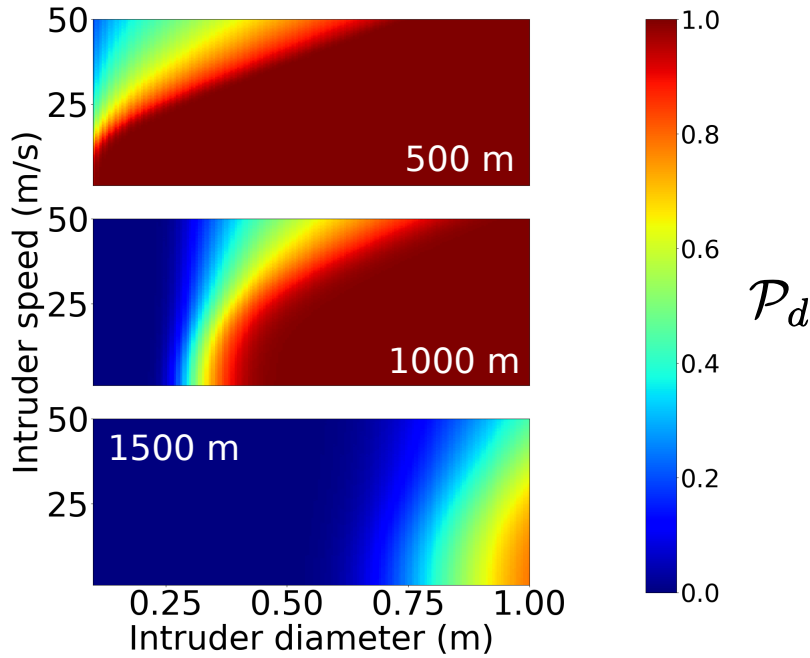


Figure 9.9: Simulated probability of detection as a function of both the intruder speed and size using the platform [PM](#), for 3 different ranges.

9.4 Conclusion

In this chapter, we used the experimental results gathered during the two trials sessions to fit our models. We have an exceptionally good fit with the phantom4, able to reproduce both the number of echoes per period and the localization frequency across range, for both case of a Lissajous or a [CLV](#) spiral. The black widow is a good fit but local deviations with the model starts to appear. Finally the twinstar is not within the boundaries of our model. Deviations can be explained by a variation of the cross-section of the drone during its trajectory, which is very visible for fixed wings such as the twinstar.

Phantom4 data allowed us to simulate the probability of detection during detection mode (scanning a wide area) for both the [BS](#) and [PM](#) platform, which revealed a factor 2 increase in term of maximal range. The impact of the drone speed was also studied, showing that scanning duration is a crucial parameter to consider for fast targets. At last, a parametric simulation for the intrusion mode displayed how the probability of detection evolved with both the intruder speed and size.

Conclusion

In this manuscript, we presented parallel developments of theoretical models and an experimental platform aimed toward long range detection and tracking of UAV, using a scanning LiDAR. We focused our study on the different components of our LiDAR system, and merged them to predict the global performances of various operating modes. We used our experimental platform to gather relevant parameters for each component. Moreover, we used the data accumulated during UAV trials sessions, in the form of the number of echoes and localization rate, to fit our models. We could therefore make them more accurate, or highlight some of their limitations.

With this development, we achieved a deep understanding of our system. We provided a link between, on one side, individual components such as the laser source, the beam steerer and the detection chain, and on the other side the target and its characteristics in terms of size and speed. The crucial step to bring these parameters together was to deal with the scanning pattern, i.e. the way the laser beams are distributed on the scene across time and space. By introducing the surface overlap coefficient between the target and the beam, we provided a way to account for the pattern shape, angular amplitude, and period. The obtained result is the probability to get one or more echoes on the given target, which is a function of all the parameters previously mentioned.

This approach is perhaps our stronger added value to this field. We provided a guideline on how to design a scanning LiDAR to answer a set of operational requirements. This guideline leads to a deeply multi-parametric model which, provided some reference data are accessible, can in turn provide a deep insight of the system performance. This model can be used to quantify gains and losses when optimizing some parameters regarding a given goal. For instance, we can firstly quantify the impact of decreasing the scanning time to detect faster moving targets, which is done at the expense of angular resolution. Secondly, tracking refresh rate can be improved at the expense of a higher beam steerer bandwidth, which in turn scales down the beam steerer size, thus its and finally limits the maximal range.

We have used this parallel approach to iterate on the design and parameters of our LiDAR, and to improve its performance. At the end, we reach a 240 Hz localization rate, more than 1 km range for a phantom4, and an angular precision smaller than the target dimension, achieving a better static stability than 150 μ rad at long range. Despite using a fairly simple model for the target, reducing it to a flat disk of lambertian properties, we succeeded in seeing great agreements between simulations and experimental data for this drone. Of course, this has some shortcomings, specifically regarding fixed wings targets such as the twinstar. For these types of targets, the additions of more parameters is unavoidable, considering that their profile and cross-section are heavily orientation dependent.

On that specific matter, a slightly more complex model introducing the yaw or pitch of the target, coupled to some geometric primitives (cylinders and spheres), could drastically improve experimental fit. The basis for this study would include a deeper modeling of the geometrical

interactions between the beam and the target surface, and the evolution of the link budget with the angle of incidence and surface normal. This way, we could compute the evolution of the maximal range as a function of the drone trajectory, position and angle parameters. An achievement would then be to fit one of our [LiDAR](#) tracking data set by accurately computing the drone orientation at each instant.

Multi-target tracking is also a real challenge that should be addressed, as fleets of drones are becoming a reality. One approach would be to divide our tracking time between multiple targets at the same time. This would require predicting one target position while the system is busy refreshing another one, by applying signal processing and automatic filters. Kalman filtering, notably used in radar, would be a first approach. Increasing the scanning capabilities to scan a larger angular portion of the scene faster could also allow for background and multi-target awareness.

Finally, another untouched field of study in this manuscript is drone recognition. It is one thing to be able to detect and track a target, but it is another to confirm its identity. On that issue, our multi-echo approach can provide the added value of a range limit for a given algorithm to have enough points to recognize the drone. We could also work on the target high resolution point cloud, generated during tracking, to gather classification characteristics such as size, shape and behavior. Overall, the integration of a clustering and classifying algorithm within our model would add another level of understanding and a deeper reach, drawing a complete picture from individual components performance up to global target recognition.

Bibliography

- [Agishev *et al.* 2013] Ravil Agishev, Adolfo Comerón, Jordi Bach, Alejandro Rodriguez, Michael Sicard, Jordi Riu and Santiago Royo. *Lidar with SiPM: Some capabilities and limitations in real environment*. Optics & Laser Technology, vol. 49, pages 86–90, 2013. (Cited on page 11.)
- [Aylward 2003] Redmond P Aylward. *Advanced galvanometer-based optical scanner design*. Sensor review, 2003. (Cited on pages 13 and 82.)
- [Baumeister 2004] Philip Baumeister. Optical coating technology, volume 137. SPIE press, 2004. (Cited on page 91.)
- [Behroozpour *et al.* 2017] Behnam Behroozpour, Phillip AM Sandborn, Ming C Wu and Bernhard E Boser. *Lidar system architectures and circuits*. IEEE Communications Magazine, vol. 55, no. 10, pages 135–142, 2017. (Cited on pages 3 and 9.)
- [Bell *et al.* 1960] Ely E Bell, Leonard Eisner, James Young and Robert A Oetjen. *Spectral radiance of sky and terrain at wavelengths between 1 and 20 microns. II. Sky measurements*. JOSA, vol. 50, no. 12, pages 1313–1320, 1960. (Cited on page 91.)
- [Benyamin & Goldman 2014] Minas Benyamin and Geoffrey H Goldman. *Acoustic detection and tracking of a Class I UAS with a small tetrahedral microphone array*. Technical report, ARMY RESEARCH LAB ADELPHI MD, 2014. (Cited on pages 16 and 17.)
- [Birch *et al.* 2015] Gabriel C Birch, John C Griffin and Matthew K Erdman. *UAS Detection, Classification, and Neutralization: Market Survey 2015*. Sandia National Laboratories, 2015. (Cited on pages 1, 15 and 19.)
- [Blais *et al.* 2000] Francois Blais, J Angelo Beraldin and Sabry F El-Hakim. *Range error analysis of an integrated time-of-flight, triangulation, and photogrammetric 3D laser scanning system*. In Laser Radar Technology and Applications V, volume 4035, pages 236–247. International Society for Optics and Photonics, 2000. (Cited on pages 21 and 30.)
- [Breiter *et al.* 2018] R Breiter, M Benecke, D Eich, H Figgemeier, T Ihle, A Sieck, A Weber and J Wendler. *Extended SWIR imaging for targeting and reconnaissance*. In Infrared Technology and Applications XLIV, volume 10624, page 1062403. International Society for Optics and Photonics, 2018. (Cited on pages 1, 18 and 24.)
- [Busset *et al.* 2015] Joël Busset, Florian Perrodin, Peter Wellig, Beat Ott, Kurt Heutschi, Torben Rühl and Thomas Nussbaumer. *Detection and tracking of drones using advanced acoustic cameras*. In Unmanned/Unattended Sensors and Sensor Networks XI; and Advanced Free-Space Optical Communication Techniques and Applications, volume 9647, page 96470F. International Society for Optics and Photonics, 2015. (Cited on page 17.)
- [Cao *et al.* 2020] Changqing Cao, Xiyuan Su, Yutao Liu, Xiaodong Zeng, Zhejun Feng, Jingshi Shen, Ting Wang and Xu Yan. *compensation for the Decoherence Effect in Heterodyne*

- Detection of Rough Targets and a Target Vibration characteristic Measurement System*. Scientific reports, vol. 10, no. 1, pages 1–13, 2020. (Cited on page 13.)
- [Caris *et al.* 2015] M Caris, W Johannes, S Stanko and N Pohl. *Millimeter wave radar for perimeter surveillance and detection of MAVs (Micro Aerial Vehicles)*. In 2015 16th International Radar Symposium (IRS), pages 284–287. IEEE, 2015. (Cited on page 16.)
- [Carter 1974] DR Carter. *Burle electro-optics handbook*, 1974. (Cited on page 122.)
- [Chevrier & Campanella 2016] M Chevrier and G Campanella. *LIDAR Pulsed Time of Flight Reference Design*, 2016. (Cited on page 9.)
- [Christnacher *et al.* 2016] Frank Christnacher, Sébastien Hengy, Martin Laurenzis, Alexis Matwyschuk, Pierre Naz, Stéphane Schertzer and Gwenaél Schmitt. *Optical and acoustical UAV detection*. In Electro-Optical Remote Sensing X, volume 9988, page 99880B. International Society for Optics and Photonics, 2016. (Cited on pages 1, 18 and 24.)
- [Christodoulakis & Ford 1989] Stavros Christodoulakis and Daniel Alexander Ford. *File organizations and access methods for CLV disks*. In Proceedings of the 12th annual international ACM SIGIR conference on Research and development in information retrieval, pages 152–159, 1989. (Cited on page 72.)
- [Church *et al.* 2018] Philip Church, Christopher Grebe, Justin Matheson and Brett Owens. *Aerial and surface security applications using lidar*. In Laser Radar Technology and Applications XXIII, volume 10636, page 1063604. International Society for Optics and Photonics, 2018. (Cited on pages 19 and 21.)
- [Drège *et al.* 2000] Emmanuel M Drège, Neal G Skinner and Dale M Byrne. *Analytical far-field divergence angle of a truncated Gaussian beam*. Applied optics, vol. 39, no. 27, pages 4918–4925, 2000. (Cited on page 36.)
- [Eldada 2018] Louay Eldada. *Three-dimensional-mapping two-dimensional-scanning lidar based on one-dimensional-steering optical phased arrays and method of using same*, January 16 2018. US Patent 9,869,753. (Cited on page 12.)
- [Farlik *et al.* 2016] Jan Farlik, Miroslav Kratky, Josef Casar and Vadim Stary. *Radar cross section and detection of small unmanned aerial vehicles*. In 2016 17th International Conference on Mechatronics-Mechatronika (ME), pages 1–7. IEEE, 2016. (Cited on page 16.)
- [Farlik *et al.* 2019] Jan Farlik, Miroslav Kratky, Josef Casar and Vadim Stary. *Multispectral detection of commercial unmanned aerial vehicles*. Sensors, vol. 19, no. 7, page 1517, 2019. (Cited on page 16.)
- [Fiocco & Smullin 1963] G Fiocco and LD Smullin. *Detection of scattering layers in the upper atmosphere (60–140 km) by optical radar*. Nature, vol. 199, no. 4900, pages 1275–1276, 1963. (Cited on page 1.)
- [Fukshansky 2009] Lenny Fukshansky. *Revisiting the hexagonal lattice: on optimal lattice circle packing*. arXiv preprint arXiv:0911.4106, 2009. (Cited on page 29.)

- [Gettinger & Michel 2015] Dan Gettinger and A Holland Michel. *Drone sightings and close encounters: An analysis*. Center for the Study of the Drone, Bard College, Annandale-on-Hudson, NY, USA, 2015. (Cited on page 1.)
- [Godbaz *et al.* 2012] John P Godbaz, Michael J Cree and Adrian A Dorrington. *Understanding and ameliorating non-linear phase and amplitude responses in amcw lidar*. Remote Sensing, vol. 4, no. 1, pages 21–42, 2012. (Cited on page 6.)
- [Goodman 2007] Joseph W Goodman. *Speckle phenomena in optics: theory and applications*. Roberts and Company Publishers, 2007. (Cited on page 48.)
- [Grönwall *et al.* 2007] Christina Anna Grönwall, Ove K Steinvall, Fredrik Gustafsson and Tomas R Chevalier. *Influence of laser radar sensor parameters on range-measurement and shape-fitting uncertainties*. Optical Engineering, vol. 46, no. 10, page 106201, 2007. (Cited on page 37.)
- [Guvenc *et al.* 2018] Ismail Guvenc, Farshad Koohifar, Simran Singh, Mihail L Sichertiu and David Matolak. *Detection, tracking, and interdiction for amateur drones*. IEEE Communications Magazine, vol. 56, no. 4, pages 75–81, 2018. (Cited on pages 1, 15 and 19.)
- [Haag *et al.* 2019] Hervé Haag, Thibault de la Villegeorges and Bruno Esmiller. *Method and device for securing a space crossed by a high-power laser beam*, October 29 2019. US Patent 10,459,082. (Cited on page 31.)
- [Hall 2011] David S Hall. *High definition lidar system*, June 28 2011. US Patent 7,969,558. (Cited on page 12.)
- [Haluza & Čechák 2016] Michal Haluza and Jaroslav Čechák. *Analysis and decoding of radio signals for remote control of drones*. In 2016 New Trends in Signal Processing (NTSP), pages 1–5. IEEE, 2016. (Cited on page 16.)
- [Hammer *et al.* 2018] Marcus Hammer, Marcus Hebel, Björn Borgmann, Martin Laurenzis and Michael Arens. *Potential of lidar sensors for the detection of UAVs*. In Laser Radar Technology and Applications XXIII, volume 10636, page 1063605. International Society for Optics and Photonics, 2018. (Cited on page 19.)
- [Hecht 2018] Jeff Hecht. *Lidar for self-driving cars*. Optics and Photonics News, vol. 29, no. 1, pages 26–33, 2018. (Cited on page 1.)
- [Hoffmann *et al.* 2016] Folker Hoffmann, Matthew Ritchie, Francesco Fioranelli, Alexander Charlish and Hugh Griffiths. *Micro-Doppler based detection and tracking of UAVs with multistatic radar*. In 2016 IEEE Radar Conference (RadarConf), pages 1–6. IEEE, 2016. (Cited on page 16.)
- [Horaud *et al.* 2016] Radu Horaud, Miles Hansard, Georgios Evangelidis and Clément Ménier. *An overview of depth cameras and range scanners based on time-of-flight technologies*. Machine vision and applications, vol. 27, no. 7, pages 1005–1020, 2016. (Cited on pages 3 and 11.)

- [Huntington *et al.* 2018] Andrew S Huntington, George M Williams and Adam O Lee. *Modeling false alarm rate and related characteristics of laser ranging and LIDAR avalanche photodiode photoreceivers*. Optical Engineering, vol. 57, no. 7, page 073106, 2018. (Cited on pages 45 and 47.)
- [Huntington 2016] Andrew Huntington. *Sensitivity analysis of APD photoreceivers*. Voxel technical note, 2016. (Cited on page 42.)
- [ICN 1998] *ICNIRP GUIDELINES FOR LIMITING EXPOSURE TO TIME-VARYING ELECTRIC, MAGNETIC AND ELECTROMAGNETIC FIELDS (UP TO 300 GHZ)*, 1998. (Cited on page 16.)
- [Imaki *et al.* 2015] Masaharu Imaki, Shumpei Kameyama, Akihito Hirai, Kimio Asaka and Yoshihito Hirano. *Laser radar system*, April 14 2015. US Patent 9,007,600. (Cited on page 11.)
- [Jenn 2005] David Jenn. Radar and laser cross section engineering. American Institute of Aeronautics and Astronautics, Inc., 2005. (Cited on page 39.)
- [Kameyama *et al.* 2007] S Kameyama, T Ando, K Asaka, Y Hirano and S Wadaka. *Compact all-fiber pulsed coherent Doppler lidar system for wind sensing*. Applied optics, vol. 46, no. 11, pages 1953–1962, 2007. (Cited on page 6.)
- [Karlsson & Olsson 1999] Christer J Karlsson and Fredrik ÅA Olsson. *Linearization of the frequency sweep of a frequency-modulated continuous-wave semiconductor laser radar and the resulting ranging performance*. Applied optics, vol. 38, no. 15, pages 3376–3386, 1999. (Cited on page 6.)
- [Kasturi *et al.* 2016] Abhishek Kasturi, Veljko Milanovic, Bryan H Atwood and James Yang. *UAV-borne lidar with MEMS mirror-based scanning capability*. In Laser Radar Technology and Applications XXI, volume 9832, page 98320M. International Society for Optics and Photonics, 2016. (Cited on pages 21 and 30.)
- [Kim *et al.* 2008] Young Min Kim, Derek Chan, Christian Theobalt and Sebastian Thrun. *Design and calibration of a multi-view TOF sensor fusion system*. In 2008 IEEE Computer Society Conference on Computer Vision and Pattern Recognition Workshops, pages 1–7. IEEE, 2008. (Cited on page 1.)
- [Kim *et al.* 2018a] Byeong Kim, Danish Khan, Ciril Bohak, Wonju Choi, Hyun Lee and Min Kim. *V-rbnn based small drone detection in augmented datasets for 3d lidar system*. Sensors, vol. 18, no. 11, page 3825, 2018. (Cited on page 19.)
- [Kim *et al.* 2018b] Byeong Kim, Min Kim and You Chae. *Background registration-based adaptive noise filtering of lwir/mwir imaging sensors for uav applications*. Sensors, vol. 18, no. 1, page 60, 2018. (Cited on page 17.)
- [Kim *et al.* 2018c] Taehwan Kim, Pavan Bhargava and Vladimir Stojanović. *Overcoming the Coherence Distance Barrier in Long-Range FMCW LIDAR*. In CLEO: Science and Innovations, pages STh3L–7. Optical Society of America, 2018. (Cited on page 6.)

- [Kim *et al.* 2019] Byeong Hak Kim, Danish Khan, Wonju Choi and Min Young Kim. *Real-time counter-UAV system for long distance small drones using double pan-tilt scan laser radar*. In Laser Radar Technology and Applications XXIV, volume 11005, page 110050C. International Society for Optics and Photonics, 2019. (Cited on pages 15 and 19.)
- [Laurenzis & Woiselle 2014] Martin Laurenzis and Arnaud Woiselle. *Laser gated-viewing advanced range imaging methods using compressed sensing and coding of range-gates*. Optical Engineering, vol. 53, no. 5, page 053106, 2014. (Cited on page 11.)
- [Laurenzis *et al.* 2019] Martin Laurenzis, Martin Rebert, Emmanuel Bacher and Stéphane Schertzer. *Active and passive computational imaging for tracking and prediction of three-dimensional MUAV flight paths*. In Electro-Optical Remote Sensing XIII, volume 11160, page 1116009. International Society for Optics and Photonics, 2019. (Cited on pages 1 and 18.)
- [Laurin *et al.* 1999] Denis G Laurin, J Angelo Beraldin, Francois Blais, Marc Rioux and Luc Cournoyer. *Three-dimensional tracking and imaging laser scanner for space operations*. In Laser Radar Technology and Applications IV, volume 3707, pages 278–289. International Society for Optics and Photonics, 1999. (Cited on page 25.)
- [Luo *et al.* 2019] Tong Luo, Rongwei Fan, Zhaodong Chen, Xing Wang and Deying Chen. *Deblurring streak image of streak tube imaging lidar using Wiener deconvolution filter*. Optics Express, vol. 27, no. 26, pages 37541–37551, 2019. (Cited on page 36.)
- [Lutzmann *et al.* 2011] P Lutzmann, B Göhler, F Van Putten and CA Hill. *Laser vibration sensing: overview and applications*. In Electro-Optical Remote Sensing, Photonic Technologies, and Applications V, volume 8186, page 818602. International Society for Optics and Photonics, 2011. (Cited on page 1.)
- [Mahmood & Moheimani 2010] Iskandar A Mahmood and SO Reza Moheimani. *Spiral-scan atomic force microscopy: A constant linear velocity approach*. In 10th IEEE International Conference on Nanotechnology, pages 115–120. IEEE, 2010. (Cited on page 72.)
- [McManamon 2015] Paul F McManamon. Field guide to lidar. SPIE Press, 2015. (Cited on page 87.)
- [McManamon 2019a] Paul F McManamon. *Lidar technologies and Systems*, 2019. (Cited on page 3.)
- [McManamon 2019b] PF McManamon. *Design considerations for an auto LiDAR*. In ODS 2019: Industrial Optical Devices and Systems, volume 11125, page 111250G. International Society for Optics and Photonics, 2019. (Cited on page 3.)
- [Melexis 2018] Melexis. *Time-of-flight basis*. 2018. (Cited on pages 6 and 9.)
- [Mitchell *et al.* 2019] John B Mitchell, Gareth Wyn Roberts and Paul CT Rees. *Full-field, high-frequency, heterodyne interferometry for dynamic metrology based on phase detection using a modified time-of-flight camera*. In Optical Measurement Systems for Industrial Inspection XI, volume 11056, page 110560U. International Society for Optics and Photonics, 2019. (Cited on page 11.)

- [NelsoN & Crist 2012] Chad NelsoN and Jordan Crist. *Predicting laser beam characteristics: Mode quality (M2) measurement improves laser performance*. Laser Technik Journal, vol. 9, no. 1, pages 36–39, 2012. (Cited on page 36.)
- [Nguyen *et al.* 2017a] Phuc Nguyen, Hoang Truong, Mahesh Ravindranathan, Anh Nguyen, Richard Han and Tam Vu. *Matthan: Drone presence detection by identifying physical signatures in the drone’s rf communication*. In Proceedings of the 15th Annual International Conference on Mobile Systems, Applications, and Services, pages 211–224. ACM, 2017. (Cited on page 16.)
- [Nguyen *et al.* 2017b] Xuan Truong Nguyen, Hyuk-Jae Lee, Hyun Kimet *al.* *A high-definition LIDAR system based on two-mirror deflection scanners*. IEEE Sensors Journal, vol. 18, no. 2, pages 559–568, 2017. (Cited on pages 12 and 67.)
- [Pacala & Frichtl 2019] Angus Pacala and Mark Frichtl. *Light ranging device having an electronically scanned emitter array*, February 28 2019. US Patent App. 16/028,178. (Cited on page 12.)
- [Paschotta 2006] Rüdiger Paschotta. *Beam parameter product*. Encyclopedia of Laser Physics and Technology, 2006. (Cited on page 35.)
- [Paschotta 2011] Rüdiger Paschotta. *Gaussian beams*. Encyclopedia of Laser Physics and Technology, 2011. (Cited on page 36.)
- [Pierrottet *et al.* 2008] Diego Pierrottet, Farzin Amzajerjian, Larry Petway, Bruce Barnes, George Lockard and Manuel Rubio. *Linear FMCW laser radar for precision range and vector velocity measurements*. Mrs Online Proceedings Library Archive, vol. 1076, 2008. (Cited on page 4.)
- [Poulton *et al.* 2017] Christopher V Poulton, Ami Yaacobi, David B Cole, Matthew J Byrd, Manan Raval, Diedrik Vermeulen and Michael R Watts. *Coherent solid-state LIDAR with silicon photonic optical phased arrays*. Optics letters, vol. 42, no. 20, pages 4091–4094, 2017. (Cited on page 13.)
- [Qu *et al.* 2018] Yang Qu, Yijun Jiang, Yijun He, Zhongfeng Qiu, Shengqiang Wang and Deyong Sun. *A method of reducing stray light of 1.5 μm laser 3D vision system*. Infrared Physics & Technology, vol. 92, pages 266–269, 2018. (Cited on page 26.)
- [Quentel *et al.* 2019] Alain Quentel, Olivier Maurice and Xavier Savatier. *Analytic model for optimizing a long-range, pulsed LiDAR scanner for small object detection*. Applied optics, vol. 58, no. 20, pages 5496–5505, 2019. (Cited on pages 13, 51 and 77.)
- [Quentel *et al.* 2020] Alain Quentel, Olivier Maurice and Xavier Savatier. *Res-Systemica*. 2020. (Cited on page 77.)
- [Richmond & Cain 2010a] R.D. Richmond and S.C. Cain. Direct-detection ladar systems. 01 2010. (Cited on page 3.)
- [Richmond & Cain 2010b] Richard D Richmond and Stephen C Cain. Direct-detection ladar systems, volume 1. SPIE Press Bellingham, 2010. (Cited on page 43.)

- [Royo & Ballesta-Garcia 2019] Santiago Royo and Maria Ballesta-Garcia. *An Overview of Lidar Imaging Systems for Autonomous Vehicles*. Applied Sciences, vol. 9, no. 19, page 4093, 2019. (Cited on pages 3 and 7.)
- [ROYO *et al.* 2018] Santiago ROYO, Jordi RIU, Noel RODRIGO, Ferran SANABRIA and Jan-Erik KÄLLHAMMER. *A vision system and method for a vehicle*, 2018. WO2019012087A1. (Cited on page 25.)
- [Rutz *et al.* 2018] F Rutz, R Aidam, A Bächle, H Heußen, W Bronner, R Rehm, M Benecke, A Sieck, S Brunner, B Göhler *et al.* *InGaAs-based SWIR photodetectors for night vision and gated viewing*. In Electro-Optical and Infrared Systems: Technology and Applications XV, volume 10795, page 1079503. International Society for Optics and Photonics, 2018. (Cited on page 11.)
- [Sato *et al.* 2010] Seiichi Sato, Masafumi Hashimoto, Manabu Takita, Kiyokazu Takagi and Takashi Ogawa. *Multilayer lidar-based pedestrian tracking in urban environments*. In 2010 IEEE Intelligent Vehicles Symposium, pages 849–854. IEEE, 2010. (Cited on page 12.)
- [Shan & Toth 2018] Jie Shan and Charles K Toth. *Topographic laser ranging and scanning: principles and processing*. CRC press, 2018. (Cited on page 1.)
- [Shi *et al.* 2018] Xiufang Shi, Chaoqun Yang, Weige Xie, Chao Liang, Zhiguo Shi and Jiming Chen. *Anti-drone system with multiple surveillance technologies: Architecture, implementation, and challenges*. IEEE Communications Magazine, vol. 56, no. 4, pages 68–74, 2018. (Cited on pages 1, 15 and 19.)
- [Shin *et al.* 2015] Hocheol Shin, Kibum Choi, Youngseok Park, Jaeyeong Choi and Yongdae Kim. *Security analysis of FHSS-type drone controller*. In International Workshop on Information Security Applications, pages 240–253. Springer, 2015. (Cited on page 16.)
- [Steinvall & Chevalier 2005] Ove Steinvall and Tomas Chevalier. *Range accuracy and resolution for laser radars*. In Electro-Optical Remote Sensing, volume 5988, page 598808. International Society for Optics and Photonics, 2005. (Cited on page 37.)
- [Sturdivant & Chong 2017] Rick L Sturdivant and Edwin KP Chong. *Systems engineering baseline concept of a multispectral drone detection solution for airports*. IEEE Access, vol. 5, pages 7123–7138, 2017. (Cited on page 1.)
- [Taha & Shoufan 2019] Bilal Taha and Abdulhadi Shoufan. *Machine learning-based drone detection and classification: State-of-the-art in research*. IEEE Access, vol. 7, pages 138669–138682, 2019. (Cited on page 19.)
- [Vaughan *et al.* 1996] John M Vaughan, Kurt Ove Steinvall, Christian Werner and Pierre Henri Flamant. *Coherent laser radar in Europe*. Proceedings of the IEEE, vol. 84, no. 2, pages 205–226, 1996. (Cited on page 1.)
- [Wang *et al.* 2016] Chunhui Wang, Xiaobao Lee, Tianxiang Cui, Yang Qu, Yunxi Li, Hailong Li and Qi Wang. *Reducing the influence of direct reflection on return signal detection in a 3D imaging lidar system by rotating the polarizing beam splitter*. Applied Optics, vol. 55, no. 7, pages 1559–1564, 2016. (Cited on page 26.)

- [Wang *et al.* 2020] Dingkang Wang, Connor Watkins and Huikai Xie. *MEMS Mirrors for LiDAR: A review*. Micromachines, vol. 11, no. 5, page 456, 2020. (Cited on page 13.)
- [Williams 2017] George M Williams. *Optimization of eyesafe avalanche photodiode lidar for automobile safety and autonomous navigation systems*. Optical Engineering, vol. 56, no. 3, page 031224, 2017. (Cited on pages 9 and 54.)
- [Williams 2018] George M. Williams. *Range-Walk Correction Using Time Over Threshold*. Voxel technical notes, 2018. (Cited on page 37.)
- [Woods *et al.* 2019] William F Woods, Dennis V Delic, Barnaby W Smith, Leszek Świerkowski, Geoffrey S Day, Vladimyro Devrelis and Robert A Joyce. *Object detection and recognition using laser radar incorporating novel SPAD technology*. In Laser Radar Technology and Applications XXIV, volume 11005, page 1100504. International Society for Optics and Photonics, 2019. (Cited on pages 1, 18 and 24.)
- [Wu *et al.* 2011] Long Wu, Yuan Zhao, Yong Zhang, Chenfei Jin and Jie Wu. *Multipulse gate-delayed range gating imaging lidar*. Optics letters, vol. 36, no. 8, pages 1365–1367, 2011. (Cited on page 11.)
- [Yang *et al.* 2019] Yunxiu Yang, Changdong Guo, Shijie Deng, Qian Dai, Haihua Huang, Xian-guo Kou, Xiaolong Lu, Fei Yuan, Li Jing, Jianbo Gao *et al.* *Near-Infrared Array Receiver for Real-Time 3D Imaging Application*. In 2019 IEEE 4th Optoelectronics Global Conference (OGC), pages 89–93. IEEE, 2019. (Cited on page 11.)
- [Yoo *et al.* 2018] Han Woong Yoo, Norbert Druml, David Brunner, Christian Schwarzl, Thomas Thurner, Marcus Hennecke and Georg Schitter. *MEMS-based lidar for autonomous driving*. e & i Elektrotechnik und Informationstechnik, vol. 135, no. 6, pages 408–415, 2018. (Cited on page 12.)
- [Zhang *et al.* 2016] Zhouyu Zhang, Yunfeng Cao, Meng Ding, Likui Zhuang and Weiwen Yao. *An intruder detection algorithm for vision based sense and avoid system*. In 2016 International Conference on Unmanned Aircraft Systems (ICUAS), pages 550–556. IEEE, 2016. (Cited on page 17.)
- [Zhu 2017] Xiang Zhu. *High speed 360 degree scanning LIDAR head*, October 17 2017. US Patent 9,791,555. (Cited on page 12.)